View metadata, citation and similar papers at core.ac.uk
brought to you by CORE
provided by DSpace@MIT

Force and Strain Feedback for Distributed Actuation

by

Alexei A. Makarenko

B.S., Mechanical Engineering
Rensselaer Polytechnic Institute, 1995

SUBMITTED TO THE DEPARTMENT OF AERONAUTICS AND ASTRONAUTICS
IN PARTIAL FULFILLMENT OF THE DEGREE OF

MASTER OF SCIENCE

at the

MASSACHUSETTS INSTITUTE OF TECHNOLOGY

July 1998

© 1998 Massachusetts Institute of Technology
All rights reserved

Signature of Author . . . . . .
Department of Aeronautics and Astronautics
July 23, 1998

Certified by. . . . . .
Professor Edward Crawley
Department of Aeronautics and Astronautics
MacVicar Faculty Fellow
Thesis Supervisor

Accepted by . . . . . .
Associate Professor Jaime Peraire
Chairman, Department Graduate Committee

Force and Strain Feedback for Distributed Actuation

by

Alexei A. Makarenko

Submitted to the Department of Aeronautics and Astronautics
on July 23, 1998 in Partial Fulfillment of the
Requirements for the Degree of Master of Science
at the Massachusetts Institute of Technology

ABSTRACT

A method of shaping the open loop structural transfer function from a distributed sensor to a distributed actuator is developed. The outputs of two sensors of different impedances are combined electronically with the goal of increasing pole-zero spacing for improved performance in low-authority structural control loops. The concept of a three-element actuator-sensor module capable of adjusting the equivalent actuator and sensor impedances is presented. The module consists of an actuator, and two sensors for measuring force and strain. The output of the module is constructed by mixing the force and strain signals using a mixing coefficient which can be used to tune the apparent sensor impedance for maximum performance. General shape of zero trajectories as a function of the mixing coefficient is derived. Mass-spring and beam models are used to further explore the behavior of the zeroes of the mixed transfer function. Both an approximate beam model derived using assumed mode method and the exact solution of the beam vibration equation are employed. A practical implementation of the module is proposed. The design uses a piezoelectric actuator with a collocated piezoelectric strain sensor and a novel piezoelectric shear load cell. A test article was built, mounted on a cantilever aluminum beam, and tested. Experiments verified the ability to increase pole-zero separation of a structural transfer function by mixing the outputs of displacement and force sensors. At low frequencies the overall shape of experimentally found zero trajectories compared well to the results of beam models. Non-minimum phase zeroes encountered for certain values of the mixing coefficient in both the models and the experiments limit the range in which the mixed transfer function is attractive for feedback control.

Thesis Supervisor:
Prof. Edward Crawley
Dept. of Aeronautics and Astronautics

ABSTRACT (RUSSIAN)

AUTHOR / АВТОР
Макаренко Алексей Александрович

THESIS SUPERVISOR / РУКОВОДИТЕЛЬ
Проф. Эдвард Кроули

TITLE / ТЕМА
Датчики силы и деформации для регулятора обратной связи с распределенным приводом

ABSTRACT / ОПИСАНИЕ
Разработан метод изменения формы конструкционной передаточной функции от распределенного датчика к распределенному приводу. Сигналы, поступающие от двух датчиков с различными импедансами, смешаны электронным путем с целью увеличения расстояния между нулями и полюсами передаточной функции, что приводит к улучшению эффективности работы систем активного демпфирования конструкций. Предложена схема трех-элементного "привод-датчик" модуля, способного изменять эквивалентные импедансы привода и датчика. Модуль состоит из привода и двух чувствительных элементов, измеряющих силу и деформацию. Выходной сигнал из модуля составлен путем комбинации сигналов датчиков усилия и деформации при помощи коэффициента, который может быть использован для настройки эквивалентного импеданса датчика на максимальную эффективность работы. Получена общая форма траекторий нулей передаточной функции в зависимости от смешивающего коэффициента. Модели систем из масс, пружин и балок использованы для исследования поведения нулей смешаной передаточной функции. Применены как приблизительные модели балок, полученные методом Рэлея-Ритца, так и точные модели, полученные путем решения уравнения поперечных колебаний. Предложен метод практического воплощения модуля, использующий пьезоэлектрический привод с со-расположенным (collocated) пьезоэлектрическим датчиком деформации, а также оригинальный пьезоэлектрический сдвиговой датчик усилия. Опытный образец был построен, установлен на консольную алюминиевую балку и испытан. Эксперименты подтвердили возможность увеличения разделения нулей и полюсов конструкционной передаточной функции путем смешивания выходных сигналов датчиков деформации и силы. На низких частотах общая форма экспериментально полученных траекторий нулей аналогична результатам математических моделей. Нули с неминимальной фазой, обнаруженные при некоторых величинах смешивающего коэффициента как в моделях так и в экспериментах, ограничивают область, в которой смешанная передаточная функция привлекательна для регуляции с обратной связью.

ACKNOWLEDGMENTS

This research was supported through a grant from NASA Headquarters, Washington, DC, under contract NAGW-2014.

I would like to thank
my advisor Edward Crawley for his guidance in research, skiing, and flying,
my friends for much needed *Melatonin*,
my wife Anne Marie and my parents for their love and support.

Special thanks to Sharon Leah Brown for candy and to Timothy S. Glenn for the Template.

TABLE OF CONTENTS

LIST OF FIGURES

LIST OF TABLES

NOMENCLATURE

a	beam inertial/stiffness parameter [1/s]
c	beam inertial/damping parameter [1/s]
C_m	mixed output gain
D_m	mixed output feedthrough coefficient
E	modulus of elasticity [Pa]
f	distributed forcing function [N/m]
F	force [N]
g	feedback gain for a SISO system
h	actuator moment arm [m]
I	cross sectional moment of inertia of a beam [m^4]
k	wave number [1/m]
k_0	ASM equivalent stiffness [N/m]
k_-	stiffness [N/m]
K	stiffness matrix
L	length [m]
m	linear density of a beam [kg/m]
M	mass matrix
M_-	moment [Nm]
q	vector of generalized coordinates in the assumed mode method
q_1, q_2, q_i	nodal displacements in ASM static model
q_a	actuator deformation [m]
Q	generalized force vector
S	matrix of output influence coefficients in the assumed mode method
t	time [s]
T	kinetic energy
U	potential energy
V	actuation voltage [V]
w	transverse deformation of a beam [m]
y_-	output
x	coordinate in the axial direction of a beam [m]
α	normalized strain sensor stiffness
β	normalized force sensor stiffness
γ	output mixing coefficient

$\bar{\gamma}$	output mixing coefficient for the case of strain and force signals matched using known values of ASM stiffness parameters
$\gamma_0, \gamma_\infty, \gamma_C, \gamma_S, \gamma_F$	special values of the output mixing coefficient
ε	total strain
ζ_i	modal damping
η	normalized actuator moment arm
η_i	normal coordinate
κ	normalized equivalent stiffness of the ASM
λ	actuation strain
Λ	eigen-value matrix
ξ	normalized coordinate in axial direction of the beam
σ	stress [Pa]
Φ	eigen-vector matrix
χ_c	ratio of strain and force sensor output coefficients
χ_k	nondimensional parameter characterizing relative stiffness of the ASM and the structure
χ_y	output matching coefficient
ψ_i	trial function in the assumed mode method
ω_i	modal frequency
$(\text{-})_a$	actuator
$(\text{-})_{asm}$	actuator-sensor module
$(\text{-})_{BC}$	boundary conditions
$(\text{-})_{CL}$	closed-loop
$(\text{-})_{DC}$	zero frequency component
$(\text{-})_e$	exact
$(\text{-})_{ext}$	external
$(\text{-})_f$	force sensor
$(\text{-})^F$	force actuation configuration
$(\text{-})_m$	mixed
$(\text{-})^M$	moment actuation configuration
$(\text{-})_s$	strain sensor
$(\text{-})_{SC}$	static correction

Chapter 1

INTRODUCTION

Motivation

Active structural control is often necessary to achieve performance specifications demanded in the aerospace and, increasingly, other fields. The difficulties encountered in modeling complex structures manifest themselves in decreasing modeling accuracy at higher frequencies. Controlled Structures Technologies framework shown in Figure 1.1 is a road map of design choices, both passive and active, available to engineers for reaching performance and robustness specifications. The work done in this thesis is applied to local control which is one of the active measures shown in the diagram.

Local or low authority control (LAC) implies that the control law is based only on information from the vicinity of the actuator. Collocated actuators and sensors are typically used for local control because if the actuator and sensor are collocated and dual (their product is power) then the input-output transfer function is positive real, with an alternating pole-zero structure and phase bounded by $\pm 90^\circ$ [Burke, 1991; Fleming, 1991]. If, in addition, the compensator applied to the structure is strictly positive real then the closed-loop system is guaranteed to be stable and the compensator will add damping to the structure.

Stability guarantees of LAC make it a perfect compliment for global or high authority control (HAC). By providing broadband increase in damping, local controller or controllers

robustify flexible modes in the roll-off region and improve performance at higher frequencies where HAC is not designed to work [Auburn, 1980; Hall, 1991].

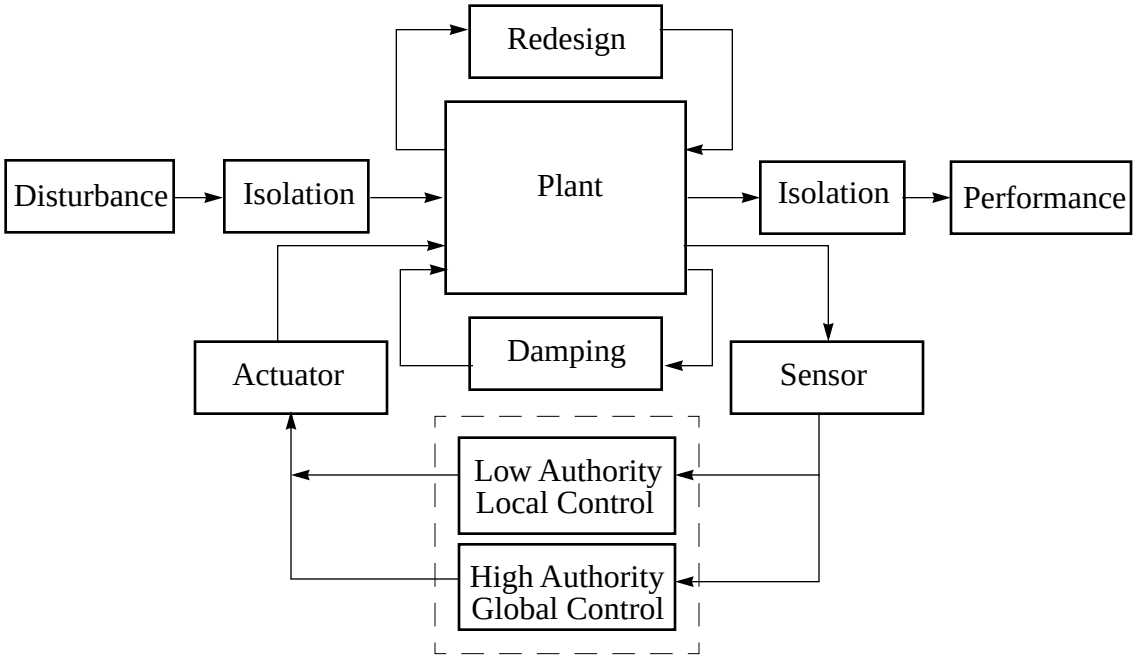

Figure 1.1 Controlled Structures Technologies (CST) framework.

Good pole-zero spacing in the open-loop transfer function is beneficial for actively adding damping to the structure [Fanson, 1989; Spangler, 1994]. This property is best visualized by considering the root locus of a lightly damped structural system with collocated actuator and sensor: for larger pole-zero separation in the plant transfer function the root locus will travel farther into the left-half plane of the s-plane. The goal of the designer then is to find the actuator-sensor pair which leads to a transfer function with good pole-zero separation, which is analogous with good observability and controllability of the modes.

This work focuses on shaping the open loop transfer function from distributed sensors to distributed actuators with the goal of exercising influence over pole-zero spacing. The pole-zero structure depends on the choice of the actuator, sensor, and their locations. Throughout this work the actuator location and its impedance relative to the structure are assumed to be chosen to maximize actuation efficiency [Anderson, 1993]. For a collocated

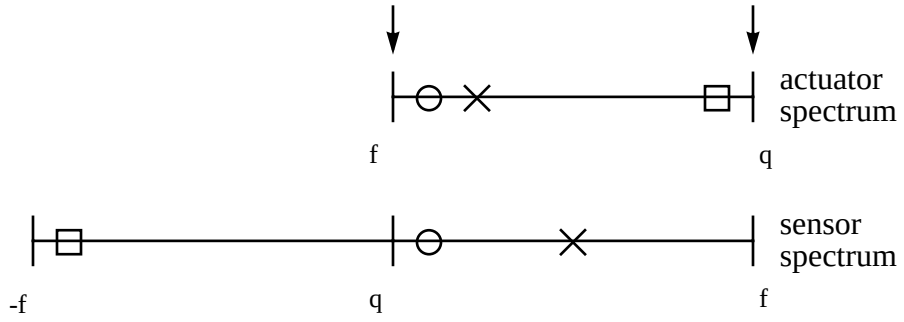

Figure 1.2 Actuator and sensor spectra [Fleming, 1990]. Sensor impedance is defined as the output signal content relative to two extremes: a generalized force and a generalized displacement sensors; also shown are special actuator-sensor pairs: complementary extremes (arrows), positive compliments (circles), negative compliments (squares), positive non-compliments (crosses)

actuator-sensor pair, the sensor is placed at the same position as the actuator. The remaining parameter is sensor "impedance" defined as the position of the sensor's output along the so-called sensor impedance spectrum shown in Figure 1.2 [Fleming, 1990]. A low impedance sensor measures deformation q whereas a high impedance sensor measures force f. The goal is to find a sensor whose impedance can be set in the design stage and later easily tuned during operation.

One way of building a sensor whose impedance can be set arbitrarily by mixing the outputs of two distinct transducers whose individual impedances are near the extremes of the sensor impedance spectrum.

Objectives

This work pursues three objectives:

- To identify characteristic features of zero trajectories resulting from output mixing by considering models of simple structures
- To build a piezoelectric shear load cell suitable for distributed actuation of beams and incorporate it into an actuator-sensor module (ASM)
- To experimentally demonstrate the feasibility of controlling pole-zero separation in a piezoelectric-to-piezoelectric transfer function by means of adjusting the effective sensor impedance of the actuation-sensor module using output mixing

Background

Piezoelectric materials have been used extensively in structural vibration control. Numerous examples exist of their use as both actuators and sensors. The two form factors in wide use are stacks and thin wafers. Stacks are more commonly used as actuators in so-called active struts incorporated into trusses [Fanson, 1989; Lurie, 1992]. Thin wafers on beams have been used as actuators [Burke, 1987; Crawley, 1987; Crawley, 1990; References], as collocated actuators and sensors [Andersson, 1993; McCain, 1995; Yung, 1996], and as nearly collocated actuators and sensors [Fanson, 1990]. In the applications above where a piezoelectric sensor was used, the sensor was placed in parallel with the actuator and measured mostly strain with a certain amount of force information mixed in due to feedthrough. A notable exception is simultaneous sensing and actuation discussed separately below.

As was already mentioned, well spaced poles and zeroes in the open-loop transfer function are necessary for effective active damping. For collocated actuators and sensors piezoelectric-to-piezoelectric transfer functions are known to have close pole-zero spacing thus limiting the achievable performance [Fanson, 1990; McCain, 1995; Yung, 1996]. Several studies aiming at maximizing the active damping performance have been conducted.

A theoretical study of the effects of varying the relative actuator and sensor impedances on the pole-zero structure was conducted by Fleming [Fleming, 1990; Fleming, 1991]. The sensor output was defined as a mixture of fictitious displacement and force sensors in a mass-spring system. Both actuator and sensor impedances were varied through their entire ranges presented as the actuator and sensor spectra which are reproduced in Figure 1.2. The analysis of the pole-zero structure of the output transfer function was performed at discrete points termed complementary extremes, positive compliments, negative compliments, and positive non-compliments. The positions of these configuration on the spectra are marked in Figure 1.2. It was shown that pole-zero spacing changes as the output mixture is adjusted. Pole-zero cancellation was predicted for certain positive mixtures and

non-minimum phase (NMP) real-valued zeroes were encountered for negative mixtures. It was concluded that the appearance of NMP zeroes was not an artifact of modal truncation.

In practice, the impedances of the actuator and the structure are often matched in order to maximize actuation efficiency meaning that the actuator impedance falls somewhere in the middle of the actuator spectrum. Because pole-zero separation is maximized by choice of a sensor of complementary impedance, it is desirable to have a sensor which produces mixed force-strain signal. Output mixing can accomplish this but the question remains on how to physically obtain the mixed output.

In one possible approach, simultaneous sensing-actuation accomplishes the task by using just one sensor [Hagood, 1991; Spangler, 1994]. An electrical circuit incorporating the piezoelectric element is used to measure both voltage and current at the piezoelectric terminals. It was shown that by tuning the electrical circuit, a signal proportional to strain, force, and any combination of the two can be obtained.

Another approach is to use outputs of two distinct sensors measuring displacement and force directly. In the past this approach has been used to improve performance in broadband damping augmentation of a space truss [Chen, 1990; Lurie, 1992]. Mechanical-electrical analogy was used to cast the problem as bridge feedback which in communication engineering refers to feeding back both current and voltage. The experiment used an active truss member with a built-in eddy current displacement sensor and an externally attached load cell to obtain independent measurements of displacement and force. Closed loop experiments were performed to verify the effectiveness of the method.

This thesis focuses on applying the idea of mixed feedback to distributed sensing and actuation of beams. The design uses a piezoelectric actuator with a collocated piezoelectric strain sensor and a novel piezoelectric shear load cell. The possibility of changing the pole-zero spacing in beam transfer functions is explored on models and in experiments.

Approach

In Chapter 2 the mixed output approach is explored on models of simple structures. Shortcomings of single-sensor setups in adjusting the sensor “impedance” are demonstrated first. A concept of a three-element actuator-sensor module (ASM) is presented which incorporates an actuator and two sensors of different sensor impedance. A simple static model of the ASM is constructed and its features independent of the underlying structure are investigated. The shape of the zero trajectory is drawn as a function of the output mixing coefficient and the internal relative stiffnesses. The expected zero trajectory shows strong dependence on the mixing coefficient. It also predicts real-valued non-minimum phase (NMP) zeroes for a range of negative values of the mixing coefficient.

The ASM is then integrated into models of a lumped parameter and continuous systems to verify the general properties of the ASM and to develop additional insights into the effects of sensor “impedance” on the pole-zero structure of the open loop transfer function. Both exact and approximate models of beams are employed. The partial differential equation of beam in vibration is solved directly to obtain the exact input-output transfer functions, poles, and zeroes. Assumed mode method is used to find an approximate finite-dimensional representation of the beam structure.

Chapter 3 covers practical implementation of an ASM capable of distributed actuation and sensing on a beam. As a stepping stone to building the ASM, feasibility of building a piezoelectric shear load cell is demonstrated. The test article consisting of the ASM and a cantilever aluminum beam is described. Design and manufacturing issues encountered in building the test article are reported.

Chapter 4 presents experimental results. Two individual sensor transfer functions and hardware-mixed transfer functions were measured. In the low frequencies the appearance of the experimental zero trajectory plot is found similar to the shape derived from the static ASM model. Some features of zero transfer functions not encountered in models are highlighted, e.g. NMP complex zeroes.

Conclusions and recommendations for future work are found in Chapter 5.

The scope of this work does not include the implications of the presence of real-valued zeroes in the plant transfer function for local control. Also left unaddressed is an important issue of actuator efficiency raised by the specific actuator-sensor module design described in Chapter 3 and tested in Chapter 4.

Chapter 2

MODELING SYSTEMS WITH FORCE AND STRAIN SENSORS

In this chapter the concept of using mixed force and strain feedback for affecting the relative pole and zero spacing is explored on simple analytical models of lumped-parameter and distributed systems. The objective of this chapter is to demonstrate that, at least in theory, mixing the outputs of the force and strain sensors is an efficient way of changing the position of the transfer function zeroes.

The first section motivates the use of output mixing and introduces a three-element active device which acts as a collocated actuator-sensor pair and achieves an arbitrary sensor impedance value by mixing the outputs of two sensors of different impedance. This device is termed actuator-sensor module (ASM). A simple static model of the ASM is derived and an analytical input-output relationship is obtained. Based on the static model, properties of the zeroes of the mixed transfer function independent of the underlying structure are derived.

The following three sections integrate the actuator-sensor module into representative structural systems. A simple mass and spring system is modeled first. Next a cantilever beam is modeled using an approximate and an exact solution methods. Two actuator configurations in which the ASM applies force and moment are considered for each solution method.

Finally, the results obtained using different modeling technics are compared and conclusions are presented. Special attention is given to the presence of non-minimum phase (NMP) zeroes in the mixed transfer function for a range of negative values of the mixing coefficient. The preliminary conclusion states that the NMP zeroes are indicative of true NMP response of the system and are not a result of modal truncation.

2.1 Actuator-Sensor Module

In this section the concept of output mixing is motivated by limitations of typical strain and force sensors. These limitations can be overcome and greater control of zero locations can be achieved by using two sensors of different “impedance” whose output can be combined into a signal which can be considered the output of a virtual sensor. A general form of a three-element actuator-sensor module (ASM) designed for output mixing is proposed. A static lumped-parameter model of an ASM is constructed and its input-output relationship is derived. The model does not incorporate any information on a specific implementation of the ASM components. Important properties of output mixing are derived which do not depend on the details of the structure to which the ASM is attached. The method of integrating an ASM into the structure used later in the chapter is outlined.

2.1.1 Concept

It is generally excepted that the zeroes of a transfer function are influenced greatly by the relative impedance of the actuator to the structure and the relative impedance of the sensor to the structure. The relative mechanical impedance of an actuator can be easily modified by simply adjusting its stiffness or by changing its position on the structure so that the driving point impedance of the structure is changed. For example, an actuator which is much stiffer than the structure commands nearly pure displacement. On the other hand, a very soft actuator placed at the same location on the same structure commands nearly pure force.

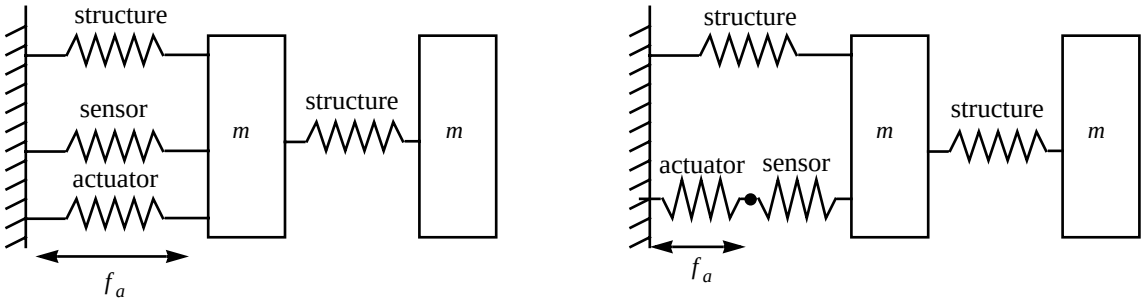

Figure 2.1 Typical sensor applications: (a) strain sensor placed in parallel with a structural stiffness and, in this case, an actuator; and (b) force sensor placed in series with an actuator.

The situation is different with sensors. Two common sensor configurations are shown in Figure 2.1 and discussed in turn below. A transducer placed in *parallel* with an actuator and a structural stiffness (see Figure 2.1a) produces an output proportional to the deformation in the structure regardless of its own stiffness. Therefore its sensor "impedance" as illustrated in Figure 1.2 can not be modified by changing its mechanical impedance. A similar argument can be made about a transducer placed in *series* with an actuator (see Figure 2.1b) and whose output is proportional to the deformation across its length. The measured output is exactly the force acting through the actuator on the structure regardless of the mechanical of the sensor stiffness.

The conclusion from these arguments is that, at least in the simple cases described above, the sensor "impedance" of a transducer is dictated by its placement on the structure relative to the actuator and cannot be modified by adjusting its mechanical impedance (stiffness).

As was pointed out in Chapter 1, it is often desirable to be able to measure a mixture of force and displacement in order to maximize power dissipation in the control loop. The two classical sensor configurations in Figure 2.1 lead to strain and force measurements. If both sensors are installed then their outputs can be combined to obtained the desired mixture of strain and force information.

ASM Concept

The conceptual diagram of a three-element actuator-sensor module is shown in Figure 2.2. At least three active element are necessary to implement such a device: an actuator, a low "impedance" sensor in parallel with the actuator, and a high "impedance" sensor in series with the first two. The actuator is driven by a control signal and the output of the module is a linear combination of the signals from the two sensors.

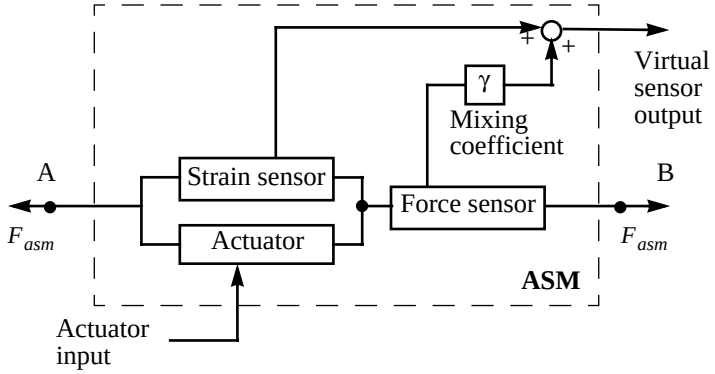

Figure 2.2 A conceptual representation of a three-element actuator-sensor module (ASM) does not imply any modeling technique or practical implementation.

The output of the module can be regarded as the output of a virtual sensor whose content is adjusted with a mixing coefficient γ. When attached to a structure, an ASM produces the actuation force F_{asm}. For better visualization, Figure 2.2 shows an ASM with two discrete attachment points marked A and B. However, as will be seen in Chapter 3, distributed actuation and sensing is certainly possible.

In the context of local control both sensors are assumed to be collocated with the actuator. The only other requirement is that the two sensors have impedances such that they are linearly independent.

Note that the two active elements intended to be used as sensors are labeled *strain* and *force sensors* based on common practice and the lack of a better term. The analysis in this section will show that the signals produced by the two sensors are not necessarily pure

strain and force. Extra care will be taken to distinguish the outputs of the strain and force sensors from pure strain and force measurements.

A high-fidelity model of the device in Figure 2.2 is dependent on the particular implementation of the device's components. Some important properties of output mixing can be derived from the most basic model of the ASM.

2.1.2 Static Model

The simplest way to represent the actuator and sensors in Figure 2.2 is to model them as springs with stiffnesses k_a for the actuator, k_s for the strain sensor, and k_f for the force sensor (see Figure 2.3). This modeling approach leads to a static lumped-parameter model of the actuator-sensor module.

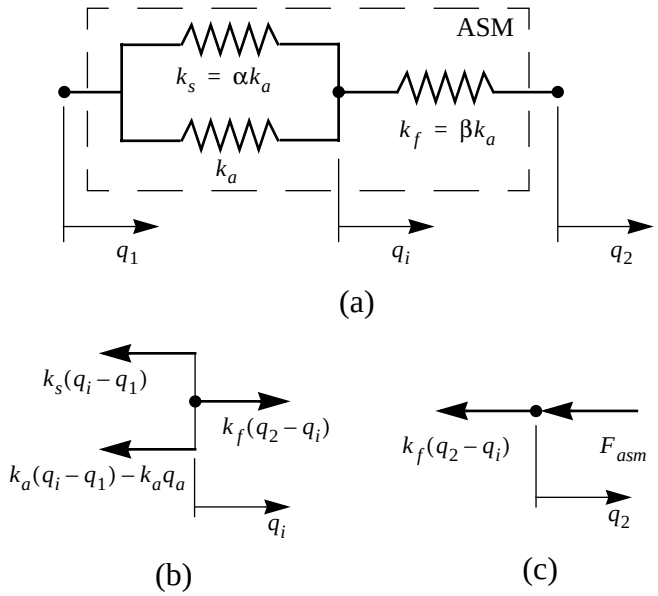

Figure 2.3 Static lumped-parameter model of an actuator-sensor module (ASM): (a) diagram; (b) force balance at spring juncture; (c) force balance at the juncture between the load cell and the structure.

In the spring model of the ASM the inertias of all active elements are ignored. This is equivalent to making the assumption that the internal dynamics of the actuator and sensors

lie outside the bandwidth of interest and the device is operated quasi-statically. Internal frequencies of a practical ASM design are discussed in Chapter 3.

To facilitate a parameter study, both sensor stiffnesses are normalized by the actuator stiffness k_a leading to the normalized strain sensor stiffness,

$$\alpha = \frac{k_s}{k_a} \tag{2.1}$$

and the normalized force sensor stiffness,

$$\beta = \frac{k_f}{k_a} \tag{2.2}$$

The equivalent stiffness of the entire module can be calculated as follows,

$$k_0 = \frac{k_f(k_a + k_s)}{k_a + k_s + k_f} \tag{2.3}$$

After rewriting the expression above in terms of the normalized sensor stiffnesses and normalizing the result by the actuator stiffness k_a, the equivalent normalized ASM stiffness is found.

$$\kappa \equiv \frac{k_0}{k_a} = \frac{(1+\alpha)\beta}{1+\alpha+\beta} \tag{2.4}$$

Note that for a stiff load cell, i.e. $\beta \gg (1+\alpha)$, the normalized equivalent ASM stiffness κ is equal to $(1+\alpha)$. If, in addition, a soft strain sensor is used, i.e. $\alpha \ll 1$, the normalized equivalent stiffness approaches unity, which means that the stiffness of the entire module is dominated by the actuator stiffness.

Actuation

In the derivation of the actuation equation, certain simplifying assumptions about the geometry and material properties are made. All three active elements are assumed to be of

prismatic shape and their mechanical and electrical properties are assumed to be uniform throughout the material. With these assumptions, the axial stiffness of the actuator can be found as

$$k_a = \frac{E_a A_a}{L_a} \tag{2.5}$$

where E_a is the modulus of elasticity of the active material, while A_a and L_a are the cross-sectional area and the length of the active element respectively.

Actuation and sensing can be based on any one of the known mechanisms that convert electrical energy into mechanical and back. The piezoelectric effect is a notable example in this category.

The *total* strain in the actuator ε_a consists of the *mechanical* strain equal σ_a / E_a and the *actuation* strain λ. For a piezoelectric actuator the actuation strain is a function of the voltage applied at the actuator electrodes.

$$\varepsilon_a = \frac{\sigma_a}{E_a} + \lambda \tag{2.6}$$

Substituting $\varepsilon_a = (q_i - q_1)/L_a$, the internal force $F_a = \sigma_a A_a$ created by the actuator can be found as

$$F_a = k_a(q_i - q_1) - k_a q_a \tag{2.7}$$

where k_a is the stiffness of a prismatic actuator and $q_a = L_a\lambda$ is the actuator deformation. Note that for an actuator fixed between two rigid constraints, i.e. $q_i - q_1 = 0$, the actuation force equals the so-called *commanded force* (also known as clamped force) defined as the product of the actuator stiffness and its deformation under free-free conditions. Also note that the opposite signs for the force F_a and the actuator deformation q_a are explained by negative (compressive) stresses generated in the actuator when the actuator is constrained and positive elongation is induced. The force F_a therefore must be inter-

preted as the reaction force applied to the actuator. After performing force balance at the internal spring junction (see Figure 2.3b), the spring junction displacement q_i is found.

$$q_i = \frac{1}{1+\alpha+\beta}[(1+\alpha)q_1 + \beta q_2 + q_a] \tag{2.8}$$

Because of the static nature of the problem, the same result for the displacement of the spring junction can be obtained by using the mechanical equivalent of the voltage divider rule according to which $q_i - q_1 = q_a + \frac{k_0}{k_s + k_a}(q_2 - q_1)$, which leads to (2.8). This exercise is useful to clarify that the relative stiffness ratios found in (2.8) and later in the chapter are nothing but indicators of stiffness distribution in the components of the ASM.

Another force balance is performed at the ASM/structure junction (see Figure 2.3c) to find the force applied by the ASM onto the structure as,

$$F_{asm} = \frac{\beta k_a}{1+\alpha+\beta}[-(1+\alpha)q_{asm} + q_a] \tag{2.9}$$

where $q_{asm} = q_2 - q_1$ is the deformation across the ASM. The force supplied by the ASM can also be written in terms of the equivalent stiffness k_0.

$$\boxed{F_{asm} = k_0\left(-q_{asm} + \frac{1}{1+\alpha}q_a\right)} \tag{2.10}$$

From the expression in (2.9) in order to have high actuation effectiveness the device has to have a stiff load cell and a soft strain sensor.

Sensor Outputs

The signal produced by the active element connected in *parallel* with the actuator is assumed to be proportional to its own deformation.

$$y_s = c_s(q_i - q_1) \tag{2.11}$$

where the coefficient c_s is determined by the geometry and the material properties of the sensor. Substituting the expression for the displacement of the internal node q_i from (2.8)

$$y_s = \frac{c_s}{1 + \alpha + \beta}(\beta q_{asm} + q_a) \tag{2.12}$$

The output signal in (2.12) is proportional to the deformation across the ASM, but it also contains a feedthrough term from the actuator deformation q_a. To make this point more clear, the strain sensor output y_s is rearranged as a sum of the ASM deformation and force,

$$\frac{y_s}{c_s} = q_{asm} + \frac{1}{\beta k_a} F_{asm} \tag{2.13}$$

When the sensor in series with the actuator is stiffer than the rest of the ASM components, i.e. $\beta \gg (1 + \alpha)$, the feedthrough term in (2.12) becomes relatively small and the output of the sensor in parallel with the actuator is proportional only to the ASM deformation q_{asm}. Because of this limiting property and for lack of a better term, the sensor placed in parallel with the actuator is referred to as the *strain sensor* although it is important to keep in mind that for the case of finite sensor stiffness the output of the strain sensor also contains force information.

Also note, that the amount of pure strain and force information mixed into the strain sensor output depends on the normalized force sensor stiffness. It appears at first that this dependence makes possible to change the strain sensor “impedance” without using output mixing. However, two consideration limit the usefulness of this approach. First, the degree to which the content of the output can be varied is limited by the penalty on the actuator effectiveness imposed by reducing the force sensor stiffness located in the load path between the actuator and the structure. Second, only positive values of the strain and force mixture are realizable because the natural “mixing coefficient” in this case is set by the ratio of stiffnesses which can only be positive.

The output of the sensor in *series* with the actuator is also assumed to be proportional to its own deformation.

$$y_f = c_f(q_i - q_2) \tag{2.14}$$

where the measurement coefficient c_f is determined by the geometry and the material properties of the sensor and is most likely different from the strain sensor coefficient c_s. Substituting the expression for the middle node displacement q_i from (2.8), the force output expression is expanded as,

$$y_f = \frac{c_f}{1 + \alpha + \beta}(-(1 + \alpha)q_{asm} + q_a) \tag{2.15}$$

By comparing the result with equation (2.9), it is apparent that the output of the sensor placed in series with actuator is proportional only to the force exerted by the ASM onto the structure. For this reason, this sensor is called the *force sensor* or the load cell.

$$\boxed{\frac{y_f}{c_f} = \frac{1}{\beta k_a} F_{asm}} \tag{2.16}$$

A special note is warranted on the signs implicit in the sensor output definitions in (2.12) and (2.15). For a stiff load cell, i.e. $\beta \gg (1 + \alpha)$, and a positive strain sensor coefficient c_s, the strain sensor output is positive when the strain sensor is in tension. For a positive force sensor coefficient c_f, the force sensor output is positive when the force sensor is in compression. This corresponds to both sensors producing positive signal when the ASM pushes against two rigid constraints.

Implementing the ideas presented at the beginning of the section, the output of a virtual sensor of arbitrary impedance is constructed by combining the outputs of the force and the strain sensors using a mixing coefficient γ and the output matching coefficient χ_y. The output produced according to (2.17) will be called the *mixed output* referring to the mixture of signals put out by the strain and force sensors.

$$\boxed{y_m = y_s + \gamma\chi_y y_f} \tag{2.17}$$

Both γ and χ_y are scalar design parameters. A separate "pre-mixing" coefficient χ_y is introduced in order to equalize the contributions from the force and strain sensors before combining them with γ. This step is convenient in light of the practical implementation discussed in Chapter 4.

The exact meaning of output equalizing is open for interpretation. Since the outputs of both strain and force sensors are functions of frequency they can be matched either at a specific frequency (including at DC) or in the integral sense over the bandwidth of interest. Both of these approaches can be applied to the model of a specific structure or directly to experimental data.

Substituting the strain and force output expressions (2.12, 2.15) and dividing through by c_s, the mixed output is rewritten as,

$$y_m = \frac{c_s}{1+\alpha+\beta}\left(\beta - \gamma\frac{\chi_y}{\chi_c}(1+\alpha)\right)q_{asm} + \frac{c_s}{1+\alpha+\beta}\left(1+\gamma\frac{\chi_y}{\chi_c}\right)q_a \tag{2.18}$$

where $\chi_c = \frac{c_s}{c_f}$ is the sensor output gain ratio. The expression above can be rearranged to show explicitly how the mixing coefficient adjusts the ratio of strain and force information in the mixed output.

$$\frac{y_m}{c_s} = q_{asm} + \frac{1}{\beta k_a}\left(1+\gamma\frac{\chi_y}{\chi_c}\right)F_{asm} \tag{2.19}$$

The expression for the mixed output can be simplified by adopting a reasonable choice for the output matching coefficient $\bar{\chi}_y$. The sensor signals y_s and y_f were defined to be equal to products of the sensor gains c_s and c_f with the appropriate sensor deformations. Therefore the difference in the two output levels, at least according to this model, is due solely to these two factors. By making the output matching coefficient proportional to the ratio of the sensor gains and inversely proportional to the sensor stiffness ratio, the two sensor signals are equalized. The specific value of the output matching coefficient is designated $\bar{\chi}_y$.

$$\bar{\chi}_y = \frac{\beta}{1+\alpha}\chi_c \tag{2.20}$$

Substituting $\bar{\chi}_y$ into the general expression for the mixed output and setting the strain sensor output gain c_s to unity for simplicity, the mixed output expression specialized for the case of simple output matching is obtained.

$$\boxed{\bar{y}_m = \frac{\beta(1-\gamma)}{1+\alpha+\beta}q_{asm} + \frac{1+\alpha+\beta\gamma}{(1+\alpha)(1+\alpha+\beta)}q_a} \tag{2.21}$$

The form of the measurement equation (2.21) is more revealing and is particularly convenient in the modeling of simple structures later in this chapter, but the output equalization relies on the knowledge of the ASM component stiffnesses which, as will be seen in Chapters 3 and 4, are not always easy to measure or even estimate. Therefore, the more general form of the measurement equation (2.18) will also be found useful.

For brevity, the measurement equation (2.21) will be referred to as,

$$\bar{y}_m = C_m q_{asm} + D_m q_a \tag{2.22}$$

with the gains C_m and D_m defined below.

$$C_m = \frac{\beta(1-\gamma)}{1+\alpha+\beta} \tag{2.23}$$

$$D_m = \frac{1+\alpha+\beta\gamma}{(1+\alpha)(1+\alpha+\beta)} \tag{2.24}$$

The static lumped parameter model of the ASM can also be expressed in the form convenient for the ASM-structure integration performed by means of feedback as described later in this section.

$$\begin{bmatrix} \bar{y}_m \\ F_{asm} \end{bmatrix} = \frac{1}{1+\alpha+\beta}\begin{bmatrix} \frac{1+\alpha+\beta\gamma}{1+\alpha} & \beta(1-\gamma) \\ \beta k_a & -(1+\alpha)\beta k_a \end{bmatrix}\begin{bmatrix} q_a \\ q_{asm} \end{bmatrix} \tag{2.25}$$

Special Values of the Mixing Coefficient

Five special values of the mixing coefficient can be identified by considering the measurement equations (2.18) and (2.21). These special values of γ correspond to the instances of the mixed transfer function which are of interest either by definition or because of the properties of their zeroes. These special mixtures discussed in turn below are (1) measured strain output, (2) measured force output, (3) pure strain output, (4) pure commanded force output, and (5) zero steady state response output.

Measured Strain Output. For $\gamma_0 = 0$ the mixed transfer function includes no contribution from the force sensor and the virtual sensor measures the mixture of strain and force information naturally produced by the strain sensor as given by (2.12). The zeroes of the mixed transfer function are the zeroes of the strain sensor transfer function.

Measured Force Output. For $|\gamma_\infty| \gg 1$ the signal from the force sensor given in (2.15) dominates the mixed output with the sign determined by the sign of the mixing coefficient. The zeroes of the mixed transfer function approach the zeroes of the force sensor transfer function as the magnitude of the mixing coefficient approaches infinity

Pure Strain Output. Pure strain is measured when the mixed transfer function does not contain any feedthrough from the actuator deformation q_a. The corresponding mixing coefficient is found by setting the term in front of the actuator deformation in (2.18) equal to zero.

$$\gamma_S = -\frac{\chi_c}{\chi_y} \tag{2.26}$$

The subscript in γ_S stands for *strain*. Substituting $\bar{\chi}_y$ from (2.20) a more telling value $\bar{\gamma}_S$ is found for the case of explicit strain and force sensor output matching.

$$\bar{\gamma}_S = -\frac{1+\alpha}{\beta} \tag{2.27}$$

In the limit, when the stiffness of the load cell is large compared to the rest of the module, i.e. $\beta \gg 1 + \alpha$, $\bar{\gamma}_S$ approaches zero. This draws attention to the fact that for an ASM with a stiff load cell, the strain sensor measures nearly pure strain, and little contribution from the force sensor is necessary to cancel out the feedthrough term normally present in the strain sensor output. Substituting $\gamma = \gamma_S$ into (2.18), the expression for the mixed output is found.

$$y_m\big|_{\gamma_s} = q_{asm} \tag{2.28}$$

Note that substituting $\bar{\gamma} = \bar{\gamma}_S$ into (2.21) leads to the same result.

Pure Commanded Force Output. Pure feedthrough from the actuator deformation q_a is measured when the structural modes become unobservable through the virtual sensor. To find the corresponding mixing gain γ_C the coefficient in front of ASM deformation term q_{asm} is set equal to zero.

$$\gamma_C = \frac{\beta}{1 + \alpha}\frac{\chi_c}{\chi_y} \tag{2.29}$$

The subscript in γ_C stands for pole-zero *cancellation*. When the force and strain signals are matched using $\bar{\chi}_y$ the pole-zero cancellation occurs when the mixing coefficient equals one.

$$\bar{\gamma}_C = 1 \tag{2.30}$$

The output of the virtual sensor in this case can be interpreted as a specially balanced sum of the force and strain measurements and is found as.

$$y_m\big|_{\gamma_C} = \frac{1}{1 + \alpha} q_a \tag{2.31}$$

Same expression is obtained for $\bar{y}_m$ with $\bar{\gamma} = \bar{\gamma}_C$.

Zero Steady State Response Output. The fifth special mixture is defined as the virtual sensor which produces zero steady-state response to a step input. Equivalently in frequency domain, the transfer function to this output has a zero DC gain. The mixing coefficient γ_F corresponding to this signal is found by applying the finite value theorem to the expression for the mixed output in (2.18) and setting steady-state value to zero. The subscript in γ_F stands for *final* value.

The final value of the mixed output depends on the final value of the transfer function from the commanded actuator deformation q_a to the deformation across the ASM. This means that γ_F unlike the other special values of γ can not be found by considering the ASM by itself, the information about the structure is also necessary.

$$\lim_{s \to 0} s \frac{y_m(s)}{q_a(s)} = \left(\beta - \gamma_F \frac{\chi_y}{\chi_c}(1+\alpha)\right) \lim_{s \to 0} \frac{q_{asm}(s)}{q_a(s)} + \left(1 + \gamma_F \frac{\chi_y}{\chi_c}\right) = 0 \tag{2.32}$$

The DC value of the dynamic transfer function $\frac{q_{asm}(s)}{q_a(s)}$ is simply the static deformation across the ASM due to the actuation load when the ASM is connected to a structure. The stiffness of a generic structure is characterized by k_{str} which is the equivalent static stiffness seen by the actuator-sensor module. The deformation across the ASM is then calculated as $q_{asm}^{DC} = \frac{F_{asm}}{k_{str}}$. Substituting the expression for the force produced by the module from (2.10), the DC value of the transfer function to the ASM deformation is found as,

$$\frac{q_{asm}^{DC}}{q_a} = \frac{\chi_k}{1+\chi_k} \frac{1}{1+\alpha} \tag{2.33}$$

where χ_k is a non-dimensional stiffness parameter defined as the ratio of the ASM equivalent stiffness to the static driving-point stiffness of the structure.

$$\chi_k = \frac{k_o}{k_{str}} \tag{2.34}$$

More specific expressions for χ_k will be found for the structures modeled in the following sections. Substituting (2.33) into (2.32), a more general form of γ_F is obtained.

$$\gamma_F = -\frac{\chi_c}{\chi_y}\left(1 + \chi_k \frac{1+\alpha+\beta}{1+\alpha}\right) \tag{2.35}$$

As before the result is specialized for the case of explicit output matching by substituting $\bar{\chi}_y$ from (2.20).

$$\bar{\gamma}_F = -\frac{1}{\beta}[1 + \alpha + \chi_k(1+\alpha+\beta)] \tag{2.36}$$

Because the sign of γ_F is negative, this mixture may be interpreted as the balanced *difference* of the strain and force measurements. In the limit, when the force sensor is stiff, i.e. $\beta \gg 1$, and the strain sensor is soft, i.e. $\alpha \ll 1$, the mixing gain $\bar{\gamma}_F$ approaches $-\chi_k$. If, in addition, the impedances of the module and the structure are matched, i.e. $\chi_k = 1$, the zero-steady-state mixture is obtained with the mixing coefficient of $\bar{\gamma}_F = -1$. The mixed transfer function for this case is found as follows.

$$y_m\big|_{\gamma_F} = q_{asm} - \frac{\chi_k}{k_0} F_{asm} = (1+\chi_k) q_{asm} + \frac{\chi_k}{1+\alpha} q_a \tag{2.37}$$

All five special values of γ are summarized in the Table 2.1. Two forms of mixing coefficients, with and without output matching, are included. In addition, limiting values for the cases of stiff load cell and soft strain sensors are listed.

Structure / ASM Integration

A common procedure is used in the following sections to integrate an actuator-sensor module (ASM) into a specific structure. An important first step in to select an appropriate actuator stiffness. To achieve good strain energy efficiency, the actuator impedance must be matched to some representative stiffness of the structure [Anderson, 1993]. For simplicity, static impedance matching is performed.

After the actuator stiffness is chosen, the structural model of the system is augmented with the equivalent stiffness of the ASM given in (2.4). The ASM force given in (2.10) is applied at the actuation points. The structural response at the mounting points of the ASM

TABLE 2.1 Special values of the mixing coefficient γ with and without output matching, limiting values for stiff force sensor and soft strain sensor, and the interpretation of the transfer functions corresponding to the mixing coefficients.

Case	Mixing Coefficients					Transfer Function Interpretation
	γ	$\bar{\gamma} = \gamma\|_{\chi_y = \bar{\chi}_y}$	$\lim_{\alpha \to 0} \bar{\gamma}$	$\lim_{\beta \to \infty} \bar{\gamma}$	$\lim_{\substack{\alpha \to 0 \\ \beta \to \infty}} \bar{\gamma}$	
γ_0	0	0	0	0	0	Strain sensor TF, mixture of strain and force.
γ_∞	$\pm\infty$	$\pm\infty$	$\pm\infty$	$\pm\infty$	$\pm\infty$	Force sensor TF, pure force applied by the ASM onto structure.
γ_S	$\frac{\beta}{1+\alpha}\frac{\chi_c}{\chi_y}$	1	1	1	1	Pure feedthrough, all poles and zeroes are cancelled.
γ_C	$-\frac{\chi_c}{\chi_y}$	$-\frac{1+\alpha}{\beta}$	$-\frac{1}{\beta}$	0	0	Pure strain measurement.
γ_F	$-\frac{\chi_c}{\chi_y}\left[1+\chi_k\frac{1+\alpha+\beta}{1+a}\right]$	$-\frac{1+\alpha}{\beta}-\chi_k\frac{1+\alpha+\beta}{\beta}$	$-\chi_k$	$-\frac{1}{\beta}-\chi_k\frac{1+\beta}{\beta}$	$-\chi_k$	Zero steady-state step response, zero DC gain of freq. response.

is found next. The mixed transfer function is calculated according to (2.17). Finally, the effect of the mixing coefficient γ on the zeroes of the transfer function is investigated.

The process of incorporating of an ASM into a structure described in the preceding paragraph can be represented as a feedback problem illustrated in Figure 2.4. A static model of the ASM which can be used in the ASM block was given in (2.25).

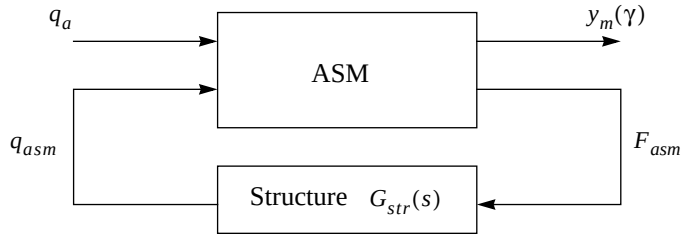

Figure 2.4 ASM/structure integration can be cast as a feedback problem.

The feedback point of view offers insight into the motion of the poles and zeroes of the closed loop system shown in Figure 2.4. The structure is represented in transfer function

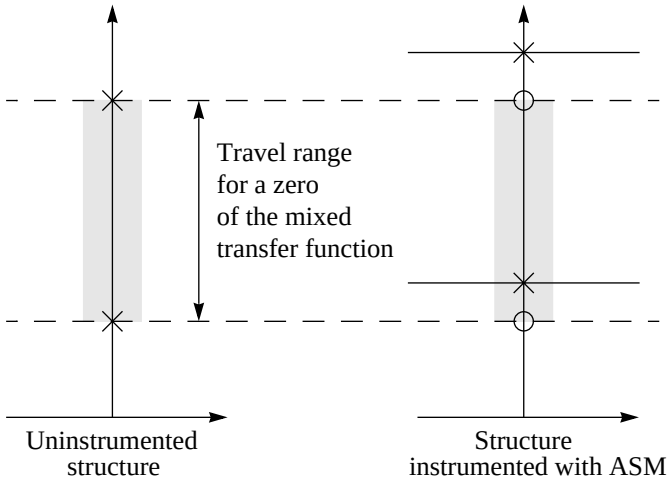

Figure 2.5 An illustration of the relationship between the poles of the original uninstrumented structure, the zeroes of the force transfer function and the travel range for the zeroes of the mixed transfer function.

form as $G_{str} = N_{str}/D_{str}$ and the ASM is described by a transfer function matrix,

$$\begin{bmatrix} y_m \\ F_{asm} \end{bmatrix} = \frac{1}{D_{asm}} \begin{bmatrix} N_1 & N_2 \\ N_3 & N_4 \end{bmatrix} \begin{bmatrix} q_a \\ q_{asm} \end{bmatrix} \tag{2.38}$$

It can be seen from Table 2.1 that the zeroes of the mixed transfer function are bounded from above and below by the zeroes of the force transfer function. More information can

be obtained about the force transfer function by considering the numerator of the closed-loop transfer function from the ASM input q_a to the force F_{asm}. It is equal to $N_{FQ}D_{asm}D_s$, indicating that the zeroes of this transfer function are equal to or, for the case of a dynamic ASM model, include the poles of the original structure. This fact is illustrated Figure 2.5 where the zeroes of the force transfer function (circles) are located on the same horizontal line as the poles of the original structure (crosses). Therefore the bounds on zeroes of the mixed transfer function are set by the poles of the uninstrumented structure.

2.1.3 Zero Trajectory Plot

Since the objective of building the ASM is to gain control of the mixed transfer function zeroes it is useful to construct a plot of the behavior of these zeroes versus the primary controllable parameter γ. A simplified sketch of such a trajectory is shown in Figure 2.6. The sketch is a summary of the information gathered so far from examining the static model of the actuator-sensor module (ASM).

The following parameters which influence the mixed output have been identified thus far: (i) the mixing coefficient γ, (ii) the normalized strain sensor stiffness α, (iii) the normalized force sensor stiffness β, and (iv) the non-dimensional stiffness parameter χ_k characterizing the relative stiffness of the ASM and the structure and defined in (2.34). Out of these four parameter only the mixing coefficient γ is a variable intended to be used as the control knob for adjusting the zeroes of the mixed transfer function. The rest of the parameters are fixed once the structure and the ASM are mechanically designed.

The poles of the uninstrumented structure are shown as dashed horizontal lines. Obviously, their frequencies are unaffected by any variations in the ASM and the ends of the dashed lines are shown “fixed” symbolizing independence from the four parameters listed above. The poles of the structure with the ASM mounted are shown as solid horizontal lines. The structure can only be stiffened as a result of adding the ASM, therefore the natural frequencies of the instrumented structure are shown above the original ones. The

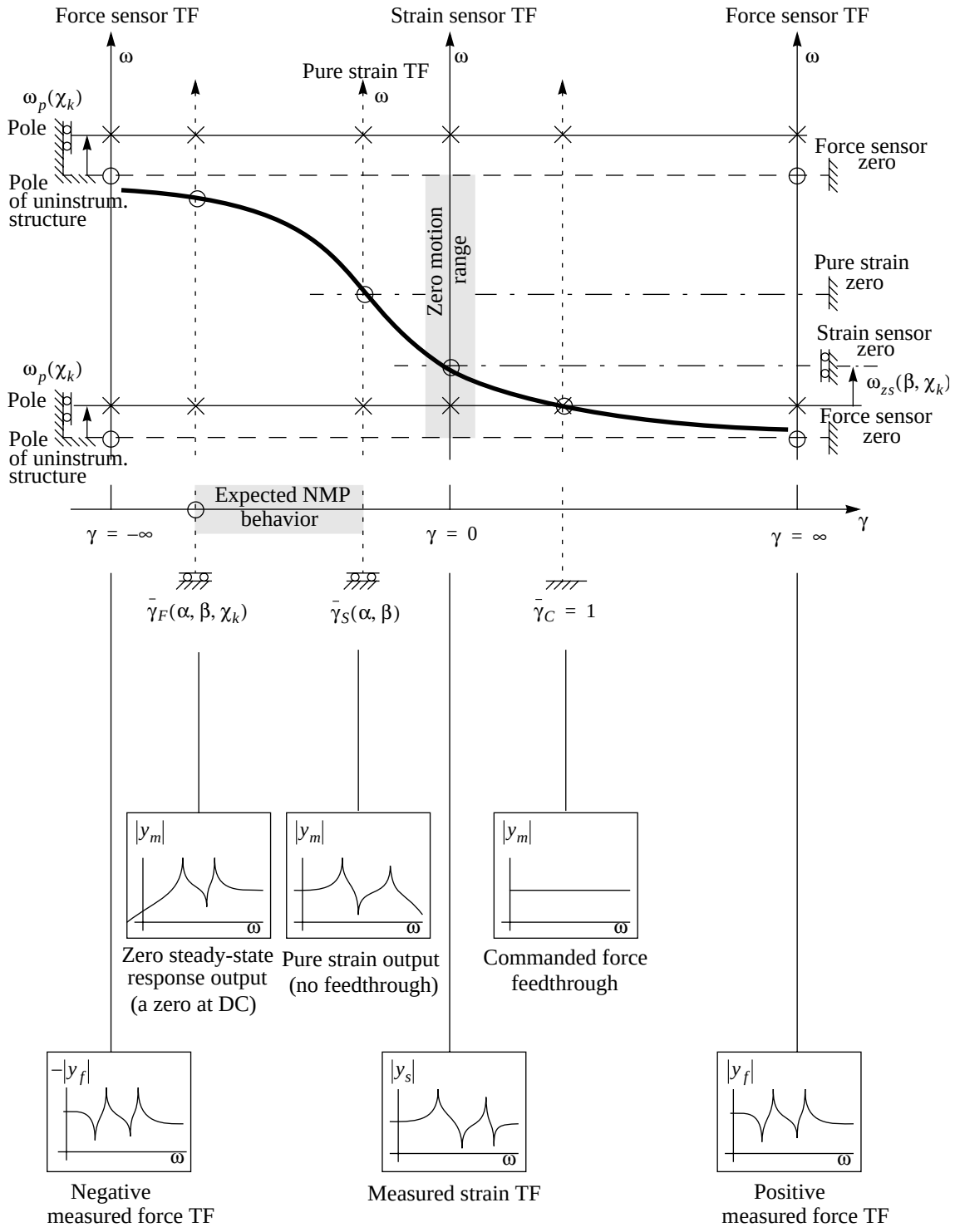

Figure 2.6 Expected shape of the zero trajectory for one mode of the mixed transfer function, monotonic change in zero frequency is assumed; also shown are the interpretations of the special values of the mixing coefficient in terms of the mixed transfer functions they produce.

increase in natural frequencies depends only on the stiffness parameter χ_k. The dependence of the poles of the instrumented structure on at least one of the system parameters (other than γ) is illustrated by the “rollers” attached to the tips of the solid lines.

It was shown in the previous section that the poles of the uninstrumented structure become the zeroes of the measured force transfer function after an ASM is attached, which in turn serve as bounds on the zeroes of the mixed transfer function. Therefore the dashed horizontal lines also mark the region of possible vertical motion of the zeroes of the mixed transfer function. Next, the special values of the mixing coefficient summarized in Table 2.1 are located on the plot. The special values for the case of balanced output are used ($\bar{\gamma}_F, \bar{\gamma}_S, \bar{\gamma}_C$) because they offer better insight into zero frequency dependencies. In practical application, however, the unbalanced form, also given in Table 2.1, is more likely to be used as is done in Chapter 4.

The intersection of the zero trajectory with the $\gamma = 0$ axis is known to occur at the zero of the measured strain sensor transfer function. From (2.12) it is clear that the strain sensor zero depends on the load cell stiffness β. Also, the presence of the feedthrough term and the fact that the poles of the $\frac{q_{asm}}{q_a}$ transfer function depend on the relative stiffness parameter χ_k mean that the zeroes of the measured strain sensor transfer function depend on χ_k as well. Therefore $\omega_{zs} = \omega_{zs}(\beta, \chi_k)$ as shown on the right hand side of the plot.

For large positive and negative values of γ, the zero trajectory approaches the values of the zeroes of the force transfer function. As was shown previously, the zeroes of the measured force transfer function are equal to the poles of the uninstrumented structure and serve as bounds for the zeroes of the mixed transfer function.

Pole-zero cancellation occurs at $\gamma = \bar{\gamma}_C = 1$ irrespective of all the parameters listed above. Note that this applies to all modes of the system and so all poles and zeroes are expected to cancel at the same time. Consequently, the alternating pole-zero pattern assumed for the individual strain and force transfer functions is preserved in the mixed transfer function. A pole-zero-pole pattern of the strain sensor transfer function transitions

through a pole-zero cancellation into a zero-pole-zero pattern of the force transfer function. This observation supports the intuitive notion that a linear combination of two collocated transfer functions should itself be collocated [Fleming, 1990].

For $\gamma = \bar{\gamma}_S$ the mixed transfer function measures pure strain and contains no feedthrough. Turning the argument in the previous paragraph around, the zeroes of the pure strain transfer function do not depend on any of the parameters under consideration because of the absence of the feedthrough term. The mixing coefficient for which the pure strain signal is achieved depends on the α and β according to (2.27).

The mixing coefficient $\bar{\gamma}_F$ by definition corresponds to the transfer function with a zero at DC which is shown on the plot. Note that the two poles in the plot do not necessarily correspond to the first and the second mode, and the vertical axes are considered discontinuous below the frequency of the lower pole. Note also that $\bar{\gamma}_F$ is the only special mixing gain which depends on the relative structure-ASM stiffness parameter χ_k according to (2.36).

Once the zeroes for all the special values of γ are marked on the plot, they were connected with a smooth curve. In doing so it was *assumed* that between the known points the zero trajectory varies monotonically. While this result was not proven in general, for the structures considered later in this chapter this assumption is validated.

Small transfer function cartoons are shown at the bottom of Figure 2.6 as reminders of the physical meaning of the special values of the mixing coefficients. The transfer functions in the sketches represent a typical 2-DOF system. The transfer function with γ_F has a zero at DC, γ_S eliminates the feedthrough term, and γ_C is just a static feedthrough.

Fleming, who considered a mass-spring system which can be put into a form consistent with the present ASM approach, reported non-minimum phase (NMP) zeroes for a range of negative mixtures [Fleming, 1990]. At this point, physical arguments will be given to help identify the range of the mixing coefficients which may lead to transfer functions

with NMP behavior. Because NMP zeroes are an important (and undesirable) feature of any plant, special attention will be given to their presence while modeling sample structures later in this chapter.

The tell-tale sign of non-minimum behavior in a system is the difference between the signs or directions of the initial response and the steady-state value. In steady state (or statically) the module acts against the stiffness of the structure putting the strain sensor in tension and the force sensor in compression. The signs for both sensors were chosen such that the output signals are positive for static actuation. The sings of the sensor signals in initial response are also positive because at first the module acts against the inertia of the mass and the sensor deformations are same as above.

Since all signs of the initial and final response for both sensors are positive, no positive mixing coefficient can lead to NMP behavior. For negative mixing coefficients a possibility of sign mismatch exists. An important observation is that the force signal always leads pure strain signal, because the force is the cause of deformation and the deformation lags behind due to inertial effects. The onset of NMP behavior, at least for finite-dimensional systems, occurs at the point of pure strain output, i.e. $\gamma = \gamma_S$. For the mixing coefficients just to the left from γ_S the initial response of the mixed transfer function is negative but the final value is still positive because in finite amount of time the structural mass catches up to the commanded displacement and the mixed signal returns to positive.

The region of NMP behavior ends at the point where the steady-state value of the mixed transfer function becomes negative as well. At the transition point is the mixture whose output in steady state is zero. The corresponding mixing gain was designated earlier as γ_F. It was pointed out by Fleming that if the mixed output is used for feedback control, the sign of the controller has to be reversed when crossing over the γ_F point.

To summarize, the values $\bar{\gamma}_F$ and $\bar{\gamma}_C$ mark the boundaries outside of which the force transfer function dominates the mix. In particular, the sign of the steady-state value of the step response of the system with mixing coefficient outside the bounds is equal to the sign

of the mixing coefficient. The region between $\bar{\gamma}_F$ and $\bar{\gamma}_s$ is characterized by the force signal dominating initially and the strain sensor signal overtaking in finite amount of time.

Summary

In this section a general form of the actuator-sensor module (ASM) with provisions for obtaining arbitrary actuator and sensor impedances was proposed. When compared to typical single-sensor configurations, the two-sensor approach makes it possible to adjust the apparent sensor impedance of the virtual sensor created by combining the outputs of two sensors. A simple static model of the ASM was constructed which captures important relationships between relative actuator and sensor stiffnesses, mixing gain and the transfer function characteristics. Several special values of the mixing coefficient were identified.

A general strategy of integrating an ASM into a structure was outlined. In the next three sections this strategy will be applied to representative lumped and distributed systems. It was shown that the bounds on the travel of the zeroes of the mixed transfer function are set by the poles of the uninstrumented structure.

ASM output properties derived from the static model were summarized in a sketch of the expected shape of the zero trajectory. This important sketch in Figure 2.6 will be compared to the zero trajectory plots for the structures modeled later in this chapter and to the experimental results presented in Chapter 4.

2.2 Lumped Parameter System

In this section the actuator-sensor module (ASM) described and modeled in the preceding section is connected to a simple mass and spring system. The simplicity of the structural system allows to calculate analytical transfer functions, and the transfer function poles and zeroes. The goal of this section is to verify the features of the mixed zero trajectories predicted in the previous section. The qualitative results of the previous section on the dependence of pole/zero spacing of the strain sensor transfer function are quantified by

considering a specific structure. The interaction between the effects of output mixing and the ASM design parameters is explored.

Model

A lumped-parameter system under consideration is shown in Figure 2.7a. It includes two structural stiffnesses modeled as springs and two masses. An ASM is attached in parallel with one of the structural springs with one end attached to the rigid constraint. Similar systems were analyzed in the past by [Fanson, 1989] in relation to the problem of active isolation applied to a truss structure and by [Fleming, 1990] in the investigation of the effects of actuator and sensor impedances on the pole-zero patterns.

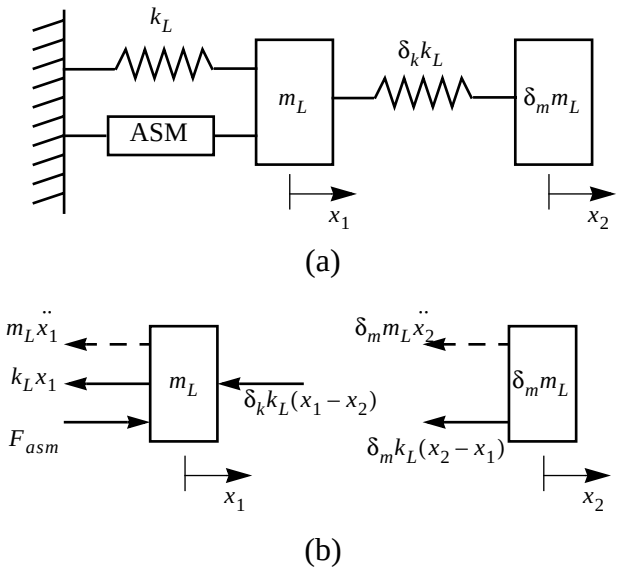

Figure 2.7 Mass-spring system with an actuator-sensor module (ASM): (a) schematic; (b) free-body diagrams.

Free body diagrams are shown in Figure 2.7b. Note that because of the simplicity of this problem the ASM stiffness is directly integrated into the system equations. Alternatively, the feedback approach combining the model of the structure and the ASM model described in Section 2.1 can be employed. Recognizing the ASM deformation for this sys-

tem as $q_{asm}^{L} = x_1$ and substituting it into the expression for the force produced by the ASM F_{asm} given in (2.10), the system dynamics equations are found as,

$$\begin{bmatrix} 1 & 0 \\ 0 & \delta_m \end{bmatrix} \begin{bmatrix} \ddot{x}_1 \\ \ddot{x}_2 \end{bmatrix} + \omega^2 \begin{bmatrix} (\chi_k^L + 1 + \delta_k) & -\delta_k \\ -\delta_k & \delta_k \end{bmatrix} \begin{bmatrix} x_1 \\ x_2 \end{bmatrix} = \omega^2 \begin{bmatrix} \frac{1}{1+\alpha}\chi_k^L \\ 0 \end{bmatrix} \begin{bmatrix} q_a \end{bmatrix} \tag{2.39}$$

where $\omega^2 = \frac{k_L}{m_L}$ is a characteristic frequency of the structure, and χ_k^L is a non-dimensional stiffness parameter characterizing the relative stiffness of the ASM and the structure. The superscript stands for *lumped.* This is the same parameter introduced in (2.34) specialized for this particular lumped parameter system.

$$\chi_k^L = \frac{k_0}{k_L} \tag{2.40}$$

Input-Output Transfer Functions

The measurement equations for the strain, force, and virtual sensors (2.12, 2.15, 2.21) are modified by substituting q_{asm}^{L}. The transfer function from the ASM input to the virtual sensor output is given as an example.

$$y_m = \frac{\beta(1-\gamma)}{1+\alpha+\beta} x_1 + \frac{1+\alpha+\beta\gamma}{(1+\alpha)(1+\alpha+\beta)} q_a \tag{2.41}$$

Analytical transfer functions from the ASM input to the mass displacements x_1 and x_2 are found by taking the Laplace transform of the second order differential equations (2.39) and solving the resulting linear algebraic system. The expressions are simplified if all structural stiffnesses and masses are set to be the same, i.e. $\delta_k = 1$ and $\delta_m = 1$. The analytical transfer function from the ASM input to the displacement of the first mass is substituted into the measurement equations for the strain and force sensors.

$$\frac{y_s(s)}{q_a(s)} = \left(\frac{1}{1+\alpha+\beta}\right) \frac{s^4 + \left[3 + \chi_K \frac{1+\alpha+\beta}{1+\alpha}\right]\omega^2 s^2 + \left[1 + \chi_K \frac{1+\alpha+\beta}{1+\alpha}\right]\omega^4}{s^4 + [3+\chi_k]\omega^2 s^2 + [1+\chi_k]\omega^4} \tag{2.42}$$

The force sensor transfer function is adjusted by pre-multiplying it by the output matching coefficient $\bar{\chi}_y$ from (2.20).

$$\frac{\bar{y}_f(s)}{q_a(s)} = \bar{\chi}_y \frac{y_f(s)}{q_a(s)} = \left(\frac{\beta}{(1+\alpha)(1+\alpha+\beta)}\right)\frac{s^4 + 3\omega^2 s^2 + \omega^4}{s^4 + [3+\chi_k]\omega^2 s^2 + [1+\chi_k]\omega^4} \tag{2.43}$$

Notice that the denominator of the transfer function depends on the stiffness parameter χ_k. The numerator of the strain sensor transfer function also depends on χ_k and on the load cell stiffness β. In addition, it depends on the strain sensor α which could not be seen from the preliminary analysis in the Section 2.1.3. As expected the numerator of the force transfer function does not change.

Because the main focus of this work is the modification of the sensor impedance, the actuator impedance is eliminated from the list of design variables by matching the equivalent ASM stiffness to the static driving point impedance of the structure, in this case simply the spring in parallel with the ASM, i.e. $\chi_k^L = \bar{\chi}_k^L = 1$, where $\bar{\chi}_k^L$ is a special value of the relative stiffness coefficient χ_k^L corresponding to the case of the ASM stiffness matched to the stiffness of the structure.

Transfer functions from the actuator input to the outputs of the strain and force sensors as described in (2.42, 2.43) with impedance matching performed are plotted in Figure 2.8 for typical values of the strain and force sensor stiffnesses. Notice that the magnitudes of the two transfer functions are approximately equal due to the output matching coefficient $\bar{\chi}_y$.

Following the same procedure, the analytical transfer function from the ASM input to the mixed output for the impedance-matched module and structure is found as,

$$\frac{\bar{y}_m(s)}{q_a(s)} = \left(\frac{1+\alpha+\beta\gamma}{(1+\alpha)(1+\alpha+\beta)}\right)\frac{s^4 + (4+\tau)\omega^2 s^2 + (2+\tau)\omega^4}{s^4 + 4\omega^2 s^2 + 2\omega^4} \tag{2.44}$$

where $\tau = \frac{\beta(1-\gamma)}{1+\alpha+\beta\gamma}$. The polynomials in the numerator and the denominator of the transfer function are of the same order in the Laplace variable s due to a nonzero

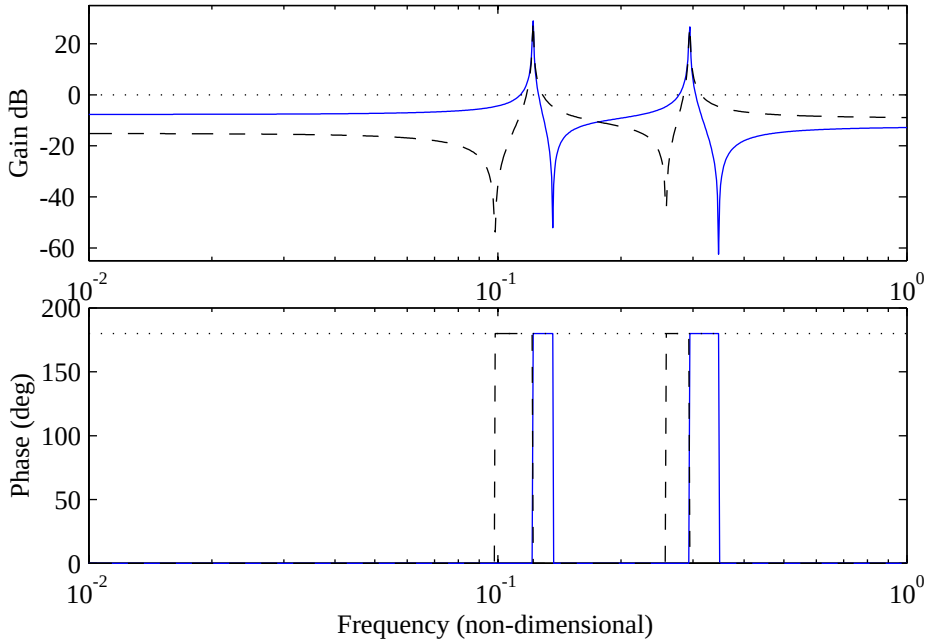

Figure 2.8 Sample strain (solid) and force (dashed) transfer functions for an ASM connected to a mass-spring system, $\alpha = 0.7$ and $\beta = 2.5$.

feedthrough term in (2.41). Note also that, as expected, the numerator of (2.44) depends on the mixing coefficient γ, while the denominator does not.

A typical plot of zero trajectories is shown in Figure 2.9. The plot closely follows the form of the sketch in Figure 2.6 constructed on the basis of general ASM properties. The zeroes of the mixed transfer function are plotted as dots. Zero trajectory branches corresponding to individual modes are easily identifiable. The imaginary and real parts of poles and zeroes are plotted separately. In this example the structure is undamped, so only the real-valued zeroes of the mixed transfer function are visible in the bottom plot. The assumption regarding monotonic zero motion holds for the case of a lumped-parameter system. Observation from the plot specific to the lumped parameter system are discussed below.

Note that for the mixing coefficients to the left from $\bar{\gamma}_F$ (and to the right from $\bar{\gamma}_C$) the mixed transfer function display the zero-pole-zero-pole pattern characteristic of the force transfer function.

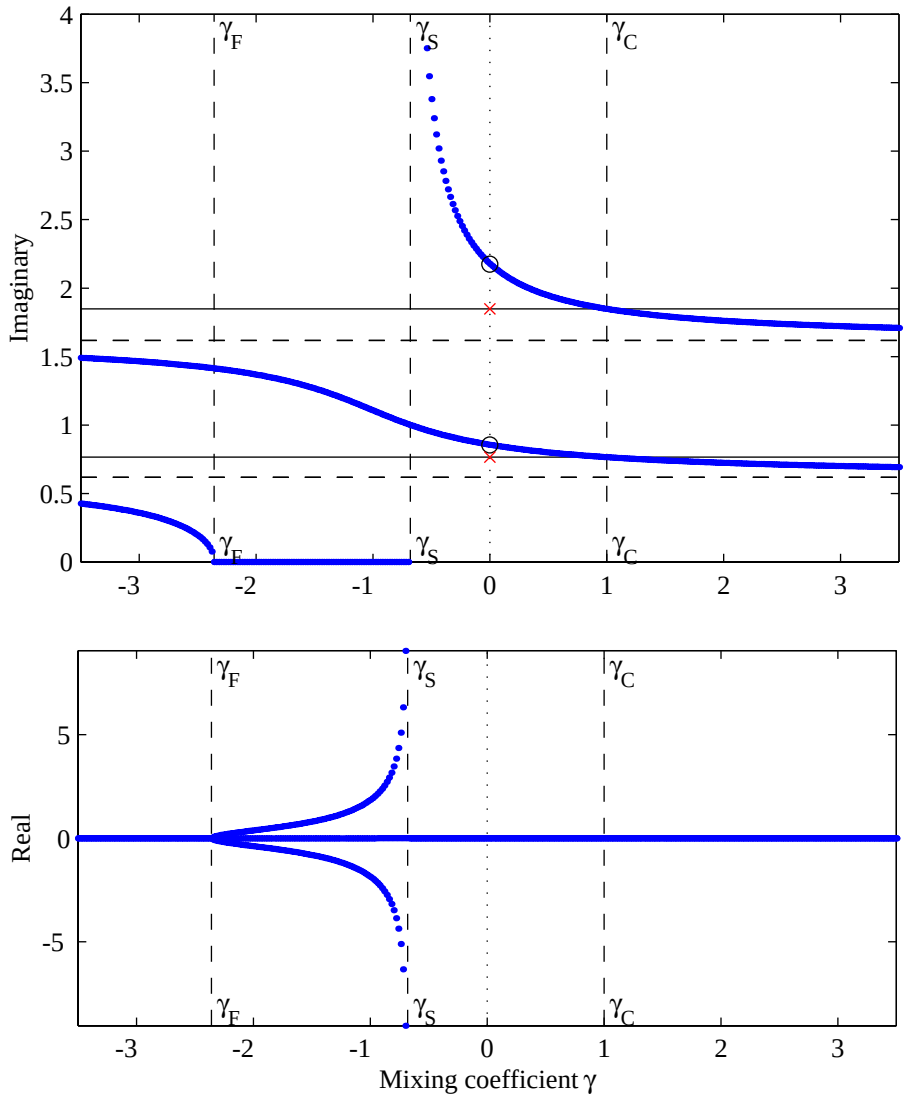

Figure 2.9 A typical zero trajectory plot for a mass-spring system with an in-line ASM; $\alpha = 0.7$, $\beta = 2.5$.

Mathematically, the coefficient corresponding to the pure strain transfer function leads to a division by zero in the numerator parameter τ. The discontinuity in the zero trajectories caused by division by zero leads to a characteristic asymptotic behavior in the vicinity of $\bar{\gamma}_S$. With γ approaching $\bar{\gamma}_S$ from above, the feedthrough term approaches zero while the faster zero pair approaches infinity along the imaginary axis. For $\gamma = \bar{\gamma}_S$, the feedthrough term is exactly zero, the faster zero pair is at infinite frequency, and it is the only instance

of the transfer function with only two zeroes. For the values of γ to the left from $\bar{\gamma}_S$, the transfer function acquires a pair of real-valued nearly-symmetric zeroes, one minimum phase (MP) and one non-minimum phase (NMP). With γ approaching $\bar{\gamma}_S$ from below, the MP zero approaches negative infinity and the NMP zero positive infinity.

The presence of a NMP zero is difficult to identify on the Bode plot because the phase contribution of a pair of nearly symmetric MP and NMP zeroes is negligible. However, a time simulation of the system with the mixing coefficient set in the range between γ_F and γ_S shown in Figure 2.10 reveals the characteristic behavior: the sign of the initial response is opposite to the sign of the steady-state value.

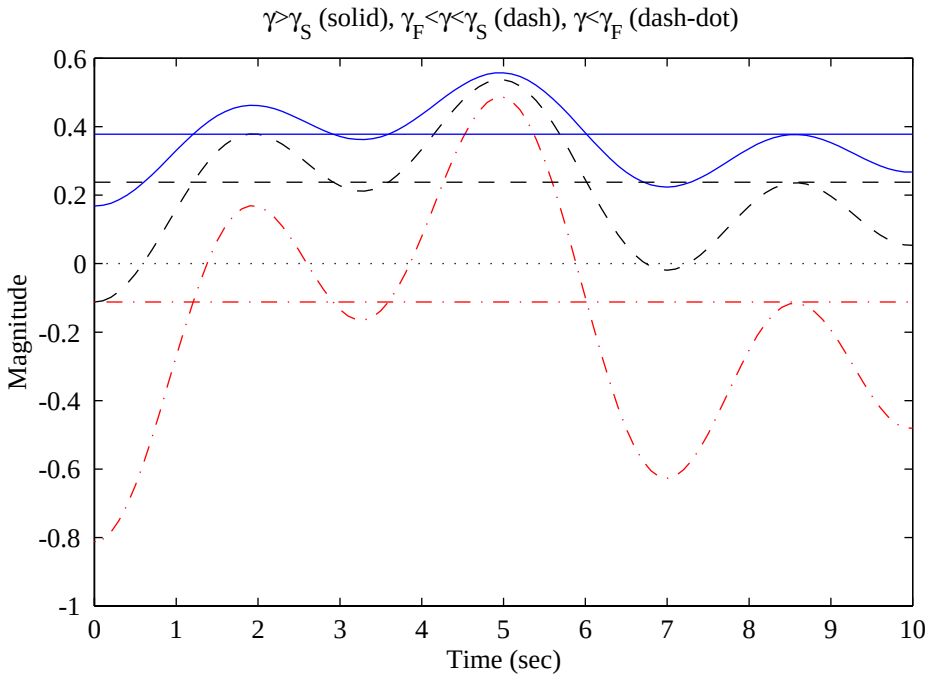

Figure 2.10 Step response of the mass-spring system with $\bar{\gamma} = -0.5$ (solid), $\bar{\gamma} = -1.0$ (dashed), and $\bar{\gamma} = -2.8$ (dash-dot) demonstrates NMP behavior of the system with the mixing coefficient $\bar{\gamma} = -1.0$ between $\bar{\gamma}_R$ and $\bar{\gamma}_S$. Steady state values are shown as horizontal lines with the same line styles as the corresponding time responses.

A different representation of the motion of the zeroes of the mixed transfer function is shown in Figure 2.11. It plots the zero locus in s-plane with the mixing coefficient as a parameter. The zeroes of the mixed transfer function are shown as dots. The poles of the

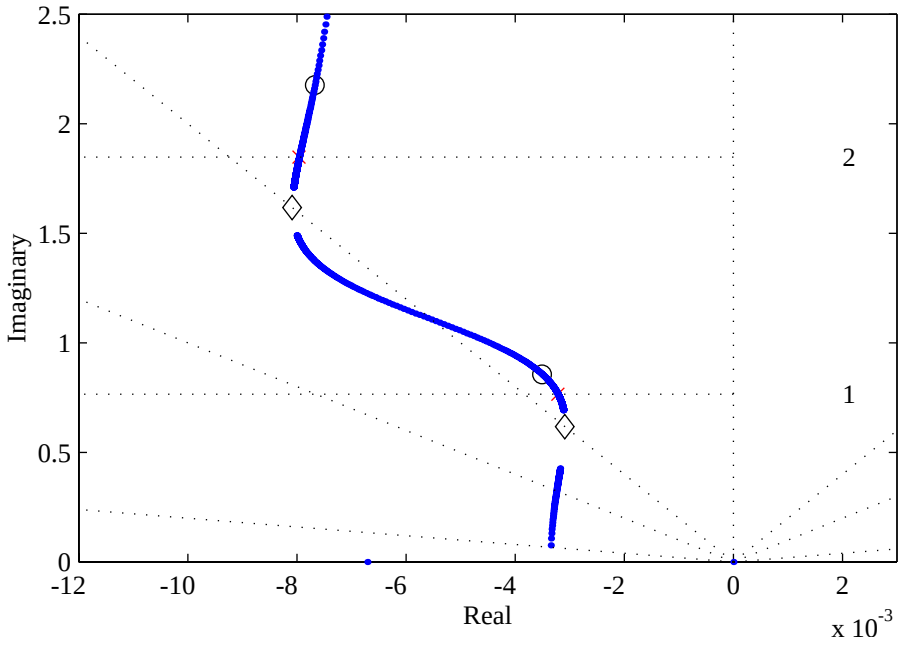

Figure 2.11 Zero locus of the mixed transfer function of an ASM connected to a mass-spring system; also shown are the system poles (crosses), strain sensor zeroes (circles), and force sensor zeroes (diamonds).

system are shown as crosses. The zeroes of the individual strain and force sensor transfer functions are shown with circles and diamonds respectively. The concentric grid lines correspond to the frequency of the two modes. The radial dashed lines are lines of constant damping marking 0.5, 1, and 5 % damping. The modal damping of the structure for this plot was arbitrarily set to 0.5% and then reduced slightly in the process of closing the feedback loop around the ASM mixed transfer function (see Section 2.1).

The plot highlights the change in zero damping for different values of the mixing coefficient. The important observation is that the zero locus never crosses the zero-damping line indicating that the mixed output of an ASM attached to a mass-spring system does not produce non-minimum phase complex zeroes.

Zero Dependence on the Stiffness of ASM Components

The explicit form of the transfer functions to strain, force, and mixed outputs in (2.42, 2.43, 2.44) offers insight into the pole and zero dependence on the relative stiffnesses of the strain and force sensors and their interaction with the output mixing coefficient which is the primary variable of interest. The pole-zero spacing in the three transfer functions is considered in turn.

The amount of pole-zero separation in the *strain sensor* transfer function depends strongly on the relative stiffness of the load cell. The zeroes approach poles as the load cell's normalized stiffness is reduced. This property of pole-zero cancellation due to a finite driving point compliance was pointed out by Fanson in the discussion of a two-spring model of an active truss member [Fanson, 1989]. As an illustration, a plot of zero-to-pole ratio in the first mode as a function of the strain and force sensor normalized stiffnesses is shown in Figure 2.12. The ratio of the pole and zero frequencies approaches unity as the load cell

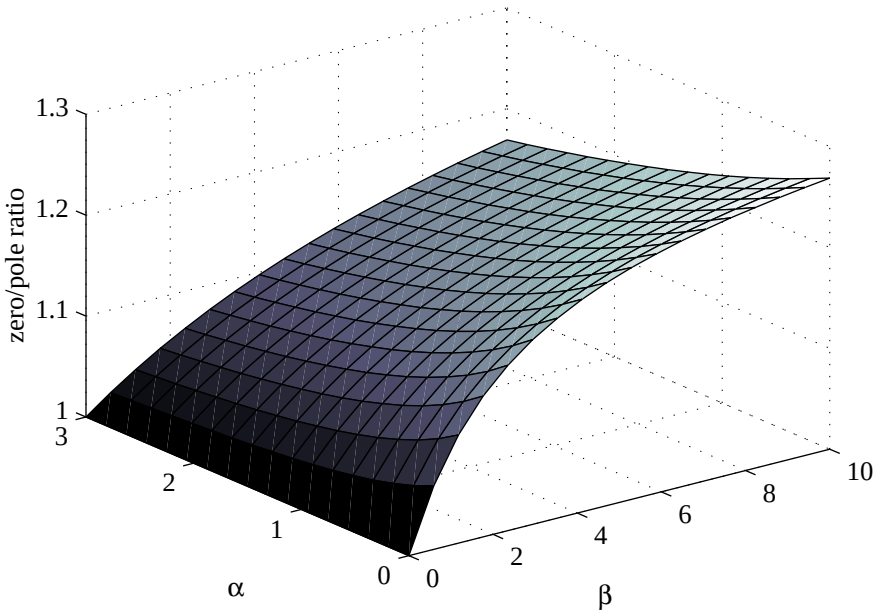

Figure 2.12 Pole-zero separation in the strain sensor transfer function as a function of strain sensor and load cell stiffnesses for an ASM attached to a mass-spring system.

stiffness is reduced to zero. The surface also shows a weak inverse dependence on the strain sensor stiffness, i.e. pole-zero separation is improved with a softer strain sensor. It is clear from this plot that if the strain sensor transfer function is to be used for feedback by itself, than the best pole-zero separation is achieved for a stiff load cell and a soft strain sensor.

When the strain sensor transfer function is expressed as a sum of the pure strain and force signals, it appears to offer an opportunity of changing the sensor impedance without output mixing. However, on closer examination this approach is limited in range and only allows positive mixtures, whereas the output mixing does not have these limitations. Figure 2.12 shows the limited range in which the pole-zero spacing in the strain sensor transfer function can be adjusted by changing the ASM component stiffnesses alone.

The zeroes of the *force sensor* transfer function in (2.42) do not depend on the ASM stiffness. As was shown earlier they are equal to the poles of the uninstrumented structure. The amount of pole-zero separation, however, does depend on the relative structure-ASM stiffness parameter χ_k^L because it effects the poles of the combined system. The softer the actuator-sensor module the closer are the poles and the zeroes in the force transfer function. In the limit, for $\chi_k^L = 0$, the poles and zeroes of the force transfer function cancel. If the force transfer function is to be used for feedback by itself, than better pole-zero separation is achieved for a stiffer ASM. Throughout this work the impedances of the structure and the actuator-sensor module are matched as was done for the current system by setting $\chi_k^L = 1$.

The zeroes of the *mixed* transfer function depend on both strain and force sensor relative stiffnesses as can be seen from (2.44). The zero trajectory plot in Figure 2.9 was created using “typical” values of component stiffness. A surface plot representing the motion of a zero of the mixed transfer function for different values of the mixing coefficient and load cell stiffness is shown in Figure 2.13. The zero trajectory plot in Figure 2.9 represents a slice through the surface at the point $\beta = 2.5$. A similar surface plot of zero dependence

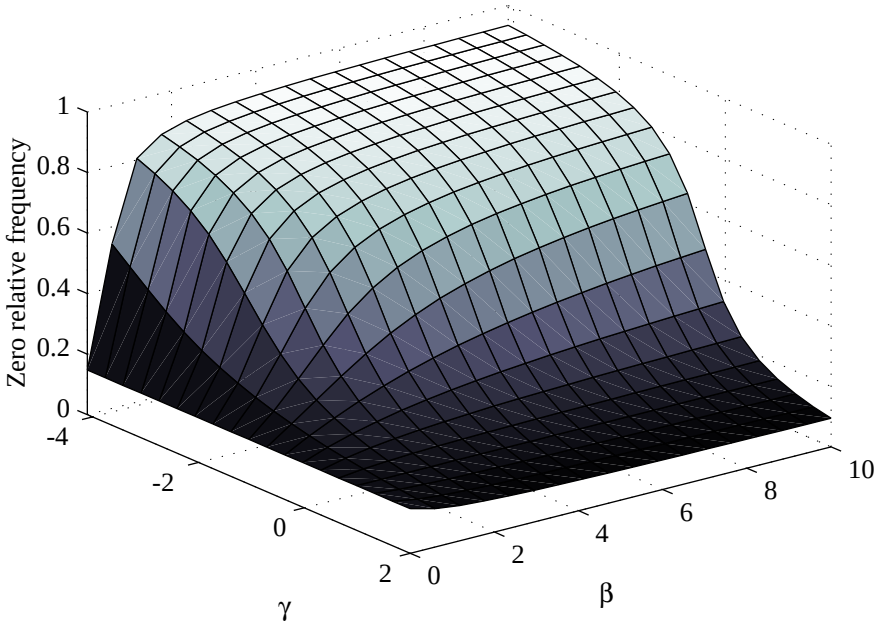

Figure 2.13 Mixed transfer function zero dependence on the mixing coefficient γ and the relative *load cell* stiffness β plotted normalized between 0 and 1 within the bounds imposed by the zeroes of the force transfer function; $\alpha = 0.7$.

on the mixing coefficient and the strain sensor stiffness is shown in Figure 2.14. The plot in Figure 2.9 represents a slice through the surface at the point $\alpha = 0.7$.

The dependence of the zeroes of the mixed transfer function on the strain sensor stiffness is not as pronounced as on the stiffness of the load cell. In either case, it is safe to conclude that for a moderately stiff force sensor, i.e. $\beta > 2$, and a sufficiently soft strain sensor, i.e. $\alpha < 1.0$, the appearance of zero trajectories only weakly depends on the exact relative stiffness of the ASM components.

Summary

In this section a simple two-degree-of-freedom lumped parameter structure coupled with an actuator-sensor module was modeled and analyzed. Closed form expressions for the transfer functions to strain, force, and mixed output were found.

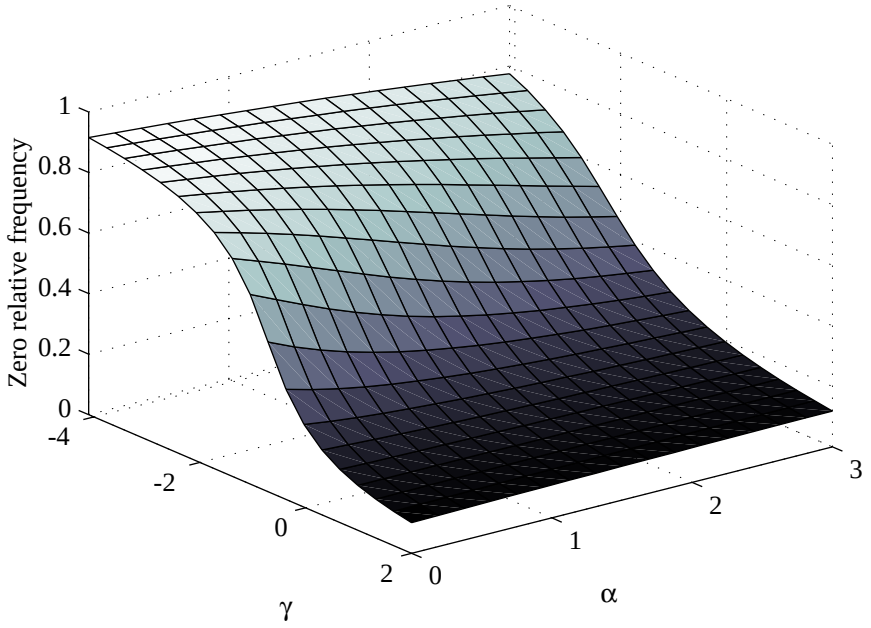

Figure 2.14 Mixed transfer function zero dependence on the mixing coefficient γ and the relative *strain sensor* stiffness α measured as a relative position within the bounds imposed by the zeroes of the force transfer function; $\beta = 2.5$.

Zero trajectory plot was constructed and its appearance verified the features predicted previously based on the general properties of the ASM. The assumption of monotonic motion of zeroes between the bounds is confirmed for the case of mass-spring system.

The amount of pole-zero spacing – an important metric in this study – was found to depend strongly on the output mixing coefficient. This is a promising result for using output mixing as a tool for obtaining the desired pole-zero separation in a structural transfer function. In addition zero dependence on the internal ASM stiffnesses was examined and found to be a secondary effect for reasonable values of the strain and force sensors.

Non-minimum phase (NMP) real-valued zeroes were observed for the output mixtures between $\bar{\gamma}_R$ and $\bar{\gamma}_S$. They appeared in nearly-symmetric real MP and NMP pairs. The following sections discussing more realistic structures will attempt to determine whether these zeroes should be expected to be encountered in practice.

2.3 Finite-Dimensional Models of Beams

In this section the results on the effects of output mixing on transfer function zeroes obtained for a lumped-parameter system are extended to a representative distributed system. The assumed-mode method is used to obtain an approximate solution for the systems' frequency response with the objective of finding the trajectories of the zeroes of the mixed transfer function. In the following section the same structures will be analyzed again to obtain the exact solution of the partial differential equation.

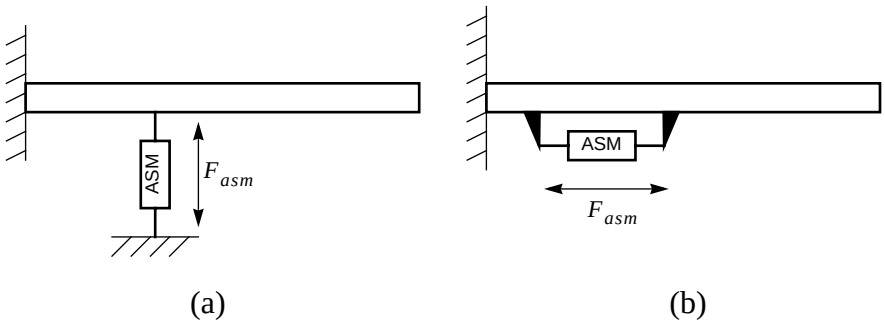

Figure 2.15 Two actuation methods used with an actuator-sensor module on a beam: (a) force actuation and transverse deformation sensing; (b) moment actuation and deformation slope sensing.

A uniform cantilever beam is used as an example of a typical continuous system. An actuator-sensor module (ASM) modeled in Section 2.1 is attached to a point along the span of the beam. The first subsection outlines the general procedure for finding an approximate solution for the beam vibration problem. In the following subsections two actuation configurations are considered. In the first configuration, shown in Figure 2.15a, the ASM is positioned perpendicular to the beam. The actuator exerts a transverse *force* and the strain sensor measures transverse *displacement* at the driving point on the beam. In the second, shown in Figure 2.15b, the ASM is placed parallel to the beam. The actuator exerts a bending *moment* and the strain sensor measures the deformation *slope* of the beam at the driving point. Finally, the modeling results for the two configurations are summarized and compared to each other in the last subsection.

2.3.1 Application of the Assumed-Mode Method to Beam Vibrations

The assumed mode method is used to find the approximate input-output transfer function for the ASM attached to a beam. In the assumed method the response of a continuous system is represented by a sum of a finite number of assumed mode shapes [Meirovitch, 1975],

$$w(x, t) = \sum_{i}^{n} \psi_i(x) q_i(t) \tag{2.45}$$

where $\psi_i(x)$ are trial functions and $q_i(t)$ are generalized coordinates. The trial function must satisfy the geometric boundary conditions only, since the natural boundary conditions are accounted for in the expressions for the kinetic and potential energies. For the solution to be accurate and the convergence speed to be acceptable, it is desirable that the trial functions span or nearly span the solution space. The structures considered in this section are perturbations of a uniform cantilever beam, and so the exact mode shapes of a uniform cantilever Bernoulli-Euler beam are used as trial functions [Meirovitch, 1975].

It has been shown that the inclusion of static deformation shapes into the set of assumed modes improves convergence characteristics of the approximate solution. In particular it helps accurately model the zero frequencies [Hagood, 1988, Fleming, 1990]. The set of trial functions is therefore augmented with one static deformation shape found separately for each loading case.

The expressions for the kinetic and potential energies in terms of generalized coordinates and the work done by the external forces are formulated and substituted into Lagrange's equation,

$$\frac{d}{dt}\left(\frac{\partial T}{\partial \dot{q}_i}\right) - \frac{\partial T}{\partial q_i} + \frac{\partial U}{\partial q_i} = Q_i(i) \tag{2.46}$$

where T' is the kinetic energy, U is the potential energy, and Q_i are the generalized forces. The result can be written in the form

$$M\ddot{q} + Kq = Q \tag{2.47}$$

where M and K are the mass and stiffness matrices respectively. In the two actuator configurations considered in this section, the kinetic and potential energies and the corresponding mass and stiffness matrices are the same and are derived in advance. The work done by the external forces is different for each configuration and will be derived for each case separately.

Exact expressions for the kinetic and potential energies of a vibrating beam are given below,

$$T = \frac{1}{2} mL \int_0^1 \left(\frac{\partial^2}{\partial t^2} w(\xi, t) \right)^2 d\xi \tag{2.48}$$

$$U = \frac{1}{2} \frac{EI}{L^3} \int_0^1 \left(\frac{\partial^2}{\partial \xi^2} w(\xi, t) \right)^2 d\xi \tag{2.49}$$

where m is constant linear density of the beam measured in [kg/m], EI is constant bending stiffness of the beam, and $\xi = x/L$ is a normalized coordinate along the span of the beam. For a concentrated external force, the work expression is written as,

$$W_{ext} = F_{ext} \delta w \tag{2.50}$$

Note that the external work includes a term quadratic in generalized coordinates which has to be moved to the left-hand side of Lagrange's equation and incorporated into the overall stiffness matrix. The quadratic term corresponds to the strain energy in the ASM equivalent stiffness and could have been included into the potential energy expression (2.49). Both approaches lead to the same result.

After substituting the trial function expansion (2.45) into the kinetic and potential energy expressions (2.48, 2.49), the elements of the mass and stiffness matrix are calculated as follows,

$$m_{ij} = mL\int_0^1 \psi_i(\xi)\psi_j(\xi)d\xi \tag{2.51}$$

$$k_{ij} = \frac{EI}{L^3}\int_0^1 \psi''_i(\xi)\psi''_j(\xi)d\xi \tag{2.52}$$

The system of equations resulting from Lagrange's equation is expressed in generalized (non-orthogonal) coordinates. For convenience, it can be transformed into normal coordinates in which the mass and stiffness matrices are diagonalized. The transformation matrix Φ is an eigenvector matrix associated with the homogeneous equation $M\ddot{q} + Kq = 0$. Performing coordinate transformation $q(t) = \Phi\eta(t)$ and pre-multiplying by Φ^T, a system of differential equations expressed in normal coordinates is found,

$$\eta_i + 2\zeta_i\omega_i\eta_i + \omega_i^2\eta_i = \phi_i^T Q \tag{2.53}$$

where ω_i and ζ_i are the natural frequency and damping of the i^{th} mode.

The outputs of the system are first written in terms of the physical variables and their spatial and temporal derivatives. The assumed solutions are then substituted, and the resulting equation transformed into the normal coordinates.

$$y = y(w, w', w'', \dot{w}, \ddot{w}) = S_q q + S_{\dot{q}}\dot{q} = S_q\Phi\eta + S_{\dot{q}}\Phi\dot{\eta} \tag{2.54}$$

The final step in the modeling process is the conversion of the system dynamics equation (2.53) and the measurement equation (2.54) into state-space representation of the form

$$\begin{aligned} \dot{x} &= Ax + Bu \\ y &= Cx + Du \end{aligned} \tag{2.55}$$

with the state vector $x^T = \left[\eta^T \ \dot{\eta}^T\right]$ and input u. The result is used to find the poles and the zeroes of the transfer function from the actuator input to the ASM mixed output. Note that the form of the A matrix in (2.56) implies constant modal damping which is assumed

here for simplicity, however, a more general proportional damping could have been easily used instead.

$$\begin{bmatrix} \dot{\eta} \\ \ddot{\eta} \end{bmatrix} = \begin{bmatrix} 0 & I \\ -\Omega^2 & -2\zeta\Omega \end{bmatrix} \begin{bmatrix} \eta \\ \dot{\eta} \end{bmatrix} + \begin{bmatrix} 0 \\ \Phi^T Q \end{bmatrix} [u]$$
$$y = \begin{bmatrix} S_q \Phi & S_{\dot{q}} \Phi \end{bmatrix} \begin{bmatrix} \eta \\ \dot{\eta} \end{bmatrix} + D[u] \tag{2.56}$$

The assumed mode method leads to an approximate solution expressed as a finite sum of modal responses. The exact solution expressed in modal form has an infinite number of modes. Higher modes not included in the model contribute a constant term at low frequencies. If the exact static solution is known then a correction procedure can be performed to find a static correction term which will make up for the DC contribution of the unmodeled modes [ref.].

The DC component of a state-space system like the one in (2.56) is written as $y_{DC} = -CA^{-1}B + D$. If the exact static solution y^e is known, then the static correction term D_{sc} can be found as the difference between the exact and the approximate solutions,

$$D_{sc} = y^e + CA^{-1}B - D \tag{2.57}$$

2.3.2 Fixed-Free Beam with an ASM as a Force Actuator

A configuration of a cantilever beam with an actuator-sensor module (ASM) placed perpendicular to the beam was previewed in Figure 2.15a and is shown again in more detail in Figure 2.16. The ASM of equivalent stiffness k_0 is attached to the beam at a distance ξ_a away from the clamp. The ASM is driven by a harmonic excitation with frequency ω and amplitude $\bar{q}_a$. The output of the ASM is adjusted with a mixing coefficient γ.

As was previously stated, the entire mass matrix and the stiffness matrix elements corresponding to the strain energy of beam deformation do not depend on the actuation method and were given in (2.51, 2.52). The generalized forces depend on the actuation method and

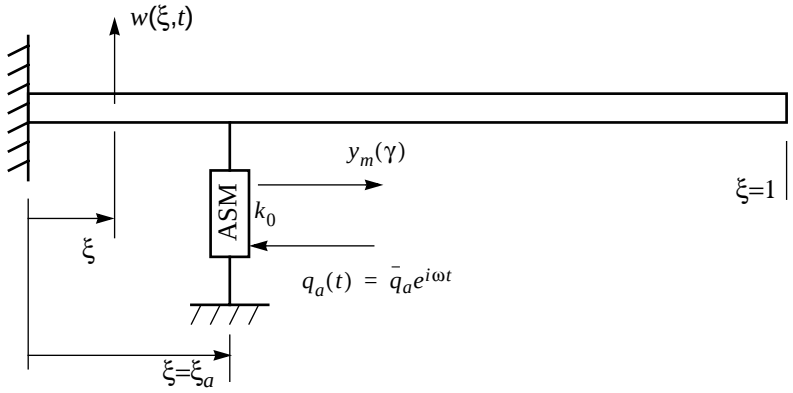

Figure 2.16 Fixed-free beam with ASM attached mid-span and acting as a force actuator and displacement sensor.

are derived in this subsection. Using the results of Section 2.1, the force F_{asm} exerted on the beam by the ASM at the point $\xi = \xi_a$ was found in (2.10).

The left end of the ASM is fixed, i.e. $q_1 = 0$, and the right end moves with the beam, i.e. $q_2 = w|_{\xi_a}$. The ASM deformation is calculated as

$$q_{asm}^F = w|_{\xi_a} \tag{2.58}$$

where the superscript stands for *force actuation.* The external work is then found as,

$$\delta W_{ext} = F_{asm}\delta w|_{\xi_a} = \left[-k_0 w|_{\xi_a} + \frac{1}{1+\alpha}k_o q_a\right]\delta w|_{\xi_a} \tag{2.59}$$

Substituting modal expansion (2.45), the expression for work performed by the external forces is expressed in terms of generalized coordinates and then separated into two components with quadratic and linear dependence on the generalized coordinates q_i. The first term contributes to the stiffness matrix K whereas the second leads to the generalized forces Q. In matrix form,

$$k_{ij}^F = 2k_0 \psi_i|_{\xi_a} \psi_j|_{\xi_a} \tag{2.60}$$

$$Q_i^F = \frac{1}{1+\alpha} k_o d\gamma_i\big|_{\xi_a} \tag{2.61}$$

Substituting expressions for the mass matrix (2.51), the combined stiffness matrix (2.52, 2.60), and the generalized forces (2.61) into Lagrange's equation and dividing through by mL, the mass matrix M, stiffness matrix K, and the generalized force vector Q are obtained,

$$\begin{aligned} m_{ij} &= \int_0^1 \psi_i \psi_j d\xi \\ k_{ij} &= a^2 \left(\int_0^1 \psi''_i \psi''_j d\xi + \frac{6}{\xi_a^3} \chi_k^F \psi_i\big|_{\xi_a} \psi_j\big|_{\xi_a} \right) \\ Q_i &= \frac{a^2}{\xi_a^3} \frac{3}{1+\alpha} \chi_k^F \psi\big|_{\xi_a} \end{aligned} \tag{2.62}$$

The beam parameter $a = \sqrt{EI/mL^4}$ describes the stiffness, inertial, and geometric properties of the beam and has dimensions of frequency. The non-dimensional parameter χ_k^F characterizes the relative stiffness of the ASM and the structure and is defined as follows,

$$\chi_k^F = \frac{k_0 (L\xi_a)^3}{3EI} \tag{2.63}$$

Note that χ_k^F is similar to the stiffness parameter $\chi_k = \dfrac{k_0}{k_{str}}$ defined in (2.34) during derivation of the zero-final-value mixing coefficient. In this case the static driving point impedance of the structure is equal to $k_{beam}^F = 3EI/(L\xi_a)^3$. For good actuator efficiency, the static stiffnesses of the ASM and the structure are matched by setting $\chi_k^F = 1$. Physically this procedure ensures that under the deformation caused by a transverse static load applied at the ASM attachment point the total strain energy is evenly divided between the beam and the equivalent stiffness of the ASM.

Sensor Outputs

The output of the ASM is derived using the general expression (2.17) and the result for ASM deformation for the case of force actuation from (2.58). After substituting the trial functions the mixed output in terms of the generalized coordinates q_i is obtained,

$$y_m^F = C_m w|_{\xi_a} + D_m q_a = S_m q + D_m q_a \tag{2.64}$$

where $S_{m_i} = C_m \gamma_i|_{\xi_a}$, while C_m and D_m depend on the mixing coefficient γ according to (2.23, 2.24).

In order to apply static correction to the result according to (2.57), the exact[1] static deformation at the actuation point caused by a unit input into the ASM must be calculated. This static deformation is then substituted into (2.64) to produce the exact static mixed output. A concentrated static force F_{asm} applied at the attachment point of the ASM results in a transverse deformation $w^e = \frac{F_{asm}(\xi_a L)^3}{3EI}$. After substituting the expression for F_{asm} from (2.10), and rearranging in non-dimensional form, the deformation can be written as,

$$w^e|_{\xi_a} = \frac{1}{1+\alpha}\frac{\chi_k^F}{1+\chi_k^F} \tag{2.65}$$

The exact deformation for the impedance matched case is calculated by substituting $\chi_k^F = 1$.

$$\bar{w}^e|_{\xi_a} = \frac{1}{2(1+\alpha)} \tag{2.66}$$

The expected exact DC component of the mixed output signal of an ASM with impedance-matched equivalent stiffness is found by substituting the result above into the mixed output equation. The exact output for a particular mixing ratio γ is used to calculate the static correction term according to (2.57) as the difference between $\bar{y}_m^e$ and the DC component

1. Exact in the context of the Bernoulli-Euler beam.

of y_m^F. It found that with the static deformation shapes included into the set of trial functions the accuracy of the solution was greatly improved and therefore the need for static correction was reduced.

Transfer Functions, Poles, Zeroes

Strain and force sensor transfer functions for representative values of sensor stiffnesses are shown in Figure 2.17. The force sensor output is adjusted by the output matching coefficient $\bar{\chi}_y$, roughly equalizing the magnitudes of the two signals.

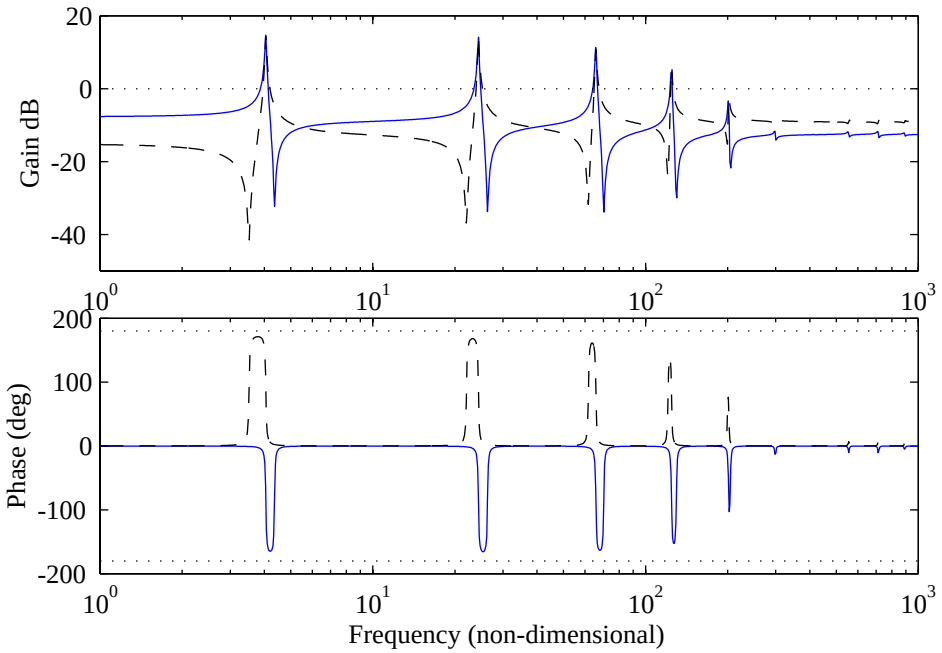

Figure 2.17 Transfer functions to strain (solid) and force (dashed) sensors derived from the assumed mode solution for a cantilever beam with an ASM as a *force* actuator; $\alpha = 0.5$, $\beta = 3.0$, $\xi_a = 0.2$.

The zero trajectory plot for the zeroes of the mixed transfer function is shown in Figure 2.18. In plotting zero trajectory plots for beams it was found convenient to change the vertical axes scaling from the usual coordinates of a zero in the complex plane (related to temporal frequency ω) to spatial frequency. The conversion from temporal to spatial frequency is done using the dispersion equation which is given in Section 2.4 and is not

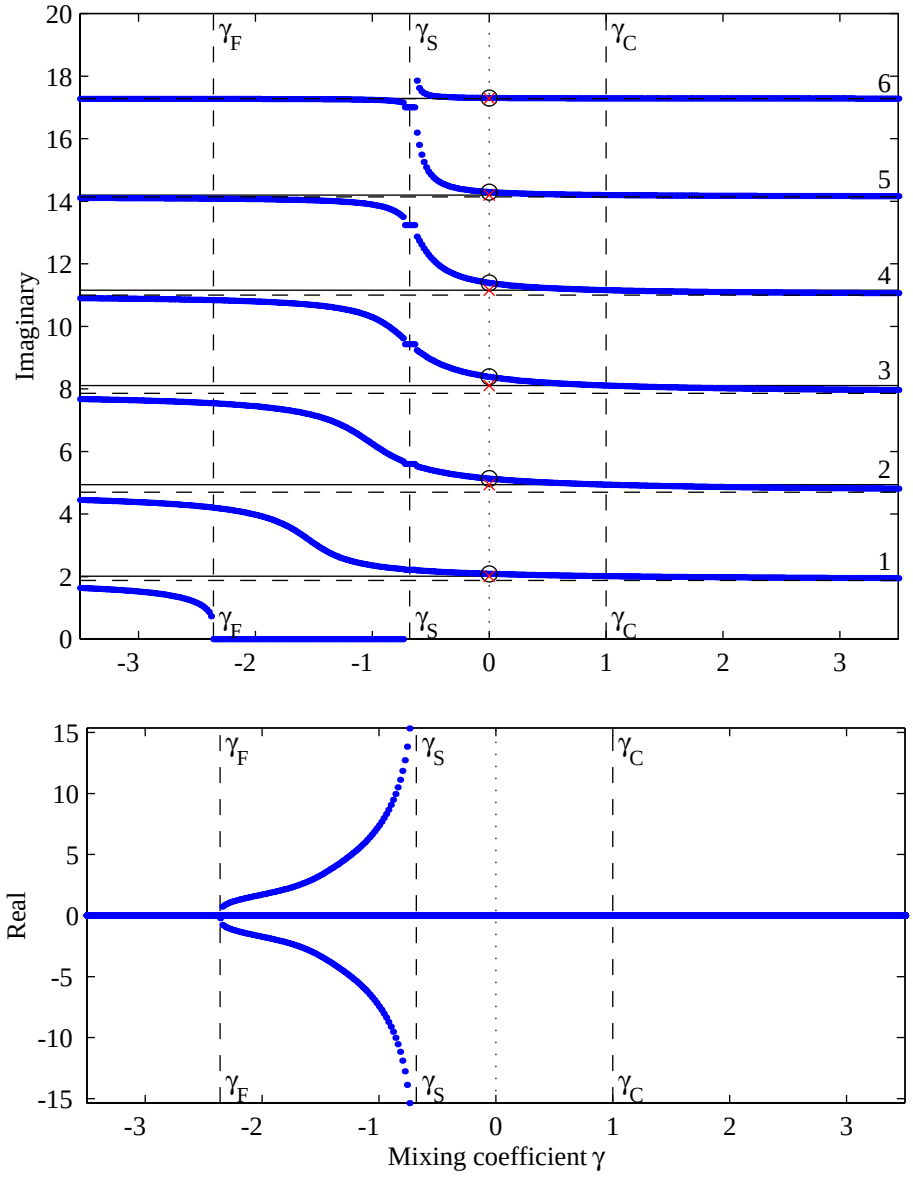

Figure 2.18 Zero trajectories as a function of the mixing coefficient γ from the assumed mode solution for a cantilever beam with an ASM acting as a *force* actuator; $\alpha = 0.7$, $\beta = 2.5$, $\xi_a = 0.2$.

important for present purposes. As the result of the change of scale the modes become evenly spaced and allow a better view of the zero trajectories. It is necessary to keep track of real-valued zeroes in order to display them properly.

In all respects the trajectories of the mixed transfer function for the beam follows the pattern set by the mass-spring system including the presence of the real-valued zeroes appearing for the negative values of the mixing coefficient between $\bar{\gamma}_F$ and $\bar{\gamma}_S$. The real-valued zeroes appear in near-symmetric pairs in the left and right hand sides of the s-plane. Just as in the case of the mass-spring system the zeroes of the mixed transfer function move monotonically between the bounds.

Without using the static deformation as an assumed mode the modeling accuracy was particularly poor for the low-frequency modes which was reflected in the first zero trajectory branch missing the intercept point at $\bar{\gamma}_F$. Using the static deformation mode completely eliminated the problem.

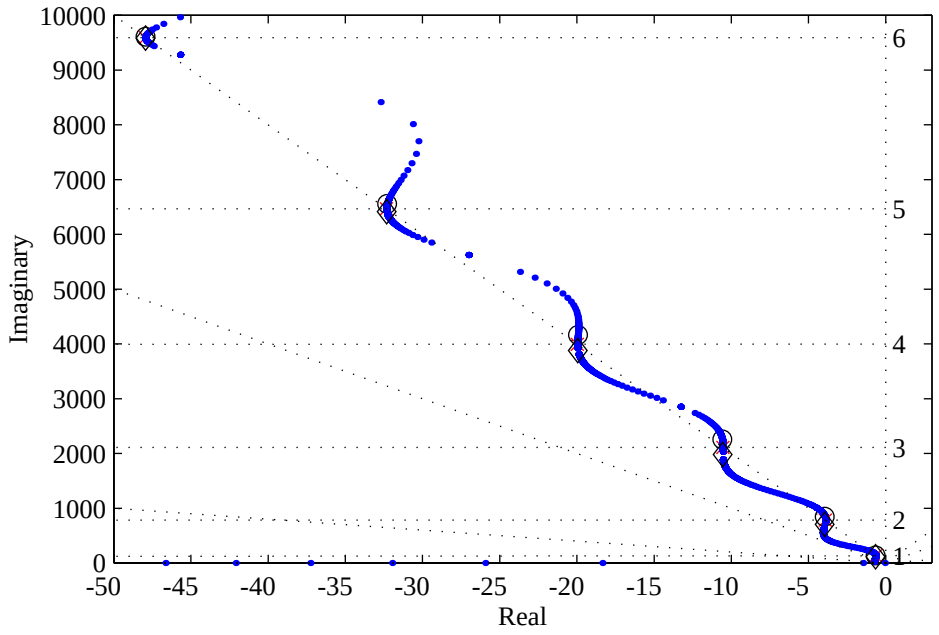

Figure 2.19 Zero locus for the first six modes of a cantilever beam with an ASM acting as a *force* actuator; $\alpha = 0.7$, $\beta = 2.5$, $\xi_a = 0.2$.

Zero locus of the mixed transfer function is shown in Figure 2.19. The behavior of the zeroes in the complex plane is very similar to that observed in the case of a lumped param-

eter system in Section 2.2. The regular pattern of the zero locus can be attributed to the constant modal damping built into the model. The zero locus was also examined for the case of randomly set modal frequencies. The result did not change significantly with the same wave pattern following the varying damping.

A different actuation configuration of the same ASM on the same beam is considered next.

2.3.3 Fixed-Free Beam with ASM as a Moment Actuator

In the previous subsection an actuator-sensor module (ASM) acting as a *force* actuator was modeled. In this subsection the same ASM is connected to the beam to act as a *moment* actuator and a *slope* sensor. This configuration is more interesting because unlike the force actuator it does not require an inertial frame to act against and is more representative of a typical beam actuation mechanism. The modeling procedure remains the same.

Model

If an ASM is placed parallel to the beam, the axial force in the actuator is converted to a bending moment acting on the beam and the ASM deformation is proportional to the relative deformation slope between the two attachment points. In general, an ASM can be placed anywhere along the beam with both ends attached to the structure (see Figure 2.15b). In that case the ASM acts as a relative actuator. Here however, for simplicity, one end of the ASM is attached to the clamp. In this case both the ASM works as an inertial actuator and sensor. The schematic of ASM placement on the beam is shown in Figure 2.20. The potential and kinetic energy expressions were given in (2.48) and (2.49) and remain unchanged. The work performed by external forces has to be rederived.

The external work is calculated according to (2.50) with the actuation moment used as the generalized force and the beam slope as the generalized displacement. The actuation moment is found as $M_{asm} = F_{asm}h$, where F_{asm} was given in (2.10) and h is the actuation moment arm, i.e. the distance from the actuator's line of action to the neutral axis of the beam. For small deformations, the axial displacement of the ASM is proportional to

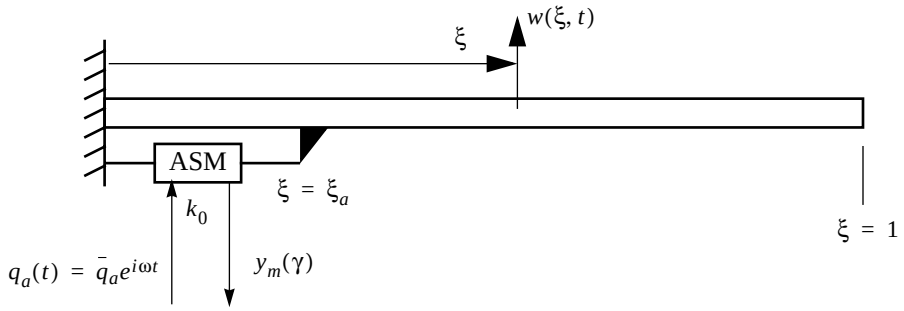

Figure 2.20 Fixed-free beam with ASM attached mid-span and acting as a moment actuator and slope sensor.

the slope of the beam at the point of attachment (see Figure 2.21). The left end of the ASM

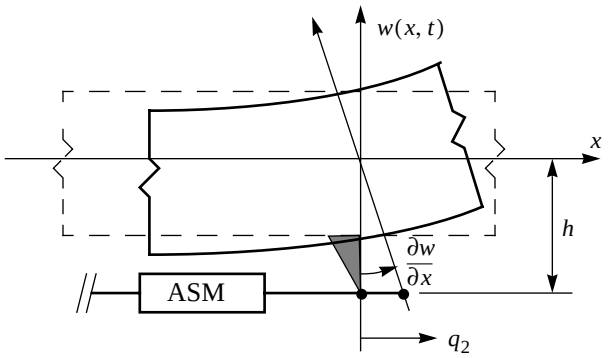

Figure 2.21 Axial displacement of the ASM mounted parallel to the beam.

is again fixed, i.e. $q_1 = 0$, and the right end moves horizontally with a point on the beam distance h away from the neutral axis, i.e. $q_2 = \left.\frac{\partial w}{\partial \xi}\right|_{\xi_a} \frac{h}{L}$. The ASM deformation for the case of moment actuation is found as,

$$q_{asm}^{M} = \left.\frac{\partial w}{\partial \xi}\right|_{\xi_a} \frac{h}{L} \tag{2.67}$$

where the superscript stands for *moment actuation.* The actuation moment is then written as follows,

$$M_{asm} = -\frac{h^2}{L^2}k_0\left.\frac{\partial w}{\partial \xi}\right|_{\xi_a} + \frac{1}{1+\alpha}hk_o q_a \tag{2.68}$$

Substituting the expression for the moment into (2.50), the work performed by the actuator is found.

$$\delta W_{ext} = M_{asm}\frac{1}{L}\delta\theta|_{\xi_a} = \left[-\frac{h}{L^3}\left.\frac{\partial w}{\partial \xi}\right|_{\xi_a} + \frac{1}{1+\alpha}q_a\right]k_o\frac{h}{L}\delta\theta|_{\xi_a} \tag{2.69}$$

Substituting trial functions and generalized coordinates in place of beam deformation, the actuator stiffness elements k_{ij} and the generalized forces Q_i^M are obtained. These expressions are analogous to the terms for the force actuator in (2.60, 2.61).

$$k^M{}_{ij} = 2\frac{h^2 k_0}{L^2}\psi_i|_{\xi_a}\psi'_j|_{\xi_a} \tag{2.70}$$

$$Q^M{}_i = \frac{h}{L}\frac{k_o}{1+\alpha}d\psi'_i|_{\xi_a} \tag{2.71}$$

The matrix element definitions required to calculate the mass, stiffness, and load matrices are given below,

$$\begin{aligned} m_{ij} &= \int_0^1 \psi_i\psi_j d\xi \\ k_{ij} &= a^2\left(\int_0^1 \psi''_i\psi''_j d\xi + \frac{2}{\xi_a}\chi_k{}^M\psi'_i|_{\xi_a}\psi'_j|_{\xi_a}\right) \\ Q_i &= \frac{a^2}{\xi_a}\frac{1}{\eta(1+\alpha)}\chi_k^M\psi_i'|_{\xi_a} \end{aligned} \tag{2.72}$$

where the nondimensional parameter $\eta = \frac{h}{L}$ is the normalized actuator moment arm, and χ_k^M is a nondimensional parameter characterizing the relative stiffness of the actuator and the structure, analogous to χ_k^F featured in the analysis of the force actuator.

$$\chi_k^M = \frac{k_0 h^2 L \xi_a}{EI} \tag{2.73}$$

The actuator stiffness is selected by matching it to the driving point bending stiffness of the beam, i.e. $\chi_k^M = 1$. Physically this procedure ensures that under the deformation caused by an axial static load applied at the ASM attachment point, the total strain energy is evenly divided between the beam and the equivalent stiffness of the ASM.

Sensor Outputs

The output of the ASM is derived using the general expression (2.17) with and the ASM deformation result from (2.67). After substituting the trial functions, the mixed output in terms of the generalized coordinates q_i is obtained,

$$y_m^M = C_m \eta \left.\frac{\partial w}{\partial \xi}\right|_{\xi_a} + D_m d = S_m q + D_m d \tag{2.74}$$

where $S_{m_i} = C_m \eta \gamma_i|_{\xi_a}$. The output terms C_m and D_m depend on the mixing coefficient according to (2.23, 2.24).

Similar to the case of force actuation, static correction is applied to the output y_m^M according to (2.57). A concentrated static force F_{asm} applied at the attachment point in the direction parallel to the beam results in a deformation slope $\frac{\partial w^e}{\partial x} = \frac{F_{asm} h \xi_a L}{EI}$. After substituting the expression for F_{asm} from (2.10) and rearranging in a nondimensional form, the exact deformation slope for the case of matched actuator impedance, i.e. $\chi_k^M = \bar{\chi}_k^M$, can be written as follows.

$$\left.\frac{\partial w^e}{\partial \xi}\right|_{\xi_a} = \frac{1}{2\eta(1+\alpha)} \tag{2.75}$$

After substitution the exact deformation slope into the mixed output equation, the expected DC component of the mixed output signal of an ASM for the system with an impedance-matched actuator is found and can be used to calculate a static correction term according to (2.57) as the difference between y_m^e and the DC component of y_m.

Transfer Functions, Poles, Zeroes

Strain and force sensor transfer functions for representative values of sensor stiffnesses are shown in Figure 2.22. The force sensor output is adjusted by the output matching coeffi-

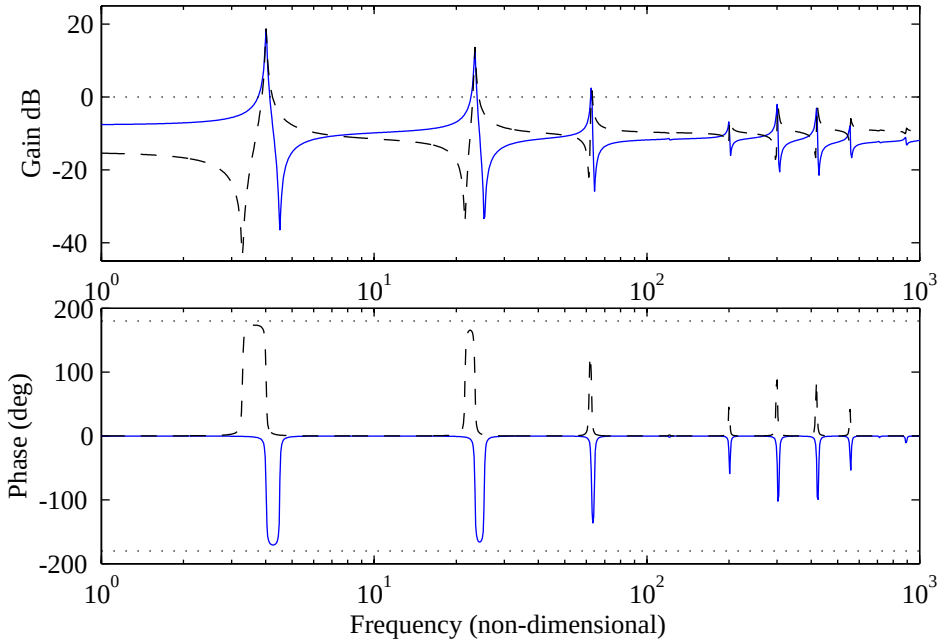

Figure 2.22 Strain (solid) and force (dash) transfer functions from the assumed-mode solution for a cantilever beam with an ASM acting as a *moment* actuator; $\alpha = 0.7$, $\beta = 2.5$, $\xi_a = 0.2$.

cient $\bar{\chi}_y$, roughly equalizing the magnitudes of the two transfer functions. Notice a nearly unobservable and uncontrollable 4th mode.

A zero trajectory plot is shown in Figure 2.23. Vertical lines mark the familiar special values of the mixing coefficient. It is useful to observe the appearance of zero trajectories around an unobservable and uncontrollable mode such as mode # 4. For all values of the mixing coefficient the position of one zero remains unchanged producing a horizontal trajectory. This zero trajectory appears to cross another one, although on close examination the two trajectories do not actually cross.

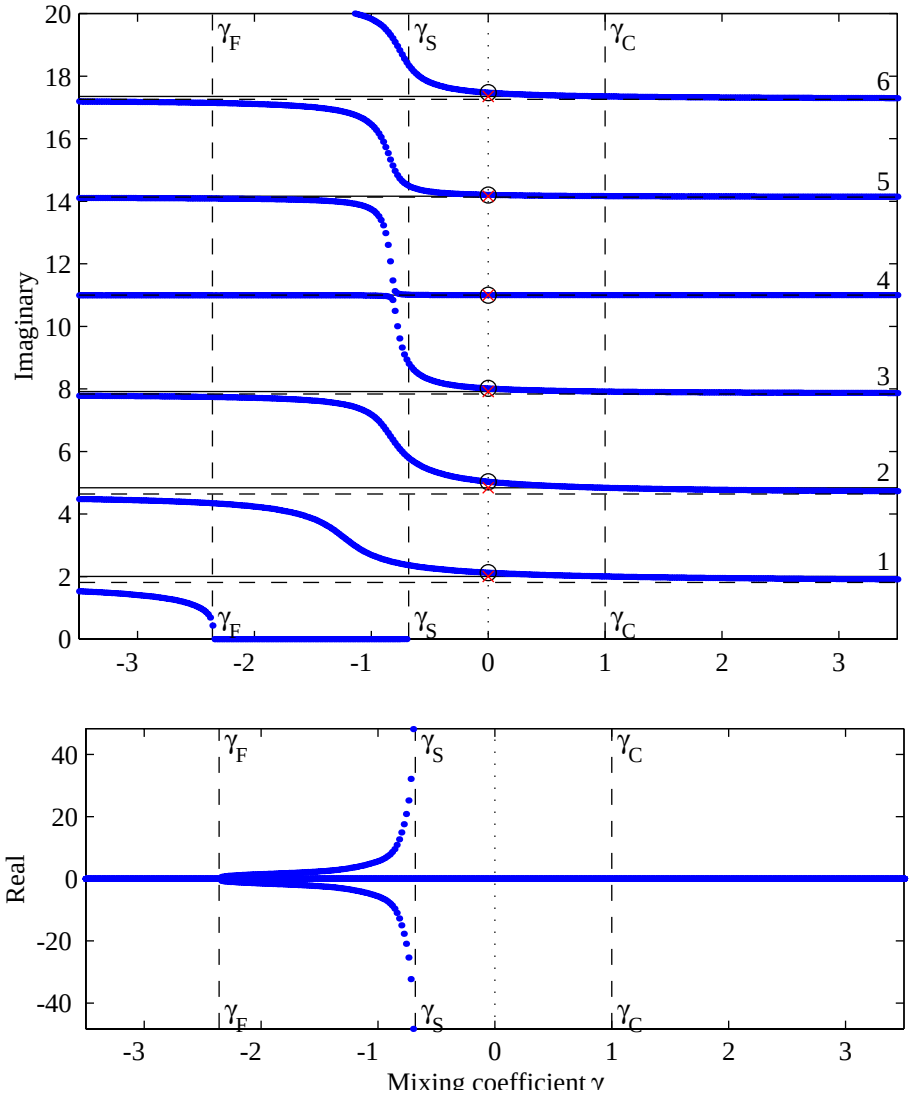

Figure 2.23 Zero trajectories from assumed-mode solution for a cantilever beam with an ASM acting as a *moment* actuator; $\alpha = 0.7$, $\beta = 2.5$, $\xi_a = 0.2$.

A zero locus plot for the case of an ASM acting as a moment actuator is shown in Figure 2.24. The zero locus in the vicinity of the unobservable and uncontrollable mode remains well-behaved, not crossing or approaching the imaginary axis.

Overall, the behavior of zeroes proved similar for the cases of the force and moment actuators.

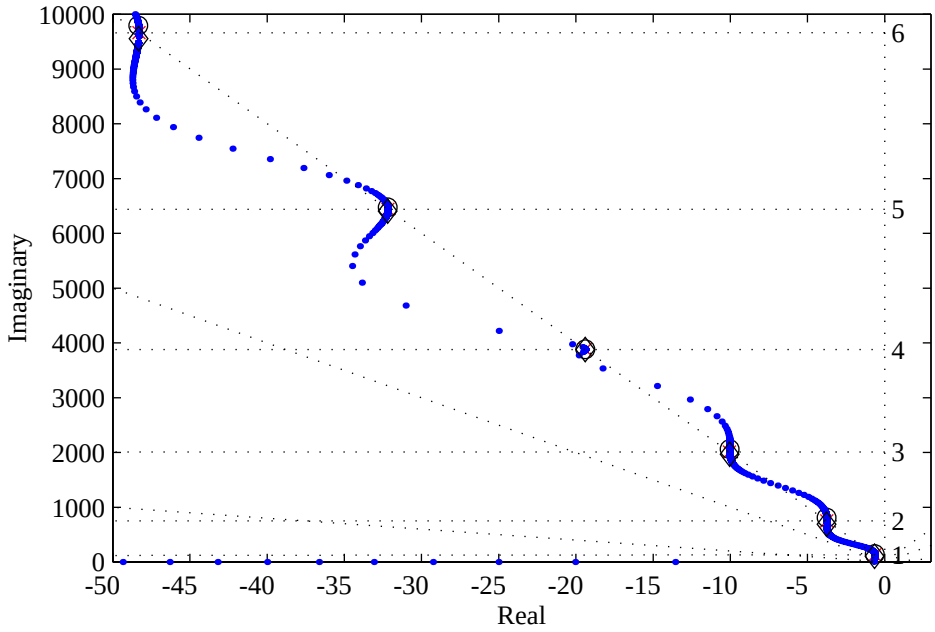

Figure 2.24 Zero locus plot for an ASM acting as a *moment* actuator attached to a cantilever beam; $\alpha = 0.7$, $\beta = 2.5$, $\xi_a = 0.2$.

Summary

It was shown in this section that according to a finite-dimensional model it appears to be possible to move the zeroes of a distributed parameter system by mixing the outputs of two sensors. A force and a moment actuation configurations were modeled. In both cases the zero trajectory plot displayed the features predicted based on the static model of the ASM and observed later in the results of modeling a 2-DOF mass-spring system. Real-valued zero were found in the region of negative mixing coefficients between γ_F and γ_S. The zero locus in the s-plane does not seem to approach or cross the imaginary axis indicating the absence of complex non-minimum phase zeroes.

2.4 Infinite-Dimensional Models of Beams

It was shown in Section 2.3 that the mixture of the outputs of the strain and force sensors retained the attractive alternating pole-zero structure except for appearance of nearly-symmetric real-valued zero pairs. In order to explore the possibility that the real-valued zeroes

are artifacts of modal truncation, this section considers exact infinite-dimensional representation of a distributed system by solving the beam equation directly. The possibility of modal truncation effects would certainly be ruled out if real-valued zeroes of the mixed transfer function are found in the exact solution of the beam equation.

A general procedure for obtaining the exact solution of a beam equation is presented first. The procedure outlines the steps for finding the poles of the system, the transfer function, and the exact zeroes of the transfer function. The following two subsections find solutions for the mixed output of an actuator-sensor module (ASM) for the cases of force and moment actuation.

2.4.1 Solution of the Beam Equation

The governing partial differential equation for a uniform Bernoulli-Euler beam is written as,

$$\frac{\partial^4 w}{\partial \xi^4} + \frac{1}{c}\frac{\partial w}{\partial t} + \frac{1}{a^2}\frac{\partial^2 w}{\partial t^2} = f(\xi, t) \tag{2.76}$$

where $w(\xi, t)$ is the transverse deflection of the beam, $\xi = \frac{x}{L}$ is the normalized coordinate along the span of the beam, and $f(\xi, t)$ is the distributed forcing function [Meirovitch, 1975; Graff, 1975]. The mass, stiffness, and damping characteristics of the beam are summarized in two parameters $a^2 = \frac{EI}{mL^4}$ and $c = \frac{EI}{c^* L^4}$, where L is the length of the beam, EI is constant flexural stiffness, m is constant mass per unit length, and c^* is the equivalent viscous damping per unit length.

Note that the actual amount of damping attributed to the beam is not important for the purposes of this study and small damping was included to improve readability of the frequency response plots. For the systems considered in this chapter, the forcing term f is absent and excitation enters in the equations through boundary conditions.

Solution

To find the dispersion relation which relates the spatial and temporal frequencies [Graff, 1975], a homogeneous solution of (2.76) in the form $w(\xi, t) = Ae^{i(k\xi - \omega t)}$ is assumed. Substituting and solving for the wave number k results in:

$$k^4 = \frac{\omega^2}{a^2} + i\frac{\omega}{c} \tag{2.77}$$

The homogeneous undamped case of (2.76) is solved next by assuming a solution with separated variables as follows,

$$w(\xi, t) = X(\xi)e^{i\omega t}. \tag{2.78}$$

Substituting the assumed solution into (2.76), results in,

$$\left[X^{IV} - \frac{\omega^2}{a^2}X\right]e^{i\omega t} = 0 \tag{2.79}$$

The spatial component of the solution is sought in the form of $X(\xi) = e^{r\xi}$, with $r = \pm k,\ \pm ik$, subject to four boundary conditions – two at each end of the beam.

$$X(\xi) = Ae^{ik\xi} + Be^{-ik\xi} + Ce^{k\xi} + De^{-k\xi} \tag{2.80}$$

Taking the appropriate derivatives of the assumed solution in (2.80), substituting into the boundary conditions, and assuming harmonic excitation in the forcing boundary conditions, a linear system (2.81) is obtained.

$$A_{BC}v_{BC} = F_{BC} \tag{2.81}$$

where A_{BC} is the boundary condition matrix, $v_{BC} = \begin{bmatrix} A & B & C & D \end{bmatrix}^T$ is a vector of constant coefficients in the assumed solution and F_{BC} is the forcing term defined by the boundary conditions. Equation (2.81) can be used to solve for the frequency response and the poles of the transfer function.

To find the structural frequency response directly, the linear system in (2.81) is solved for the coefficient vector v_{BC}. The spatial part of the solution $X(\xi)$ is then found according to (2.80). The spatial part of the solution $X(\xi)$ is a complex-valued function of the position along the beam and the wave number k and when divided by the amplitude of the harmonic input produces the transfer function from the harmonic excitation at the boundaries to the structural response at any point along the beam. The wave number k is related to the temporal frequency ω through the dispersion relation (2.77).

In order to find the poles of the system, the homogeneous form of (2.81) is considered. The non-trivial solution of the homogeneous linear system requires the boundary condition matrix A_{BC} to be singular, which means that the determinant of the matrix must be zero. For simple systems considered in this section, it is always possible to obtain a closed-form expression for the determinant and numerically solve for the roots of the resulting transcendental equation, usually called the *frequency equation*.

$$det(A_{BC}) = 0 \tag{2.82}$$

Two approaches can be taken for finding the zeroes of the analytical transfer function. One possible approach is to obtain a numerical solution for the frequencies at which the output of the system expressed in terms of $X(\xi)$ is zero for a nonzero input. This method however fails to identify the zeroes which are perfectly cancelled by the system poles and is likely to give poor results for near pole-zero cancellation.

An alternative approach makes use of the root locus definition of the zeroes of a transfer function [Fleming, 1990]. The finite zeroes of the open loop transfer function are equal to the poles of the closed loop system with feedback gain set to infinity. A feedback loop is formed around the transfer function whose zeroes are being sought. The resulting *closed-loop* boundary condition matrix depends on the feedback gain. The determinant of this matrix is found and the limit of the determinant with the feedback gain approaching infinity is calculated. The solution of the resulting transcendental equation gives the frequencies of the zeroes of the open loop transfer function.

$$\lim_{g \to \infty} det(A_{BC}^{CL}) = 0 \tag{2.83}$$

In summary, the following results are obtained by solving the beam equation: (i) the exact transfer function from the ASM control input to the ASM mixed output as a function of the mixing coefficient γ, ASM position along the beam ξ_a, the internal ASM stiffnesses α, β, and the relative stiffness χ_k; (ii) the exact transcendental frequency equation (2.82) whose numerically found roots are the poles of the mixed transfer function; (iii) the exact transcendental closed loop frequency equation (2.83) whose numerically found roots are the zeroes of the mixed transfer function.

The solution procedure outlined in this subsections will now be applied to a cantilever beam with an ASM attached to it. Two actuation configurations already encountered in Section 2.3 will be considered.

2.4.2 Fixed-Free Beam with an ASM as a Force Actuator

This subsection applies the general wave solution method outlined in the preceding subsection to the case of an ASM attached perpendicular to a cantilever beam and functioning as a force actuator and a displacement sensor. An approximate solution for this system was already found in Section 2.3.2.

Solution

The system to consider a uniform beam with fixed-free boundary conditions and an ASM attached at an arbitrary point along the span of the beam (see Figure 2.25a). The beam can be broken up into two segments with two assumed solutions $w_1(\xi, t)$ and $w_2(\xi, t)$ for the transverse deformation of the beam. After variable separation, the temporal component in both solutions is the $e^{i\omega t}$ and the spatial components are $X_1(\xi)$ and $X_2(\xi)$.

$$\begin{aligned} X_1(\xi) &= A_1 e^{ik\xi} + B_1 e^{-ik\xi} + C_1 e^{k\xi} + D_1 e^{-k\xi} \\ X_2(\xi) &= A_2 e^{ik\xi} + B_2 e^{-ik\xi} + C_2 e^{k\xi} + D_2 e^{-k\xi} \end{aligned} \tag{2.84}$$

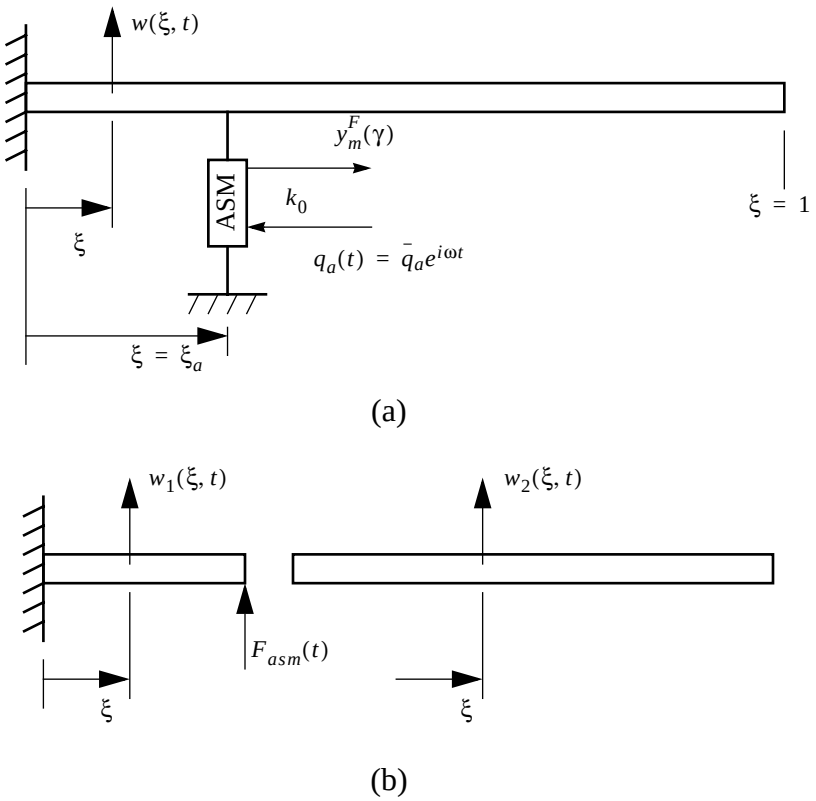

Figure 2.25 (a) Fixed-free beam with ASM as a force actuator; (b) the full solution is obtained by dividing the beam into two parts with compatibility boundary conditions at the common point.

The boundary conditions at the fixed end represent zero deflection and zero slope at the clamp.

$$\begin{aligned} w_1\big|_{\xi = 0} &= 0 \\ w_1'\big|_{\xi = 0} &= 0 \end{aligned} \tag{2.85}$$

The boundary conditions at the free end specify zero moment and zero force at the tip.

$$\begin{aligned} w_2''\big|_{\xi = 1} &= 0 \\ w_2'''\big|_{\xi = 1} &= 0 \end{aligned} \tag{2.86}$$

The continuity boundary conditions enforce continuity of deflection, slope, curvature, and shear force across the common point between the two segments of the beam. The last continuity boundary condition accounts for the force exerted by the ASM onto the beam.

$$\begin{aligned} w_1|_{\xi_a} &= w_2|_{\xi_a} \\ w_1'|_{\xi_a} &= w_2'|_{\xi_a} \\ w_1''|_{\xi_a} &= w_2''|_{\xi_a} \\ w_1'''|_{\xi_a} &= -\frac{L^3}{EI}F(t) + w_2'''\Big|_{\xi_a} \end{aligned} \tag{2.87}$$

The sign of the force in the last boundary condition is consistent with common sign convention, i.e. positive sign for an external force applying a clockwise moment to the beam. Substituting $F(t) = F_{asm} = -k_0 w_1|_{\xi_a} + \frac{k_0}{(1+\alpha)} q_a$ from (2.10) into the shear force continuity boundary condition, a new form of the last boundary condition reads,

$$w_1'''|_{\xi_a} + \frac{3}{\xi_a^3}\chi_k^F w_1|_{\xi_a} - w_2'''|_{\xi_a} = \frac{3}{(1+\alpha)\xi_a^3}\chi_k^F q_a \tag{2.88}$$

where the non-dimensional stiffness parameter χ_k^F characterizes the relative stiffnesses of the ASM and the beam, and was previously defined by (2.63) in the derivation of the approximate solution. Following the reasoning of Section 2.3.2, the actuator stiffness is set to match the static driving-point bending stiffness of the beam.

Substituting $w(\xi, t) = X(\xi)e^{i\omega t}$ from (2.78) and its derivatives, and considering harmonic excitation $q_a = \bar{q}_a e^{i\omega t}$, the boundary conditions yield a system of linear equations with a vector of 8 unknown coefficients v_{BC}.

$$\begin{bmatrix} 1 & 1 & 1 & 1 & 0 & 0 & 0 & 0 \\ i & -i & 1 & -1 & 0 & 0 & 0 & 0 \\ t_3 & t_4 & t_1 & t_2 & -t_3 & -t_4 & -t_1 & -t_2 \\ it_3 & -it_4 & t_1 & -t_2 & -it_3 & it_4 & -t_1 & t_2 \\ -t_3 & -t_4 & t_1 & t_2 & t_3 & t_4 & -t_1 & -t_2 \\ -(i+t_9)t_3 & (i-t_9)t_4 & (1-t_9)t_1 & -(1+t_9)t_2 & it_3 & -it_4 & -t_1 & t_2 \\ 0 & 0 & 0 & 0 & -t_7 & -t_8 & t_5 & t_6 \\ 0 & 0 & 0 & 0 & -it_7 & it_8 & t_5 & -t_6 \end{bmatrix} \begin{bmatrix} A_1 \\ B_1 \\ C_1 \\ D_1 \\ A_2 \\ B_2 \\ C_2 \\ D_2 \end{bmatrix} = \begin{bmatrix} 0 \\ 0 \\ 0 \\ 0 \\ 0 \\ -\dfrac{3\bar{q}_a}{(1+\alpha)(\xi_a k)^3} \\ 0 \\ 0 \end{bmatrix} \tag{2.89}$$

The following temporary variables are used in the boundary condition matrix above $t_1 = e^{k\xi_a}$, $t_2 = e^{-k\xi_a}$, $t_3 = e^{ik\xi_a}$, $t_4 = e^{-ik\xi_a}$, $t_5 = e^{k}$, $t_6 = e^{-k}$, $t_7 = e^{ik}$, $t_8 = e^{-ik}$, $t_9 = \dfrac{3}{(\xi_a k)^3}$.

Solving for the coefficients v_{BC} and substituting into (2.84) gives the exact structural response of the beam $X_{1,2} = X_{1,2}(k, \xi, \xi_a)\bar{q}_a$ at an arbitrary point ξ driven with the excitation frequency ω by an actuator located at ξ_a.

A general expression for the mixture of force and strain outputs of an ASM was derived earlier (ref.). Substituting $q_1 = 0$ and $q_2 = w_1\big|_{\xi = \xi_a}$, an expression for the mixed output of an ASM attached perpendicular to a cantilever beam is found.

$$y_m = C_m(\gamma) w_1\big|_{\xi_a} + D_m(\gamma) q_a \tag{2.90}$$

Transfer Function, Poles, Zeroes

Setting the amplitude of the input $\bar{q}_a$ to unity for simplicity, the transfer function from ASM input to its mixed output is found as,

$$G_{yd}(k, \gamma) = C_m(\gamma) X_1\big|_{\xi_a} + D_m(\gamma) \tag{2.91}$$

The poles of the single-input single-output (SISO) transfer function G_{yd} are found according to (2.82) by setting the right-hand side of (2.89) equal to zero and looking for singularities of the boundary condition matrix A_{BC}. A closed-form expression for the determinant of the 8 by 8 boundary condition matrix was found using Maple[1] symbolic mathematics package and then the roots of the frequency equation were found numerically in Matlab[2].

The zeroes of $G_{yd}(s)$ are calculated by closing a feedback loop around the ASM transfer function and finding the roots of the closed-loop frequency equation. A constant-gain control law is defined as $q_a = -gy_m(\gamma)$. Substituting it into (2.90) and solving for the control signal q_a, the control signal is found as,

$$q_a = -\frac{gC_m}{1+gD_m} w_1\big|_{\xi_a} \tag{2.92}$$

The loop is closed by feeding the control signal q_a into the ASM actuator which produces an external force according to (2.10),

$$F(t) = -k_0\left[1 + \frac{1}{1+\alpha}\frac{gC_m}{1+gD_m}\right] w_1\big|_{\xi_a} \tag{2.93}$$

Substitution of the feedback force into the boundary conditions leads to the closed-loop shear force continuity boundary condition.

$$w_1'''\big|_{\xi_a} + \frac{3}{\xi_a^3}\left[1 + \frac{1}{1+\alpha}\frac{gC_m}{1+gD_m}\right] w_1\big|_{\xi_a} - w_2'''\big|_{\xi_a} = 0 \tag{2.94}$$

The rest of the boundary conditions are not affected by feedback.

The closed-loop boundary condition matrix depends on the feedback gain g. After multiplying by $(1+gD_m)$, the determinant of the closed loop boundary condition matrix A_{BC}^{CL} is a first order polynomial in g and can be expressed as $det(A_{BC}^{CL}) = f_1 + g f_2$. The limit of the determinant when $g \to \infty$ is taken and the resulting transcendental equation can be expressed as a first order polynomial in the mixing coefficient γ.

$$\lim_{g\to\infty} \frac{1}{g}(f_1 + g f_2) = f_2 = C_m(\gamma) f_{21} + D_m(\gamma) f_{22} = h_1 + \gamma h_2 = 0 \tag{2.95}$$

1. Maple V Release 4, Waterloo Maple Inc., W. Waterloo, Ontario, Canada.
2. Matlab 5, The MathWorks, Inc., Natick, MA, US.

where $h_1 = f_{21} + f_{22}/\beta$ and $h_2 = -f_{21} + f_{22}/(1+\alpha)$. The expressions for f_{21} and f_{22} contain a large number of exponential terms. They were found using Maple symbolic mathematics package. The roots of the frequency equation (2.95) are the poles of the infinite-gain closed-loop system and the zeroes of the original open-loop transfer function. The roots of the frequency equation were found numerically using Matlab software package.

To verify that the transfer function solution is consistent with the solution for the poles and the zeroes, the results for a sample ASM/beam configuration are plotted in Figure 2.26.

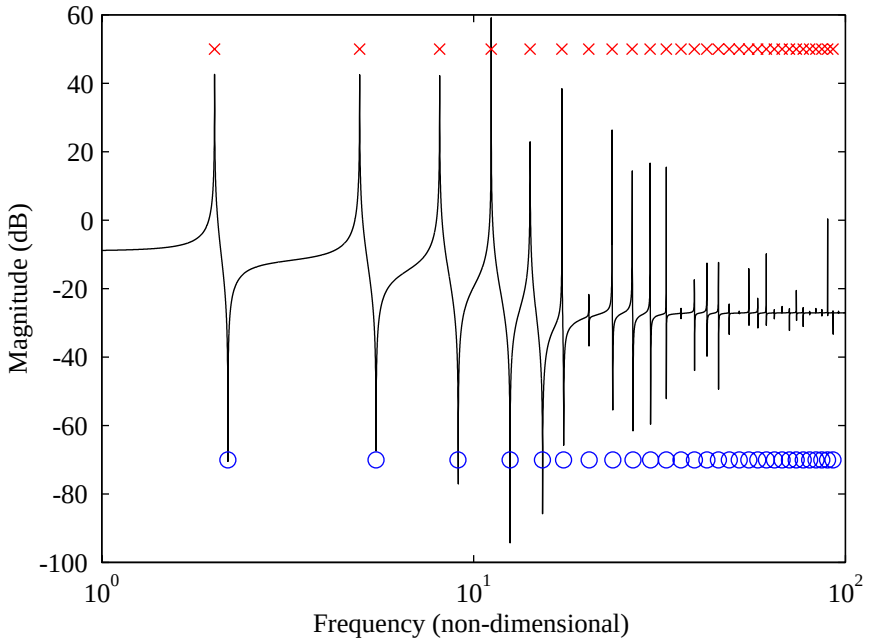

Figure 2.26 Typical mixed transfer function using wave analysis for a cantilever beam with an ASM acting as a *force* actuator, with independently calculated poles (crosses) and zeroes (circles); $\alpha = 0.5$, $\beta = 3.0$, $\gamma = -0.4$, $\xi_a = 0.2$.

The transfer function does not include any damping and its finite magnitude at resonances is due discretization in plotting. Individual strain and force sensor transfer functions are shown in Figure 2.27.

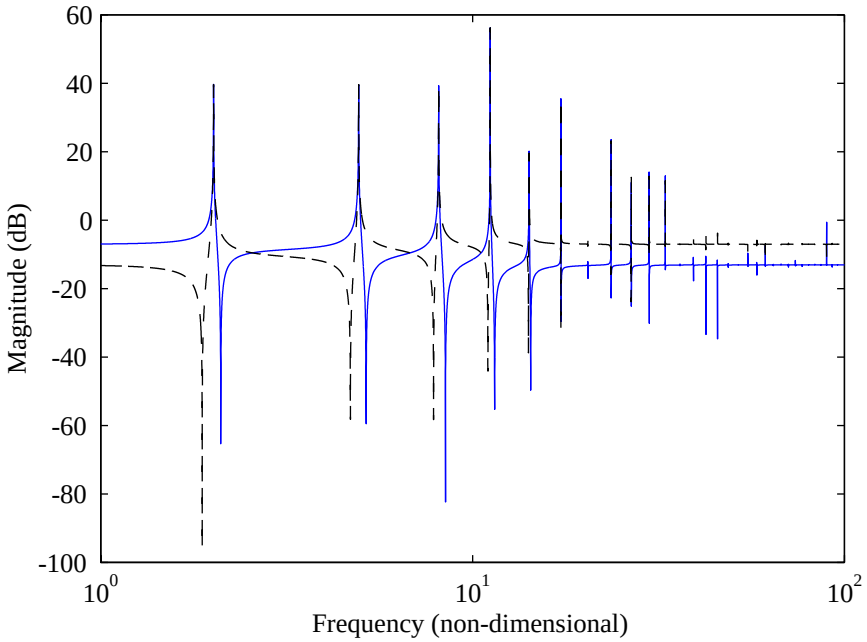

Figure 2.27 Strain (solid) and force (dashed) sensor transfer function from wave solution for the ASM acting as a *force* actuator attached to a cantilever beam.

The effect of the mixing coefficient γ on the zeroes of the transfer function is investigated next. The closed-loop frequency equation (2.95) is numerically solved for a range of mixing coefficients and the resulting wave numbers for the zeroes of the transfer function are plotted in the familiar format of zero trajectories in Figure 2.28. The general pattern of the trajectories mimics the one observed for the lumped parameter system and for the approximate solution of a cantilever beam.

The bottom branch intercepts the zero frequency line exactly at the mixing gain value of γ_F. However the real-valued zeroes were not encountered. Zero trajectories for higher modes become increasingly sensitive to the mixing coefficient. High-mode trajectories quickly shift from one zero of the force transfer function to the one above. The shift occurs at γ_S. Pole-zero cancellation occurs at the mixing gain value of γ_C.

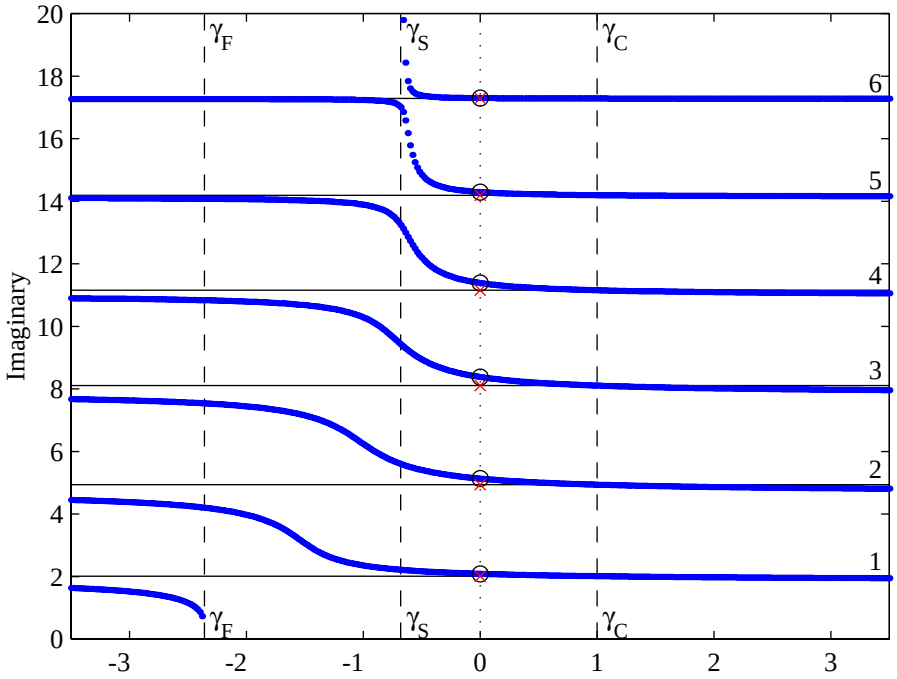

Figure 2.28 Zero trajectories as a function of the mixing coefficient γ for the wave model of a cantilever beam with an ASM acting as *force* actuator, $\alpha = 0.7$, $\beta = 2.7$, $\xi_a = 0.2$.

2.4.3 Fixed-Free Beam with an ASM as a Moment Actuator

In this subsection the solution procedure from Section 2.4.1 is applied to the case of an actuator-sensor module (ASM) acting as a moment actuator. The ASM is oriented parallel to a cantilever beam, as shown in Figure 2.29a. Note that the setup is identical to the one considered in Section 2.3.3 where an approximate solution of the same problem was found using the assumed mode method.

Solution

The solution method follows the steps taken in finding the solution for the force actuator. A different actuation method, however, leads to different boundary conditions. The displacement solution is divided into two parts and is sought in the same form as for the force actuator given in (2.84).

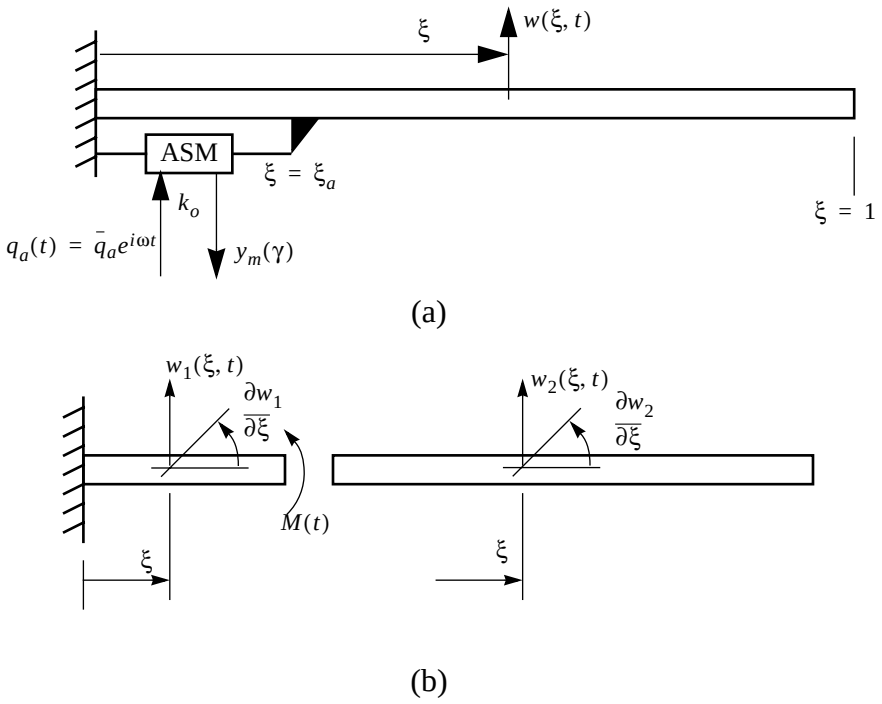

Figure 2.29 (a) Fixed-free beam with ASM as a moment actuator; (b) the full solution is obtained by dividing the beam into two parts with compatibility boundary conditions at the common point.

The root and tip boundary conditions (2.85, 2.86) also remain unchanged. The displacement and slope continuity boundary conditions in (2.87) are the same. The curvature and shear continuity boundary conditions, however, are different and are re-derived below.

$$\begin{aligned} w_1''\big|_{\xi_a} &= \frac{L^2}{EI}M(t) + w_2''\big|_{\xi_a} \\ w_1'''\big|_{\xi_a} &= w_2'''\big|_{\xi_a} \end{aligned} \tag{2.96}$$

The sign of $M(t)$ accounts for the direction of the applied moment in Figure 2.29b. Substituting $M(t) = F_{asm}h = -\frac{h}{L}k_0 w_1'\big|_{\xi_a} + \frac{h}{1+\alpha}k_0 q_a$ into (2.96) and rearranging, the curvature boundary condition reads,

$$w_1''\big|_{\xi_a} + \frac{1}{\xi_a}\chi_k^M w_1'\big|_{\xi_a} - w_2''\big|_{\xi_a} = \frac{1}{\eta(1+\alpha)\xi_a}\chi_k^M q_a \tag{2.97}$$

where χ_k^M is a non-dimensional stiffness parameter identical to the one which appearing in the derivation of an approximate solution and given in (2.73). The actuator stiffness is again matched to the driving-point static bending stiffness of the beam.

Substituting $w(\xi, t) = X(\xi)e^{i\omega t}$ from (2.78) and its derivatives into the boundary conditions and considering harmonic excitation $q_a = \bar{q}_a e^{i\omega t}$, the boundary value problem leads to a linear system with the coefficients of the assumed solution (2.84) forming a vector of 8 unknowns.

$$\begin{bmatrix} 1 & 1 & 1 & 1 & 0 & 0 & 0 & 0 \\ i & -i & 1 & -1 & 0 & 0 & 0 & 0 \\ t_3 & t_4 & t_1 & t_2 & -t_3 & -t_4 & -t_1 & -t_2 \\ it_3 & -it_4 & t_1 & -t_2 & -it_3 & it_4 & -t_1 & t_2 \\ (-1+it_9)t_3 & -(1+it_9)t_4 & (1+t_9)t_1 & (1-t_9)t_2 & t_3 & t_4 & -t_1 & -t_2 \\ -it_3 & it_4 & t_1 & -t_2 & it_3 & -it_4 & -t_1 & t_2 \\ 0 & 0 & 0 & 0 & -t_7 & -t_8 & t_5 & t_6 \\ 0 & 0 & 0 & 0 & -it_7 & it_8 & t_5 & -t_6 \end{bmatrix} \begin{bmatrix} A_1 \\ B_1 \\ C_1 \\ D_1 \\ A_2 \\ B_2 \\ C_2 \\ D_2 \end{bmatrix} = \begin{bmatrix} 0 \\ 0 \\ 0 \\ 0 \\ \bar{q}_a \\ \hline \eta(1+\alpha)\xi_a k^2 \\ 0 \\ 0 \\ 0 \end{bmatrix} \tag{2.98}$$

The following temporary variables are used in the boundary condition matrix above $t_1 = e^{k\xi_a}$, $t_2 = e^{-k\xi_a}$, $t_3 = e^{ik\xi_a}$, $t_4 = e^{-ik\xi_a}$, $t_5 = e^{k}$, $t_6 = e^{-k}$, $t_7 = e^{ik}$, $t_8 = e^{-ik}$, $t_9 = \dfrac{1}{\xi_a k}$.

Substituting $q_1 = 0$ and $q_2 = \eta \dfrac{\partial w}{\partial \xi}\Big|_{\xi_a}$ into the general expression for the mixed force-strain output of an ASM obtain,

$$y_m = C_m \eta w_1'|_{\xi_a} + D_m d \tag{2.99}$$

where C_m and D_m are given in (2.23, 2.24).

Transfer Function, Poles, Zeroes

Following the steps already familiar from the analysis of the force actuator in the preceding subsection, the transfer function from ASM input to its mixed output is found as,

$$G_{yd}(k, \gamma) = C_m(\gamma)\eta X_1|_{\xi_a} + D_m(\gamma) \tag{2.100}$$

The poles the ASM/structure system are found by numerically solving for the roots of the frequency equation, obtained by setting the determinant of the boundary condition matrix A_{BC} in (2.98) to zero.

The zeroes of the transfer function were found in a manner similar to the previous subsection, by closing a feedback loop around the ASM output and setting the feedback gain to infinity. The control law is again $q_a = -gy_m(\gamma)$. Substituting (2.99) and solving for the control signal q_a, obtain,

$$q_a = -\frac{gC_m}{1+gD_m}\eta w_1'\big|_{\xi_a} \tag{2.101}$$

Substituting the result into the moment exerted by the ASM onto the beam $M_{asm} = F_{asm}h$,

$$M(t) = -\frac{h^2}{L}k_0\left[1+\frac{1}{1+\alpha}\frac{gC_m}{1+gD_m}\right]w_1'\big|_{\xi_a} \tag{2.102}$$

The curvature continuity boundary condition is the only one affected by the feedback and it is modified as,

$$w_1''\big|_{\xi_a} + \frac{1}{\xi_a}\left[1+\frac{1}{1+\alpha}\frac{gC_m}{1+gD_m}\right]w_1'\big|_{\xi_a} - w_2''\big|_{\xi_a} = 0 \tag{2.103}$$

The closed-loop frequency equation is found by forming the closed-loop boundary condition matrix, calculating its determinant, and finding its limit as the feedback gain approaches infinity. The form of the closed-loop frequency equation is the same as for the system with a force actuator (2.95), with the exception that f_{21} and f_{22} are modified for the moment actuator problem. The roots of the closed-loop frequency equation are the zeroes of the open-loop ASM transfer function.

Strain and force sensor transfer functions for typical values of ASM component stiffnesses is shown in Figure 2.30. The magnitude of the force sensor transfer function is adjusted to match the output of the strain sensor.

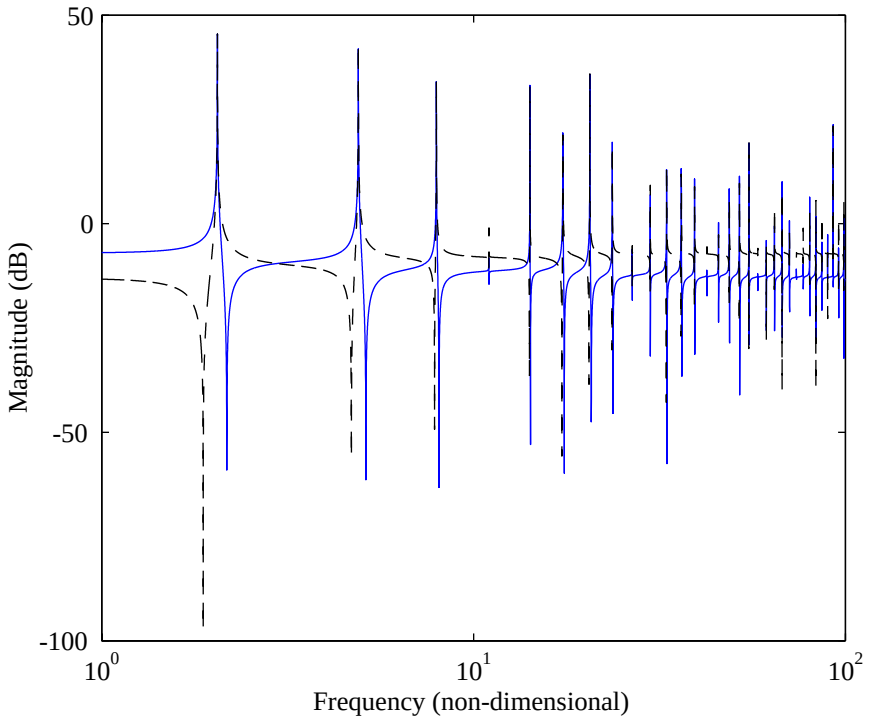

Figure 2.30 Strain (solid) and force (dash) sensor transfer functions from the wave solution for the ASM acting as a *moment* actuator attached to a cantilever beam; $\alpha = 0.5$, $\beta = 3.0$, $\xi_a = 0.2$.

The zero trajectory plot is shown in Figure 2.31. It demonstrates features already encountered in previous sections. Notice the characteristic signs of a nearly unobservable/uncontrollable mode # 4.

Summary

In this section the exact transfer functions from the ASM input to the mixed output were calculated for the cases of force and moment actuation. A numeric solution for the exact poles and zeroes of the transfer function was also found. Qualitatively, the exact zero tra-

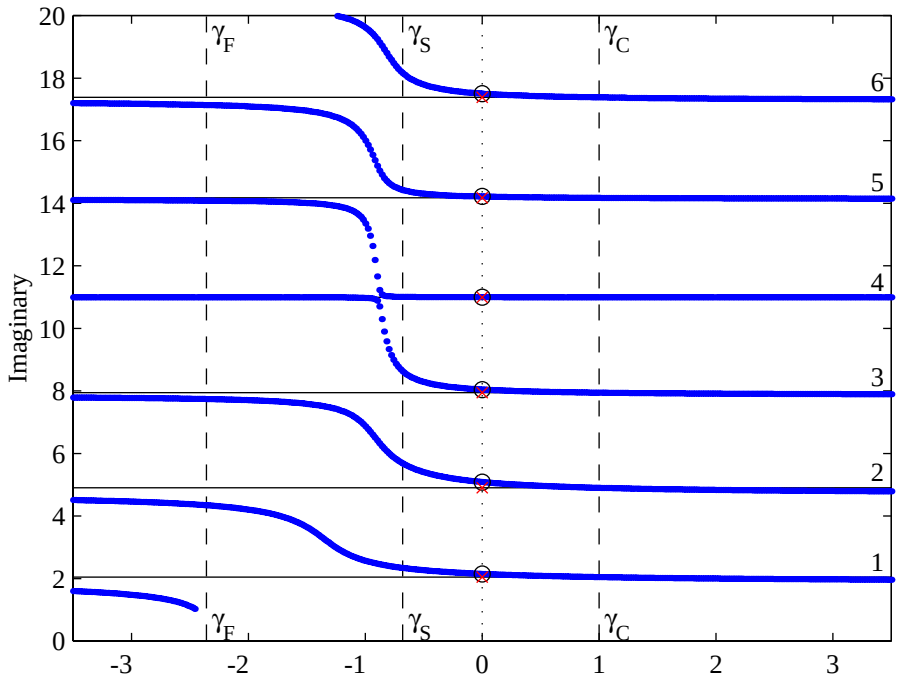

Figure 2.31 Zero trajectories as a function of the mixing coefficient γ from the wave solution of a cantilever beam with an ASM acting as a *moment* actuator; $\alpha = 0.7$, $\beta = 2.7$, $\xi_a = 0.2$.

jectories exhibit the same behavior as the approximate ones with the notable exception of the real-valued zero branch which was not captured by the solution.

2.5 Discussion of Results

Having modeled the effect of output mixing for the cases of actuator-sensor module connected to several systems, some preliminary conclusions can be made. This section focuses on the similarities and the differences between the zero trajectories observed in the models of lumped- and distributed-parameter systems. It also compares the results obtained from the exact and approximate models of a cantilever beam, specifically the presence of real-valued zeroes. For the beam models, a comparison is also made between two different actuation configurations. The section also raises a specific question on the

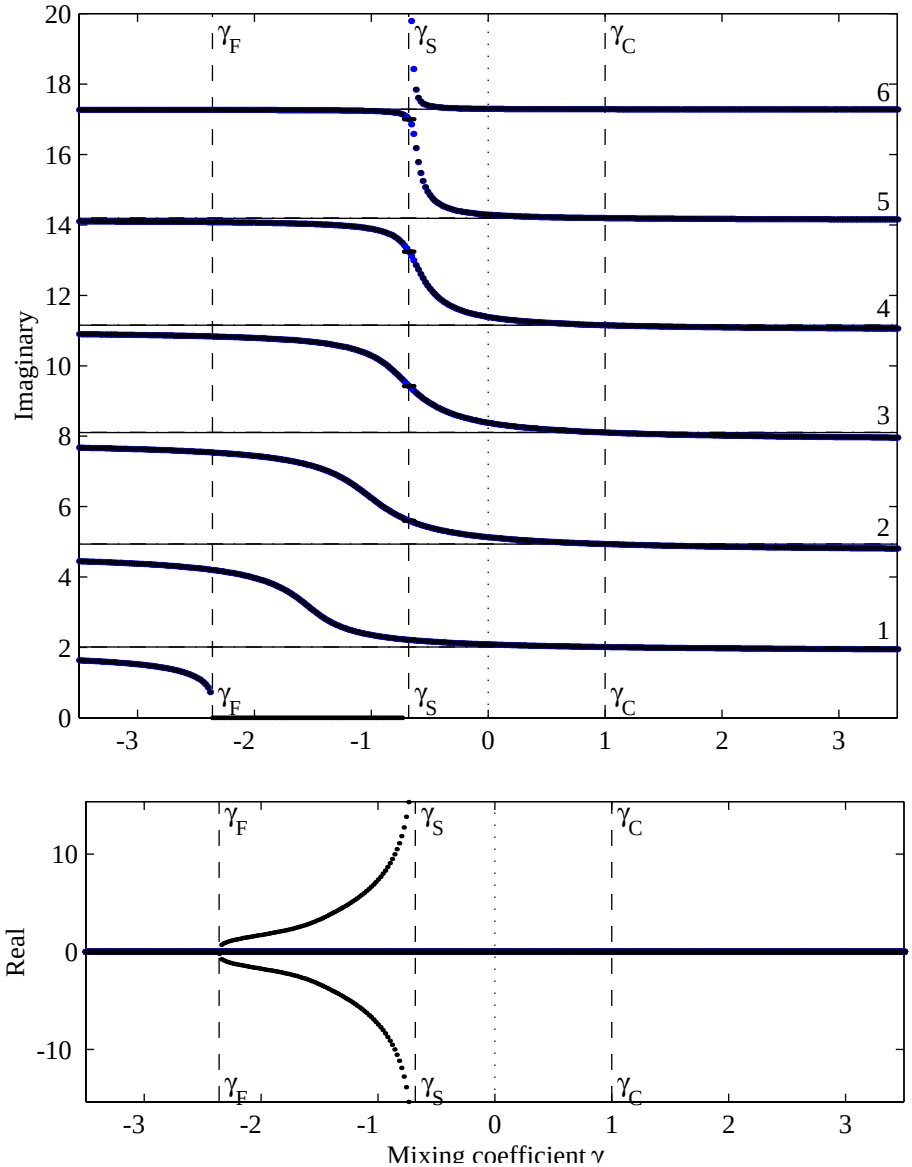

Figure 2.32 Comparison of zero trajectories using exact (large dots) and approximate (small dots) models for the *force* actuator, the two solutions overlap with the obvious exception of the real zeroes only present in the approximate solution.

nature of the real-valued zeroes which appear in the approximate model but not in the model based on the wave solution

Qualitatively, the zero trajectories of the lumped-parameter system discussed in Section 2.2 and the finite-dimensional models of beams in Section 2.3 appear very similar.

The features of the zero trajectory plot summarized in Section 2.1.3 were confirmed on models of lumped and distributed systems. It was also observed that both system types produced monotonically varying zero trajectories, thus verifying the assumption made in Section 2.1.3.

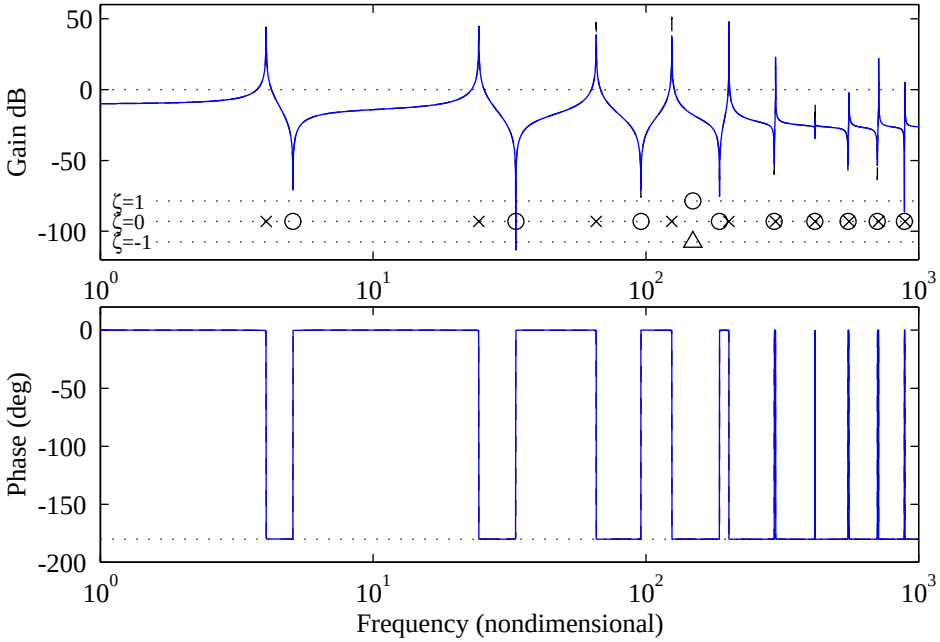

Figure 2.33 Comparison of exact (solid) and approximate (dashed) sample transfer function, $\gamma = -0.6$; poles and zeroes of the approximate transfer function are shown containing a real-valued zero pair, one real MP (circle) and one real NMP (triangle); the two transfer functions nearly overlap.

The finite-dimensional models of both the mass-spring system and the beam gave rise to similar patterns of nearly-symmetric real-valued zeroes one of which is minimum phase (MP) and the other non-minimum phase (NMP). The real zeroes occur only in the region of negative values of the mixing coefficient between γ_F and γ_S. Their frequency diminishes as the values of the mixing coefficient increase in magnitude. The physical significance of the NMP zeroes was explained in Section 2.1.3.

A key goal of this chapter was to compare the zero patterns of the same beam structure using approximate and exact solution methods. The objective of the investigation was to

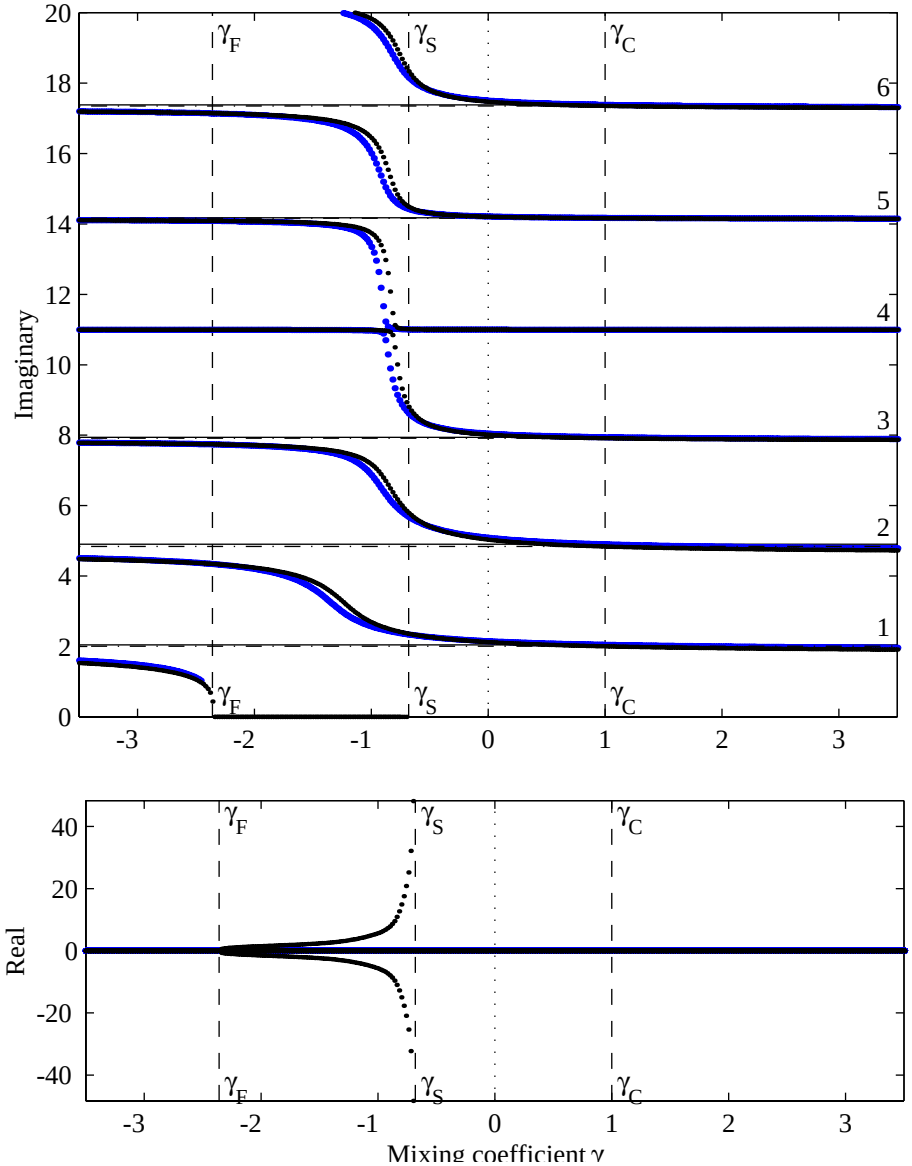

Figure 2.34 Comparison of zero trajectories obtained from exact (large blue dots) and approximate (small black dots) models for the *moment* actuator.

find out whether the direct solution of the partial differential equation would lead to the same result as the truncated representation of the same system.

The comparison of the zero trajectory plots obtained using approximate and exact methods for the force actuation case is shown in Figure 2.32. A similar plot for the moment

actuator is shown in Figure 2.34. For the force actuator case, the zero trajectories and the natural frequencies are overlapping. The moment actuator case shows more discrepancy between the assumed mode and the exact the solution but overall the results are sufficiently close to each other. In both cases no real-valued zeroes were extracted from the wave model.

A sample transfer function for the force actuator configuration is shown in Figure 2.33 for a value of the mixing coefficient leading to a real zero pair visible as a circle and a triangle in the pole-zero structure display at the bottom of the magnitude plot. The magnitude and phase plots resulting from the approximate and the exact models match almost perfectly.

Preliminary conclusion based on best modeling effort using approximate and exact methods is that these zeroes are indicative of true non-minimum phase behavior and not results of the modeling technique or modal truncation. The reason for their marked absence from the wave solution remains undetermined. The final decision is reserved until the experimental results are presented.

Chapter 3

EXPERIMENT DESIGN

In Chapter 2 a general concept of a three-element actuator-sensor module (ASM) was presented without discussing the practical aspects of constructing the actuator and the sensors suitable for distributed actuation. The objective of this chapter is to offer a practical ASM design. The design employs a commercially available actuator and strain sensor package and a novel force sensor. This force sensor uses shear piezoelectric effect and is suitable for distributed actuation of beam structures.

The chapter begins by describing the concept of using three piezoelectric patches as components of an ASM. Detailed description of ASM components is presented in the second section. It also includes the description of the proof-of-concept experiment which was performed to verify the feasibility of the shear load cell design. The last section lists the design decisions made while integrating the shear load cell with an actuator and a strain sensor. A finite element model is used to gain insight into the stress and strain distributions inside the ASM components. The details of the manufacturing process and a tabulated summary of measured and estimated properties of the test article are also provided.

3.1 Conceptual Design

In this section a practical design of an actuator-sensor (ASM) module is presented. The details of component design are covered in the next section.

The generalized actuator-sensor module in Figure 2.2 contains three essential elements: the actuator, the low impedance sensor or strain sensor, and the high impedance sensor or force sensor. Following the design process, the practical issues associated with each of these elements are described below.

Actuator

Actuator technology is not the focus of this work, therefore a thin PZT wafer was chosen as the actuator. This active elements type is most commonly used for distributed beam and plate actuation.

Strain Sensor

It is also common to place another active material wafer on top of the actuator and use it as a sensor. The sensor is essentially placed in parallel with the actuator and it measures some combination of strain and force whose exact proportions depend on the relative stiffnesses of the structure, actuator, and sensor. If the sensor element has the same dimensions as the actuator then the two form a collocated actuator-sensor pair. Note that while it is important for the actuator and the sensor to have the same width and length, they can have different thickness or even be made from different piezoelectric materials. These features fit perfectly the requirements for the strain sensor in the three-element ASM.

Force Sensor

The third element needed for the design is a force sensor. In order to act as a load cell, the active element must be placed in the load path between the actuator and the structure. The actuation mechanism modeled in Chapter 2 with an ASM pushing against a riser on the beam would allow an easy placement of the force sensor in line with the actuator. While piezoelectric actuators built for this purpose exist and are used in truss actuation, this approach is not a natural solution for structures in bending because it eliminates the advantage of a surface-mounted piezoelectric wafer: simplicity, compactness, and jointless actuation.

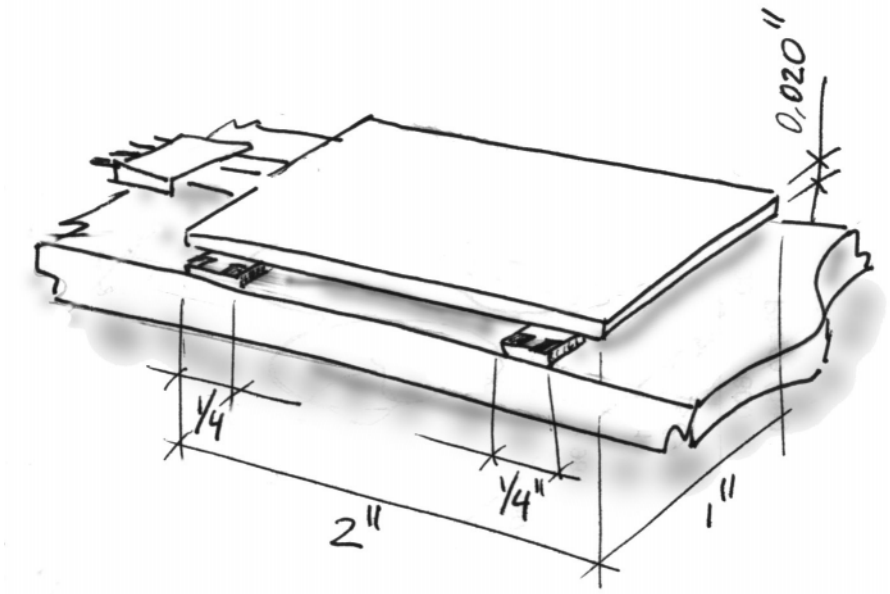

Figure 3.1 Concept sketch of an ASM based on a collocated piezoelectric actuator and strain sensor, and a shear piezoelectric load cell.

The concept drawing of the solution adopted in this work is illustrated in Figure 3.1. It is a hybrid between a typical piezoelectric wafer bonded on the surface of a beam and a stack with discrete attachment points similar to the one modeled in Chapter 2.

A collocated actuator-sensor pair is positioned to span two thin risers placed on the surface of the structure. As the voltage is applied to the actuator it produces actuation strain and applies force to the two risers causing them to deform and transmit the force to the structure below. One of the risers is made out of piezoelectric material and the signal it produces is expected to be closely related to the force developed by the actuator. This active riser is therefore referred to as the force sensor.

The ASM diagram with a mixed virtual sensor output is shown Figure 3.2 and can be directly compared to the general diagram in Figure 2.2. Note that an insert under the left end of the strain sensor is needed for symmetry and it does not have to be made out of active material. Also, the issue of relative placement of the strain sensor and the actuator will be discussed separately and the labels marking their positions in this figure are for

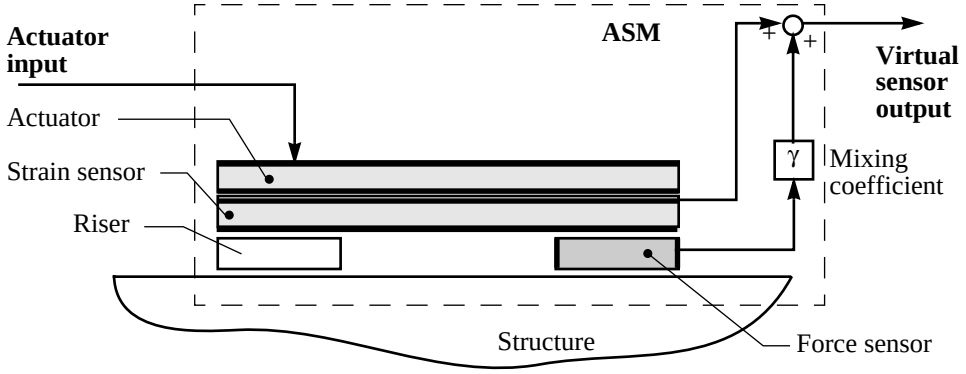

Figure 3.2 Input-output diagram of an ASM based on collocated piezoelectric actuator and sensor and a shear load cell.

illustration purposes only. In the remainder of the chapter the details of the design are presented.

The design parameters which have been discussed so far and are applicable to any design are (i) the location of the ASM on the structure; (ii) the actuator stiffness relative to the structure χ_k; (iii) the strain sensor stiffness relative to the actuator α; and (iv) the force sensor stiffness relative to the actuator β. Note that the relative stiffness definitions are consistent with those in Section 2.1 which focused on a static model of the ASM.

The design parameters specific to this design are (i) the shear load cell width, length, and thickness; (ii) the stacking order in which the actuator and strain sensor are placed onto the structure; and (iii) the choice of the electrodes to be grounded.

The design choices are made based on either the component design in Section 3.2 or the experimental results presented in Chapter 4.

3.2 Component Design

A test article was designed and built by implementing the concept of the actuator-sensor module (ASM) outlined in the preceding section. This section presents the details of engineering design of the main components of the device. The test article is designed as a proof of concept device and the design choices reflect the need for quick and not necessar-

ily the most efficient solutions. First, a brief introduction to piezoelectric properties is given.

Piezoelectric properties

Piezoelectric materials are a class of materials whose constitutive relation couples mechanical stress and strain with electric field and electric displacement. Linear piezoelectric constitutive relations [IEEE, 1978] can be presented in four forms. Using the form in which the electrical field and the mechanical stress are independent variables the material properties are written as,

$$\begin{bmatrix} D \\ S \end{bmatrix} = \begin{bmatrix} \varepsilon^T & d \\ d_t & s^E \end{bmatrix} \begin{bmatrix} E \\ T \end{bmatrix} \tag{3.1}$$

where D is the electrical displacement, S is the strain, E is the electric field, and T is the stress. The complementary electrical and mechanical fields are related through the material properties: the dielectric constant ε^T, the induced strain constant d, and the compliance s^E. The subscript $(\text{-})_t$ denotes a matrix transpose. The superscripts in material properties specify the boundary conditions for which the values were measured. Superscript $(\text{-})^T$ represents a constant stress condition, e.g. free strain. Superscript $(\text{-})^E$ represents a constant electric field condition, e.g. short circuit. The material properties are described in a standard coordinate system, with axes named 1, 2, and 3. The poling direction is by convention chosen to be parallel to the 3 direction.

Equation (3.1) can be expanded into a 9 by 9 matrix and several simplifications can be made. The relationship between the electric field and the electrical displacement is described by a diagonal matrix. Poled piezoelectric material is transversely isotropic about the 3 direction resulting in material properties which are identical in the 1 and 2 directions. The first term in the subscript of the coupling coefficients refers to the electrical axis while the second refers to the mechanical. Thus d_{31} refers to the normal strain developed in the 1 direction (perpendicular to the direction of material poling) in response to a field in the 3

direction (parallel to material poling). Similarly, d_{15} refers to the shear strain in the 5 direction (in plane with material poling) in response to a field in the 1 direction (perpendicular to material poling).

$$\begin{bmatrix} D_1 \\ D_2 \\ D_3 \\ S_1 \\ S_2 \\ S_3 \\ S_4 \\ S_5 \\ S_6 \end{bmatrix} = \begin{bmatrix} \varepsilon_{11}^T & . & . & . & . & . & . & d_{15} & . \\ . & \varepsilon_{11}^T & . & . & . & . & d_{15} & . & . \\ . & . & \varepsilon_{33}^T & d_{31} & d_{31} & d_{33} & . & . & . \\ . & . & d_{31} & s_{11}^E & s_{12}^E & s_{13}^E & . & . & . \\ . & . & d_{31} & s_{12}^E & s_{11}^E & s_{12}^E & . & . & . \\ . & . & d_{33} & s_{13}^E & s_{12}^E & s_{33}^E & . & . & . \\ . & d_{15} & . & . & . & . & s_{55}^E & . & . \\ d_{15} & . & . & . & . & . & . & s_{55}^E & . \\ . & . & . & . & . & . & . & . & s_{66}^E \end{bmatrix} \begin{bmatrix} E_1 \\ E_2 \\ E_3 \\ T_1 \\ T_2 \\ T_3 \\ T_4 \\ T_5 \\ T_6 \end{bmatrix} \tag{3.2}$$

Note that the normal and shear directions are uncoupled.

3.2.1 Actuator and Strain Sensor package: QuickPack

Actuators and sensors used for distributed actuation of beams and plates are typically made out of thin wafers of piezoelectric material poled through the thickness. The electrodes are placed on the top and bottom surfaces of the wafer so the driving or the measured field is parallel to the poling direction.

The equations for the transverse mode of operation in the 1-D case of beam bending is found by eliminating the rows of the equation (3.2) corresponding to the decoupled shear components, the zero field components, and the normal stresses through the thickness and through the width. The independent variables are the electrical field, used as the input, and the stress in the 1 direction.

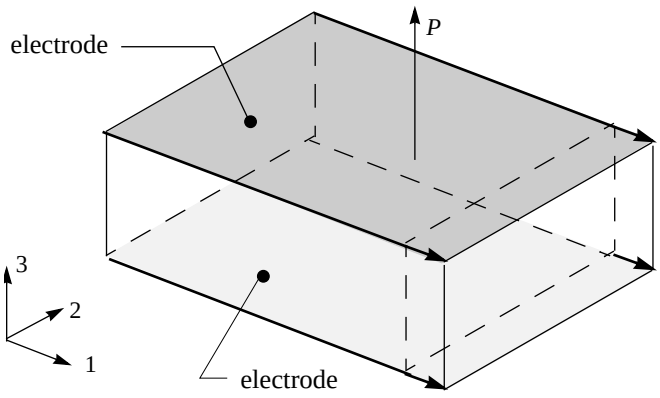

Figure 3.3 Piezoelectric block in transverse extension uses the so-called d_{31} effect for both actuation and sensing.

$$\begin{bmatrix} D_3 \\ S_1 \end{bmatrix} = \begin{bmatrix} \varepsilon_{33}^T & d_{31} \\ d_{31} & s_{11}^E \end{bmatrix} \begin{bmatrix} E_3 \\ T_1 \end{bmatrix} \tag{3.3}$$

An alternative form of the equation is obtained by inverting (3.3) so that the independent variables are the electrical displacement and strain in the 1 direction.

$$\begin{bmatrix} E_3 \\ T_1 \end{bmatrix} = \frac{1}{\varepsilon_{33}^T s_{11}^E - d_{31}^2} \begin{bmatrix} s_{11}^E & -d_{31} \\ -d_{31} & \varepsilon_{33}^T \end{bmatrix} \begin{bmatrix} D_3 \\ S_1 \end{bmatrix} \tag{3.4}$$

Note that for the case of a sensor connected to a high-impedance measuring device, the electrical displacement is small and the voltage output depends only on the shear deformation. An alternative form of measuring the signal is to connect the sensor to a charge amplifier in which case the signal is proportional to the electrical displacement D_1. Both options are discussed in Chapter 4 while presenting experimental results.

The ASM test article is based on a commercially available two-ply piezoelectric package offered by Active Control Experts[1]. The specific model used is *QuickPack QP20N*. The active element is made out of a variation of PZT piezoelectric material and the dimensions

1. Active Control Experts, Inc., Cambridge, MA, USA.

for each ply are 1.81 in long, 0.81 in wide, and 0.010 in thick. The capacitance of the pack (both plies) is reported as 0.11 μF.

The device was chosen because of its availability, ease of use, and because its two-ply construction makes it a collocated actuator-sensor pair. The decision to use a QuickPack constrained the design in the α direction at the point of equal stiffness for the actuator and the strain sensor, i.e. $\alpha = 1.0$.

3.2.2 Force Sensor: a Shear Load Cell

The total deformation of the force sensor placed as in Figure 3.2 is a combination of shear deformation due to the actuation force and the deformation due to the bending and extension of the underlying structure. Since we are interested in obtaining the signal related to the force, it is desirable to construct a sensor which produces a signal proportional primarily to the shear deformation in the piezoelectric block.

The shear parameters in the constitutive relations in (3.2) are decoupled from their normal counterparts and the coupled equations are given as follows,

$$\begin{bmatrix} D_1 \\ S_5 \end{bmatrix} = \begin{bmatrix} \varepsilon_{11}^T & d_{15} \\ d_{15} & s_{55}^E \end{bmatrix} \begin{bmatrix} E_1 \\ T_5 \end{bmatrix} \tag{3.5}$$

The decoupled nature of the constitutive relations means that in order to sense shear deformations in the 1 direction, the electrical field in the 1 direction must be measured and the electrodes must be positioned as in Figure 3.4. This is an unusual electrode configuration because for a typical patch of piezoelectric material, the dimension in direction 3 is much smaller than in the other two directions making it difficult to position the electrodes.

An alternative form of the equation is obtained by inverting (3.5) so that the electrical displacement and the strain are independent variables.

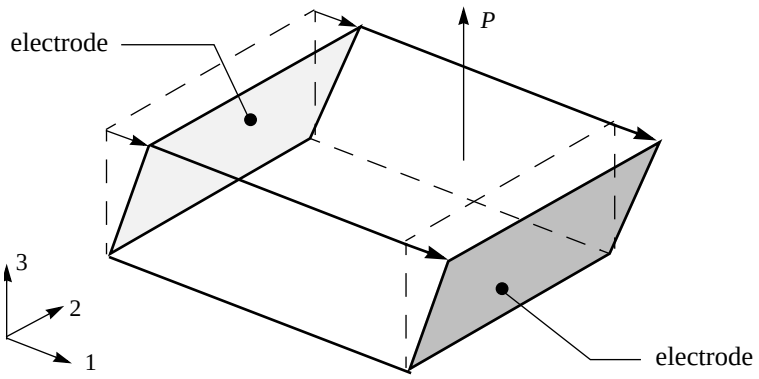

Figure 3.4 Piezoelectric block in shear uses the so-called d_{15} effect for shear strain sensing.

$$\begin{bmatrix} E_1 \\ T_5 \end{bmatrix} = \frac{1}{\varepsilon_{11}^T s_{55}^E - d_{15}^2} \begin{bmatrix} s_{55}^E & -d_{15} \\ -d_{15} & \varepsilon_{11}^T \end{bmatrix} \begin{bmatrix} D_1 \\ S_5 \end{bmatrix} \tag{3.6}$$

Simple analysis of the prismatic force sensor in shear is questionable because its expected small thickness leads to an extremely low aspect ratio. Pure shear deformation is nevertheless a limiting case worth considering. Besides the obvious dependence on the material properties, the voltage on the electrodes of a piezoelectric block under pure shear deformation is directly proportional to the applied force and inversely proportional to its width (dimension in the 1 direction). The voltage does not depend on the block's thickness (dimension in the 2 direction) because the electrical field is proportional to strain which remains the same for a thicker piece. The voltage does not depend on the length of the piece in (dimension in the 1 direction) because for a longer piece the stiffening effect is counterbalanced by the larger separation between the electrodes which for a constant field leads to a higher voltage. Again, pure shear strain conditions are not expected in the shear load cell, and the information above is provided only to clarify the design issues.

Proof-of-Concept Experiment

A simple fixture was built to verify feasibility of building a piezoelectric shear load cell. Its sketch and a photograph are shown in Figure 3.5 and Figure 3.6. Four piezoelectric

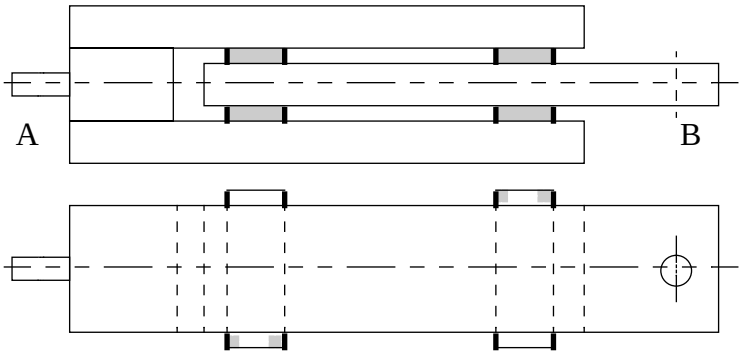

Figure 3.5 Sketch of the shear load cell proof-of-concept device.

patches were bonded between three strips of fiber-glass. Fiber glass composite was used because it is not conductive and the need to insulate the exposed electrodes was eliminated. All four shear load cells were instrumented in order to compare the consistency of the manufacturing process. The fiber-glass pieces are 0.75 in wide and 0.25 in thick.

The shear load cells were made out of 0.010 in thick sheet of PZT-5A material poled through the thickness. The sensor strips were made 0.75 in long and 0.25 in wide. Nickel electrodes on top and bottom surfaces of the wafer were removed using ferric chloride. Small electrode patches, approximately 1/16 in square, were left in the corners of the wafers and were used later to attach lead wires.

The electrodes on the side surfaces were deposited using P-CS-30 colloidal silver paint made by Energy Beam Sciences[1]. The paint is in liquid state and the manufacturing process consisted of dipping the edges of pre-cut PZT pieces into the paint and allowing to dry. Care was taken to insure continuity of coverage along the edge and to minimize paint runoffs onto the top and bottom surfaces. The electrical resistance between the two ends of the electrode varied between 6Ω and 8Ω for different pieces.

An attempt was made to measure the complex electrical impedance of the piezoelectric block between the two electrodes. Due to the unusual location of the electrodes the equiv-

1. Energy Beam Sciences, Agawam, MA, USA.

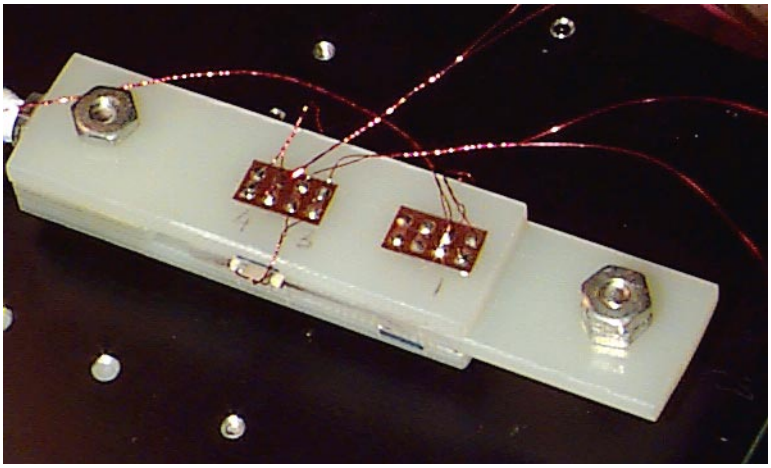

Figure 3.6 Shear load cell proof-of-concept fixture was built out of fiber-glass and four PZT blocks.

alent capacitance of the piezoelectric block cannot be found by the two-infinite-parallel-plates approximation typically used for thin piezoelectric sheets. The arrangement is better viewed as two parallel wires separated by a material of known dielectric constant. It was found experimentally that the measured equivalent capacitance is very dependent on the grounding scheme and the environment. Measured capacitance on the order of 100 pF was typically observed.

During the experiment the test fixture was mounted vertically on a shaker with a load cell placed between the shaker and the mounting point A. The measured transfer functions from the force applied to the fixture to the output of the shear sensors was encouraging for the work to progress into the stage of designing and building the actuator-sensor module using the shear load cell as a force sensor.

3.3 Component Integration and Manufacturing

In this section design issues specific to the interaction of the components comprising the actuator-sensor module (ASM) are discussed. A low-fidelity finite element model of the ASM used in the design process is introduced. The section also describes the test article used in obtaining experimental data presented in Chapter 4.

The design decisions discussed below are (i) the choice of locations of the active and passive risers; (ii) shear load cell thickness, width, and length; (iii) location of the shear load cell relative to the actuator and strain sensor package; (iv) stacking order of the actuator and strain sensor.

Instead of deciding a priori on which of the two risers to make active, both of them made out of PZT-5A and both were instrumented with electrodes and lead wires.

The design decision on the thickness of the shear force sensor was driven mostly by considerations of stiffness, compactness, and manufacturability. The first two drive the thickness down and the last drives it up. Higher stiffness is required for better actuation efficiency and better pole-zero separation in the strain sensor transfer function as was shown in Chapter 2. Thinner shear sensors decrease the overall height of the device and reduce the gap between the structure and the actuator-sensor package bridging the two sensors making it less damage prone. Thicker electrodes make it easier, at least in the experimental stage, to deposit electrodes on the sides of the piezoelectric sheet. The 0.010 in thickness of the shear sensors was chosen as a compromise between the available 0.005 in and 0.020 in PZT sheets. In the hindsight, it appears possible to deposit electrodes on a 0.005 in thick piece using the present technique.

The width of the shear sensors (dimension across the beam) was chosen to be 1/8 in wider than a QuickPack to allow the some space for lead wire connection. Having experienced one of the connectors break on the proof-of-concept fixture, lead wire connectors were positioned on both sides of the shear sensor in case one of them was damaged.

The length of the shear sensors (dimension along the beam) was at first chosen based on engineering judgement and then validated through finite element analysis. The obvious bounds on the length of the sensors are “as small as practically possible” on the low side and almost half-length of the QuickPack on the high side. A shorter sensor is lighter which is likely to be important for high-performance structures. A longer sensor is stiffer and

also reduces the span of the unsupported actuator-sensor pack positioned above. No attempt was made to optimize the sensor length and the length was picked to be 1/4 in.

The location of the sensors was also picked based on engineering judgment. It has been shown that most of the strain is transferred into the structure at the tips of the piezoelectric wafer [References]. It is therefore logical to position the two shear sensors such that their outside edges are directly under the edges of the active elements inside the QuickPack.

The decision on which QuickPack ply to use as an actuator was originally based on the assumption that by placing the sensor between the actuator and the structure pole-zero spacing would improve because “more information” about the structure is extracted from the sensor. This decision was verified experimentally as described in Chapter 4.

Finite-Element Model

A two-dimensional low-fidelity finite element model (FEM) was created to verify that the expected output levels from a shear load cell are measurable and to gain insight into the approximate strain and stress distributions in the components. It would have been useful to have a model accurate enough to reliably predict the frequency response of the system. Such model would have allowed to make more informed decisions on sizing and positioning the parts by considering the impact on the pole-zero structure. However, small feature sizes, large aspect ratios, and poorly known material properties of the piezoelectric and the epoxy did not allow to create such model in a reasonable amount of time.

A commercial FEM package ANSYS[1] was used for the analysis. A sample mesh is shown in Figure 3.7. Coupled field plane stress elements were used to model piezoelectric material. A short cantilever aluminum beam is modeled using plane stress finite elements. A shear load cell is represented by a rectangular block offset from the strain sensor material above it in order to allow the voltage degrees of freedom in the strain and force sensors to remain independent from each other. The nodes on the left and right sides of the shear sen-

1. ANSYS 5.3, Swanson Analysis Systems, Houston, PA, USA.

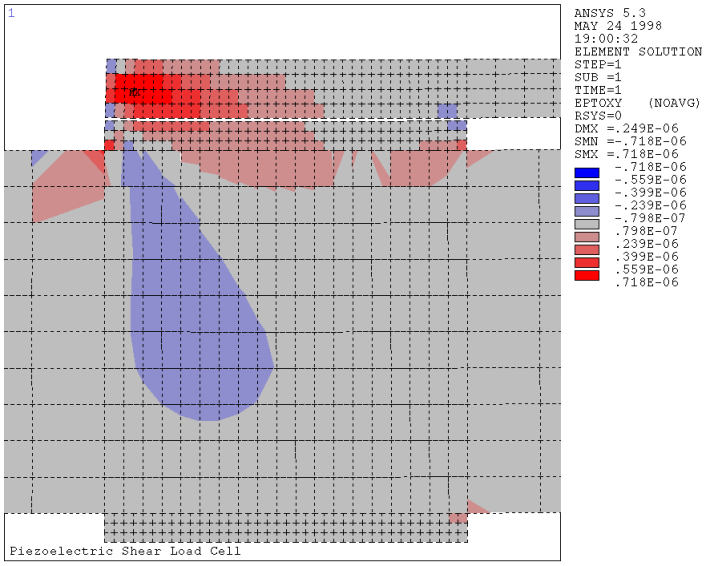

Figure 3.7 FEM results for shear strain distribution in the vicinity of a shear load cell for a simplified representation of an ASM.

sor block have coupled voltage degrees of freedom to represent electrodes. Two layers of piezoelectric material represent a QuickPack. Nodes in the top, bottom, and middle rows have coupled voltage degrees of freedom representing QuickPack electrodes. The middle electrode is grounded.

Another rectangular piezoelectric block is placed on the bottom surface of the beam opposite the shear sensor. It represents one of two dummy sensors intended to be placed on the test article in order to compare their output signals with those from the shear sensors. Like the shear sensor the dummy sensors have electrodes on the sides.

A static shear strain solution is shown in Figure 3.7. A 1 V potential applied at the top electrode causes the actuator to contract which in turn deforms the shear load cell and the structure. More shear deformation is visible towards the left side of the load cell. As expected, very little shear deformation is present in the dummy sensor visible on the bottom of the figure.

The nodal voltage solution for the same loading condition as above is shown in Figure 3.8. The electrode on the left side of the shear sensor is grounded. The voltage distribution

offers no surprises.The predicted output level is certainly high enough to be measured. Note that the software is somewhat misleading in extrapolating the values of the voltage degrees of freedom into the aluminum elements below.

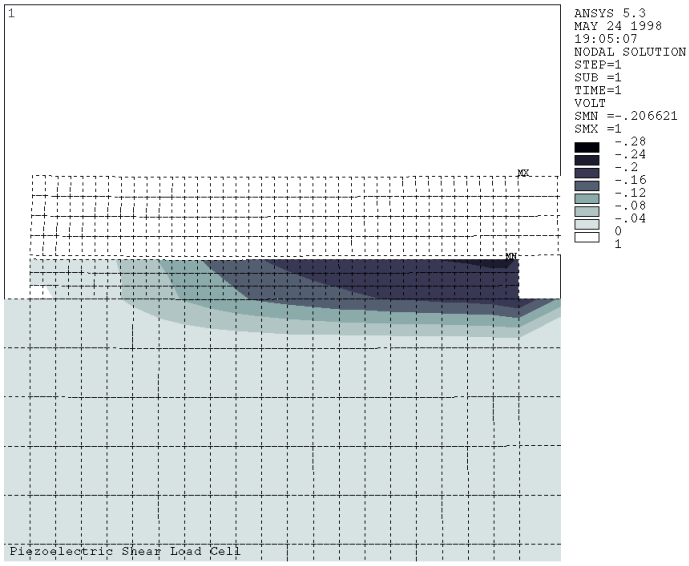

Figure 3.8 FEM results for voltage distribution in a simplified representation of an ASM.

The FEM results indicated that the strain, stress, and voltage distributions were not particularly sensitive to the length of the shear force sensors. The decision was made to leave the width at approximately 1/4 in, the size already tested in the proof-of-concept experiment.

A detailed view of the manufactured device is shown Figure 3.9. A QuickPack with a large connector plug is visible in the center. Two shear sensors with their individual lead wires are seen near the edges of the QuickPack.

Complete Test Article

A cantilever aluminum beam was chosen as the structure for ASM testing. The beam was made out of 5052 aluminum and with dimensions 9.5 in long, 1.25 in wide, and 0.126 in thick. The fundamental bending frequency of the bear beam is 45 Hz. An actuator-sensor module was attached near the root of the beam as shown in Figure 3.10. The placement

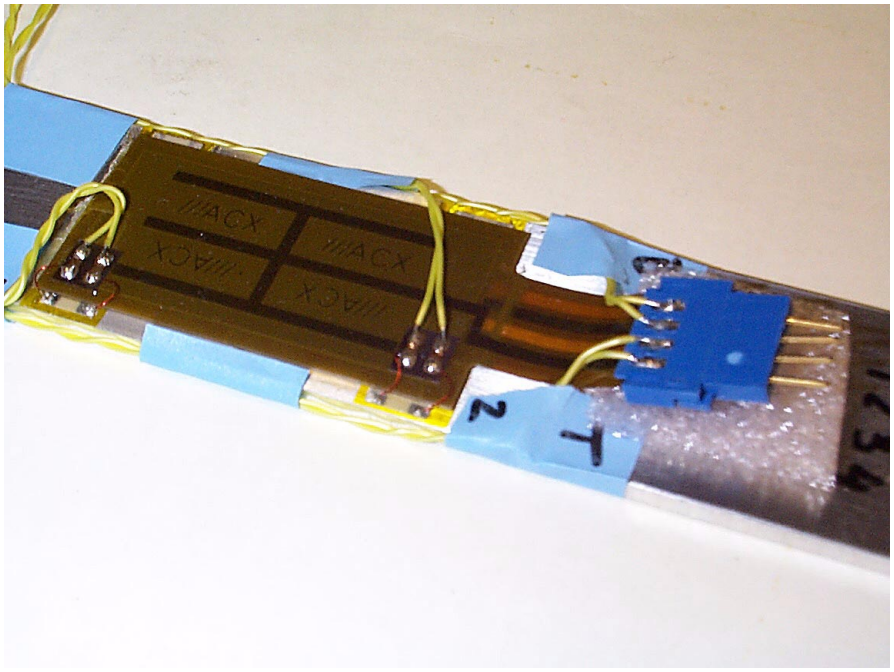

Figure 3.9 Actuator-sensor module (ASM) mounted on an aluminum beam.

near the root offers good actuation authority due to high strain levels in the low-frequency modes.

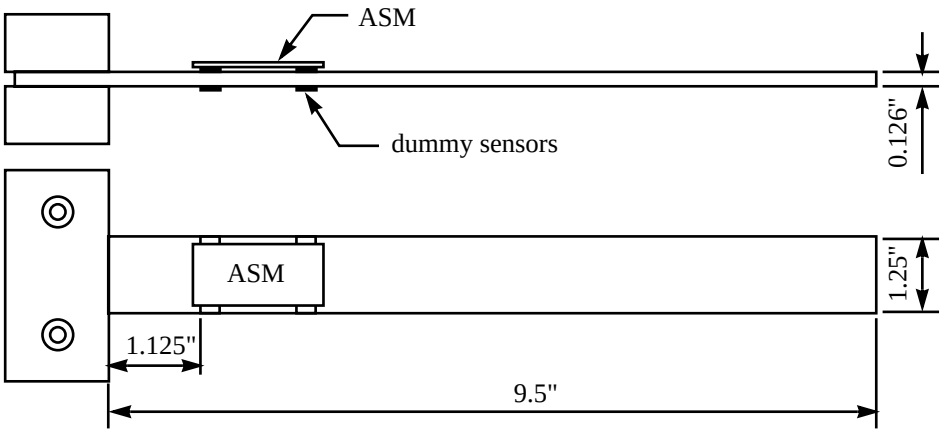

Figure 3.10 The test article is a cantilever aluminum beam with an ASM attached near the clamp on one side of the beam and two dummy sensors on the opposite side.

To prevent the electrodes of the shear sensors from being shorted by exposure to the conductive beam, a layer of 0.001 in thick Kapton film was placed between the ASM and the

beam. All components were bonded at the same time using ACX QuickPack epoxy recommended for bonding QuickPack piezoelectric actuators. The combined thickness of the assembled shear sensors including two epoxy layers and the thickness of the insulation was measured to be 0.014 in. The total height of the module assembly above the beam surface including the QuickPack and one more epoxy layer is 0.035 in. The total mass of the fully instrumented module mounted on the beam was 8 g including 5.5 g for the QuickPack.

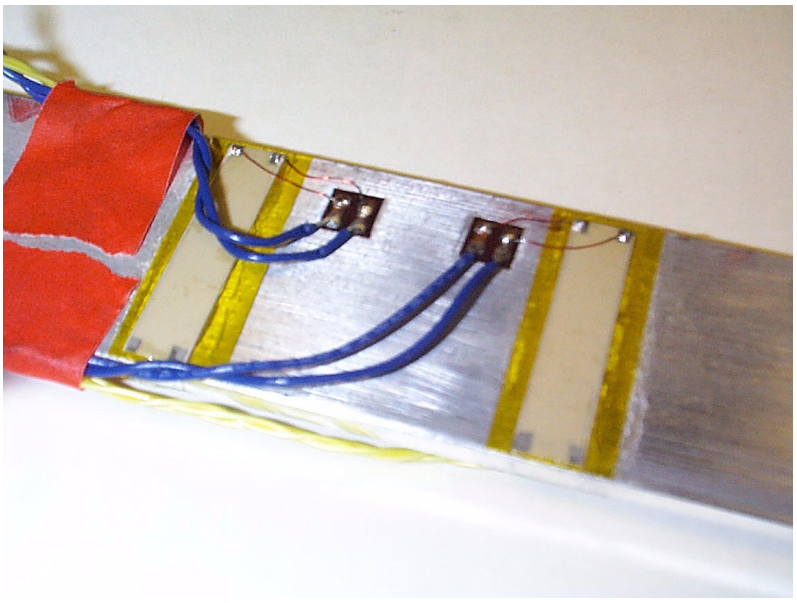

Figure 3.11 Dummy sensors are located on the back side of the beam directly opposite the shear sensors built into the ASM; an electrically insulating layer of Kapton is visible under the sensors.

To quantify the degree of decoupling between the normal and shear strains in a realistic piezoelectric material, two dummy sensors were placed on the back side of the beam. The dummy sensors have the same dimensions, were made out of the same batch of PZT, electroded using the same procedure as the shear sensors and were placed at the same position along the beam opposite the shear sensors. A photograph of the back side of the beam is shown in Figure 3.11. The shear and dummy sensor transfer functions are compared in Chapter 4.

The final design choice is electrode grounding scheme. Finite element analysis showed that the transfer functions are influenced by this decision. Since the model was not accurate enough to be trusted, it was decided to make this decision based on the experimental data.

Modified Four-Element Static Model

Compared to the ASM topology assumed in the development of the static model in Chapter 2, the present design consists of four elements: the actuator, the strain sensor, and *two* shear load cells. In order to use the results of the model, small modification must be made. Most importantly, the formulae for the special values of the mixing coefficient have to be modified. The modified system diagram is shown in Figure 3.12

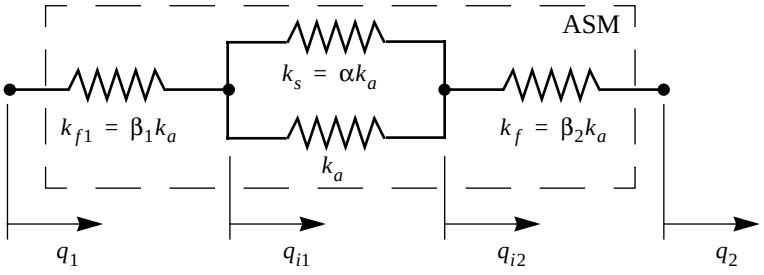

Figure 3.12 Diagram of the static model of a four-element ASM with two load cells.

Because the modeling approach remains static the two stiffness corresponding to the two shear sensors can be combined and their effective stiffness equals $\beta_0 = \frac{\beta_1\beta_2}{\beta_1 + \beta_2}$. Equation (2.18) for the mixed output is re-derived and the new version has the same form with the normalized stiffness of the single force sensor β replaced with the effective stiffness of two force sensors β_0. The special values of the mixing coefficient obtained from this expression are given below,

$$\begin{aligned}\hat{\gamma}_C &= \frac{\chi_c}{\chi_y}\frac{\beta_0}{1+\alpha} \\ \hat{\gamma}_S &= -\frac{\chi_c}{\chi_y} \\ \hat{\gamma}_F &= -\frac{\chi_c}{\chi_y}\left(1+\hat{\chi}_k^E\frac{1+\alpha+\beta_0}{1+\alpha}\right)\end{aligned} \tag{3.7}$$

where $\hat{\chi}_k^E = \frac{k_0^E}{k_{beam}^E}$ is the modified structure/ASM relative stiffness parameter, the modified ASM equivalent stiffness is calculated as $k_0^E = \frac{(1+\alpha)\beta_0}{1+\alpha+\beta_0}k_a$, and k_{beam}^E is the static driving point impedance of the experimental setup which can be approximated by k_{beam}^M given in (2.73). The difference between k_{beam}^E and k_{beam}^M is due the fact that in the experimental setup, the ASM is not attached to the clamp as was assumed in Chapter 2 but is offset by 1.125 in.

Calculation and Estimation of ASM Parameters

In order to relate the results obtained in Chapter 2 to the experimental results in Chapter 4, the parameters describing the test article must be collected. The important ones are summarized in Table 3.1. The relative stiffness of the force sensor proved to be particularly challenging to determine.

The actuator stiffness was calculated using the dimensions for one QuickPack ply and the modulus of elasticity $E_{QP} = 120GPa$. The relative stiffness of the strain sensor is set by the choice of a two-ply QuickPack to act as an actuator and a sensor, $\alpha = 1$. The relative stiffness of the shear load cell was difficult to calculate analytically or using the FEA model because the dimensions and stiffnesses of multiple bonding layers were not accurately known.

An attempt was made to estimate the shear sensor stiffness by measuring the longitudinal natural frequencies of a QuickPack under free-free condition and compare those to the longitudinal frequencies of the QuickPack mounted on the shear sensors. The two shear sensors were viewed as springs and by knowing the change in frequencies during the tran-

TABLE 3.1 Summary of ASM and test article parameters.

Parameter	Value	Source of data, notes
Strain sensor normalized stiffness	$\alpha = 1$	By design, two equal stiffness QuickPack plies
Force sensor normalized stiffness	$\beta \approx 1.33$	Estimate, based on experimental zero trajectory plot, procedure described in Section 4.2.
ASM equivalent stiffness	$\kappa = 0.4$	Calculated according to (2.4)
Actuator stiffness	$k_a = 7.5 \cdot 10^6 \left(\frac{N}{m}\right)$	Calculated according to (2.5)
ASM mass	$m = 8(g)$	Measured
Beam parameter	$a = 80.6\left(\frac{1}{s}\right)$	Calculated as $a = \frac{EI}{mL^4}$
ASM moment arm	$h = 0.100(in)$	Measured
Relative ASM/structure stiffness parameter	$\chi_k^M = 0.74$	Calculated according to (2.73). The impedance matched value from $\bar{\chi}_k^M \approx 1$ (an approximation because ASM is not at the clamp).

sition from free-free to spring-spring boundary conditions the required spring stiffness could be calculated. An impedance analyzer was used to estimate the natural frequencies of the electro-mechanical system which eliminated the need for using shakers or sensors. Unfortunately the measured frequencies under two boundary conditions did not correlate well and a different approach described in Chapter 4 had to be used.

The normalized shear sensor stiffness was estimated to be $\beta = 1.33$ based on the experimental data and the properties of zero trajectory plots. The procedure for estimating β is described in Section 4.2. The equivalent stiffness of the ASM based on the value of β above was found to be $\kappa = 0.45$. The ASM/structure relative stiffness $\chi_k^M = 0.74$ can be compared to $\bar{\chi}_k^M = 1$ for the case of ASM/structure impedance matching, indicating that the present ASM design is approximately 25% softer than the target medians matched value.

The internal resonances of the ASM are important because they set the frequency up to which the behavior of the ASM can be considered quasi-static. Using the Hewlett-Packard 4194A impedance analyzer the complex impedances of electro-mechanical systems can be measured. Two measurements were made: (i) complex electrical impedance of the QuickPack by itself and (ii) a QuickPack assembled into the ASM and mounted on a beam. The extension and bending modes of the QuickPack can be effectively separated by connecting the electrodes of the two plies to the terminals of the analyses in such a way that the plies are driven in or out of phase with each other. This method gave good results for a suspended QuickPack with approximately free-free conditions. The frequencies for both bending and extensional vibrations correlated well with the analysis. When mounted on the shear sensors, the boundary conditions for both types of vibrations become spring-spring with unknown extensional and rotational spring stiffnesses. For these boundary conditions the fundamental frequencies are lower than for the free-free conditions. In addition, due to the changed geometry the bending and extensional vibration can no longer be easily decoupled.

The fundamental bending frequency of the QuickPack by itself under free-free conditions was calculated and experimentally verified to be not lower than 850 Hz. The lowest extensional frequency of the QuickPack by itself was measured at approximately 30 kHz. The low frequency modes of the ASM mounted on the beam were unobservable through the impedance analyzer and could not be measured. The FEA model showed high degree of coupling between bending of the beam and bending of the actuator / strain sensor package starting with the second bending mode of the beam at approximately 280 Hz.

Based on this limited information it can be concluded that the quasi-static range of the present design of the ASM does not extend high enough to be ignored when used for control. Therefore care must be taken to minimize the degree of interaction between the structure and the module or the module dynamics must taken into consideration in the control design.

Summary

The ASM design proposed at the beginning of the chapter uses a standard component for actuator and strain sensor and focuses attention on an novel force sensor which uses piezo-electric shear effect to measure shear force. Trial force sensors were built and a proof-of-concept experiment was conducted.

Chapter 4

EXPERIMENTAL RESULTS

This chapter presents experimental results obtained for the test article whose design and manufacturing details were described in Chapter 3. The primary objective of the experiments described in this chapter is to experimentally verify the feasibility of controlling the pole-zero structure of the plant transfer function by mixing the outputs of the two available sensors. Experimental results are correlated to the predictions of simple models considered in Chapter 2.

The chapter begins by describing the experimental setup and procedure. First, the experiments conducted to gather the information necessary for finalizing the test article design are described. The main part of the chapter covers the experimental transfer functions of the two sensors and the experimental mixed transfer functions. Discussion of the results and conclusions are presented in the last section.

4.1 Hardware

This section describes the laboratory equipment and procedure used to record the experimental transfer functions.

A block diagram of the data acquisition system is shown in Figure 4.1. The setup was used to record both the individual sensor transfer functions and the experimentally mixed trans-

fer functions. A Siglab Model 20-42 4 channel Fourier analyzer was used as the main measurement tool. The analyzer's bandwidth is 20 kHz.

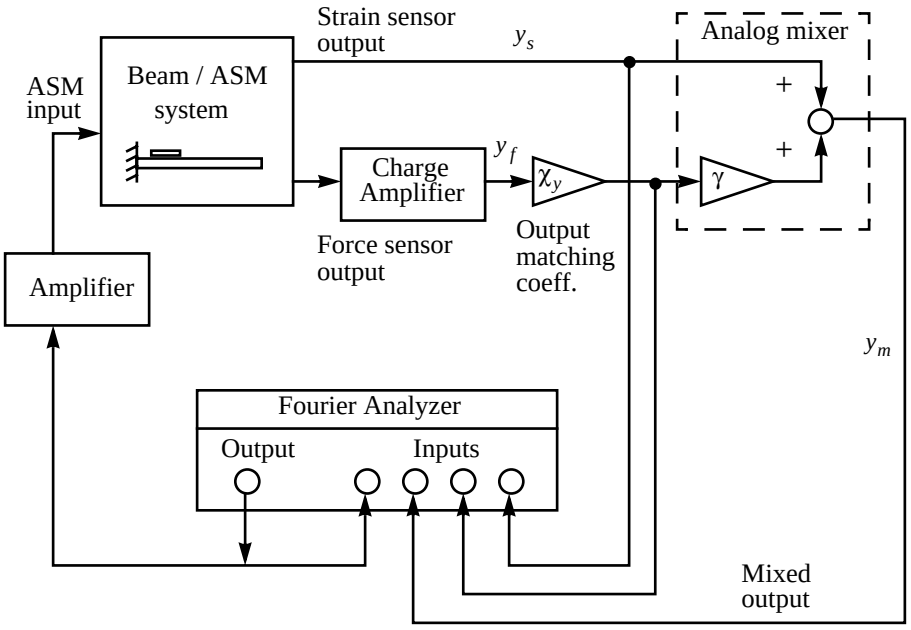

Figure 4.1 Block diagram of the data acquisition system.

The low-current driving signal generated by the output channel of the Fourier analyzer was amplified by a Crown D-150A Series II amplifier with maximum power of 750 W. Typically, an amplification factor of approximately 5 was used, setting the driving signal applied to the ASM in the region between 2.5 V at high frequencies and 7.5 V at low. The driving signal was applied to the actuator ply of the QuickPack which typically was the top ply.

The output from the sensor ply of the QuickPack acting as a strain sensor was fed directly into one of the input channels of the Fourier analyzer. The bottom ply was typically used as a sensor. The output of the force sensor was passed through an Endevco model 2721 charge amplifier. The resulting voltage signal was amplified in an analog circuit representing the output matching gain χ_y described in Section 2.1. The phase loss associated with the analog circuit was measured to be approximately 5 degrees at 5 kHz.

A photograph of the beam mounted in a clamp is shown in Figure 4.2. The accelerometer

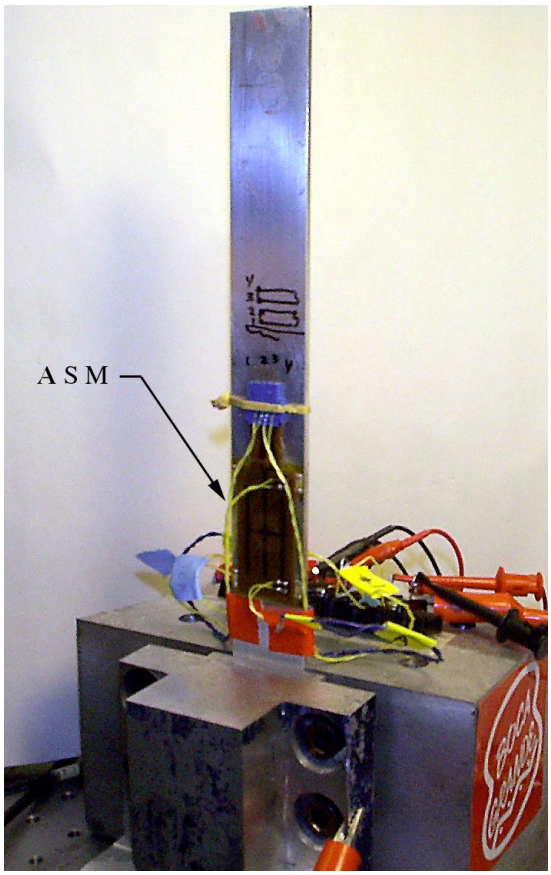

Figure 4.2 Test article in a clamp mounted on an optical bench.

seen in the picture was originally used to verify the finite element and Rayleigh-Ritz models, but was subsequently removed from the beam.

A charge amplifier was used to condition the output of the shear sensor but not the output of the strain sensor because of the difference in equivalent capacitances of the two active elements. The corner frequency for an RC circuit associated with a piezoelectric wafer connected to a high-impedance measuring device such as a Fourier analyzer is inversely proportional to the capacitance of the piezoelectric ($\omega_0 = \frac{1}{RC}$). The measured capacitance of the QuickPack ply was found to be three orders of magnitude higher than that of a typical shear sensor (see hardware description in Chapter 3). Therefore the corner fre-

quency of the high-pass filter for the shear sensor is significantly higher and is more likely to be in the bandwidth of interest.

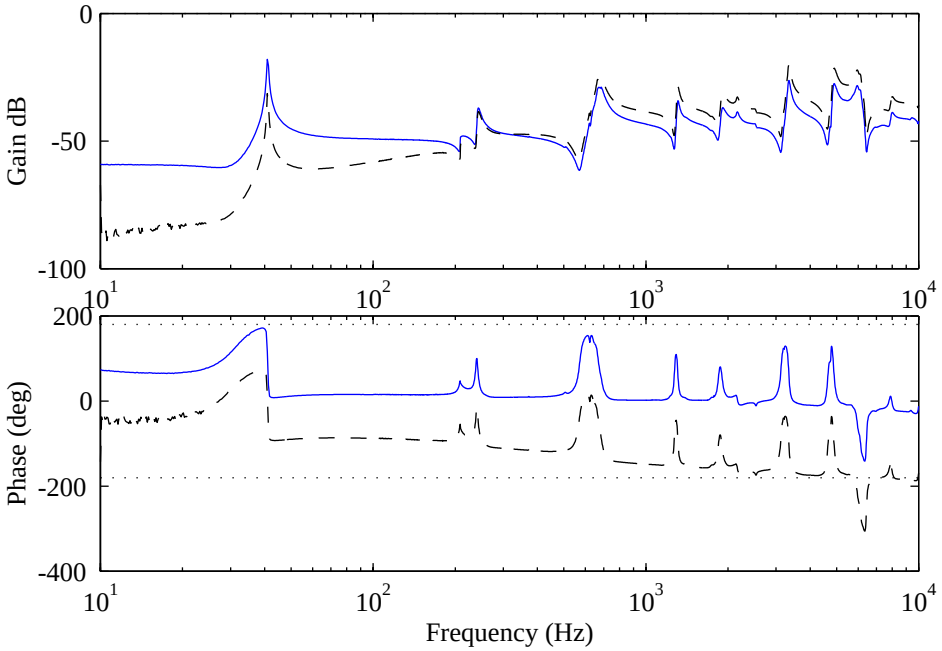

Figure 4.3 The output of the shear sensor # 2 passed through a charge amplifier (solid) and measured directly by the data acquisition system (dashed).

The effect of using a charge amplifier is illustrated in Figure 4.3. The high-pass filtering with a corner frequency of approximately 600 Hz is clearly visible in both magnitude and phase plots for the signal measured directly by the network analyzer. The filtering effects are not present in the output of the charge amplifier. Otherwise the pole-zero structure remains unchanged.

In the experiments in which the mixed transfer function was measured, the signal from the sensor ply of the QuickPack and the amplified shear sensor signal were combined in an analog circuit which allowed to vary the mixing gain γ from -10 to +10. The amplifying, summing, and inverting analog circuits were implemented using common operational amplifiers.

Note that due to the limitation on the input voltage allowed by the Fourier analyzer, the transfer function input was measured directly from the signal generator therefore making the driving signal amplifier part of the plant. To estimate the true magnitude of the transfer function from the ASM input to the appropriate output, the magnitude of the experimental transfer function must be divided by the amplifier gain which, although was not held constant for all experiments, remained in the region between 5 and 6.

4.2 Transfer Functions

The experiments performed on the test article can be roughly divided into three groups: (i) exploratory measurements with the goal of finalizing design parameters, (ii) individual strain and force sensor transfer functions, and (iii) experimentally mixed transfer functions. These results are presented and discussed in turn.

Phase 1: Finalizing the Design

Recall that two shear sensors were designed into the ASM even though only one of them was needed to produce the mixed transfer function. Both were made functional so that the differences due to the sensor location and manufacturing variations could be observed. The results of the finite-element model showed that the transfer functions to the outputs of the two sensors would be substantially different, however the final decision on which sensor to use for output mixing was based on experimental results.

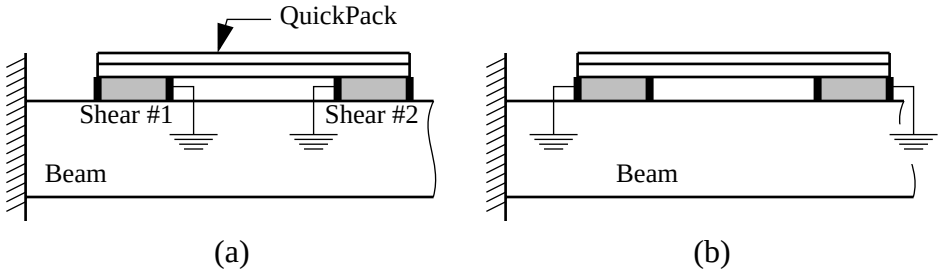

Figure 4.4 Two candidate electrode grounding schemes: (a) both inside electrodes are grounded; (b) both outside electrodes are grounded.

Another design variable which was briefly mentioned in the Chapter 3 is the grounding of the shear sensor electrodes. In general, consistent and thorough grounding proved absolutely critical for measuring meaningful and consistent results. Two possible grounding schemes are illustrated in Figure 4.4. In order to simplify the decision, only symmetric grounding schemes were considered, i.e. both inside or both outside electrodes were grounded at the same time.

Figure 4.5 and Figure 4.6 show four candidate force transfer functions resulting from the choice of two shear sensors and two grounding schemes. A fairly large variation in shape and relative magnitude of the transfer functions is observed.

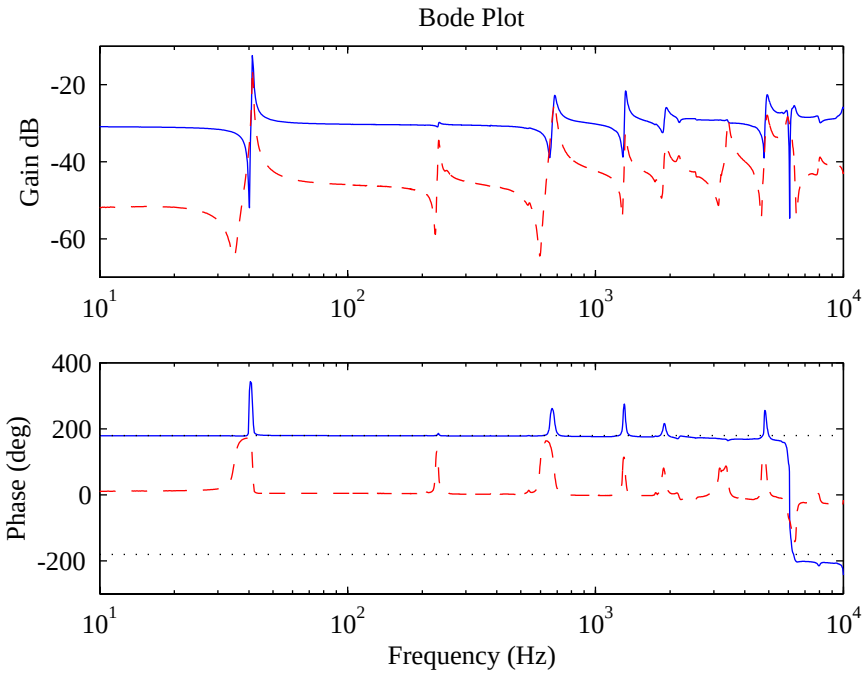

Figure 4.5 Candidate force transfer functions from shear sensors #1 (solid) and #2 (dashed) with *inside* electrodes grounded.

In choosing the suitable sensor and grounding scheme combination two criteria were applied: (i) the frequency at which the alternating pole-zero pattern breaks down and (ii) mode observability in the bandwidth of interest, i.e. the amount of pole-zero separation. Based on these criteria, the combination of shear sensor # 2 (located farther away from the

root of the beam) and the inside electrode grounding scheme were selected. For this transfer function the onset of non-collocation occurs at approximately 6 kHz and modal observability is high, particularly for the mode just above 200 Hz which is nearly unobservable when viewed through two out of four candidate transfer functions.

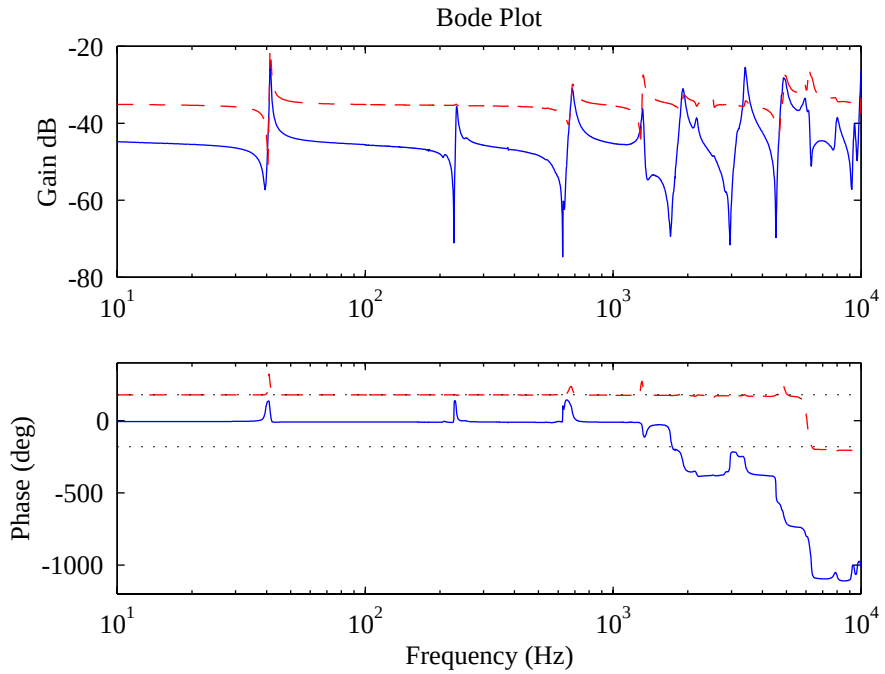

Figure 4.6 Candidate force transfer functions from shear sensors #1 (solid) and #2 (dashed) with *outside* electrodes grounded.

To verify that the signal from the shear load cells is primarily proportional to *shear* strain, the transfer functions to the shear sensor #2 and the corresponding dummy sensor are compared in Figure 4.7. The dummy sensor transfer function does indeed have a different pole-zero structure and has the appearance of a strain transfer function with its characteristic pole-zero-pole structure. Its magnitude is on average at least 10 dB lower than the shear sensor transfer function.

Another design matrix was explored regarding the task assignment and the grounding of the QuickPack plies. The differences between the transfer functions were not as drastic as those for the shear sensors and the details are not presented here. In the final design the top

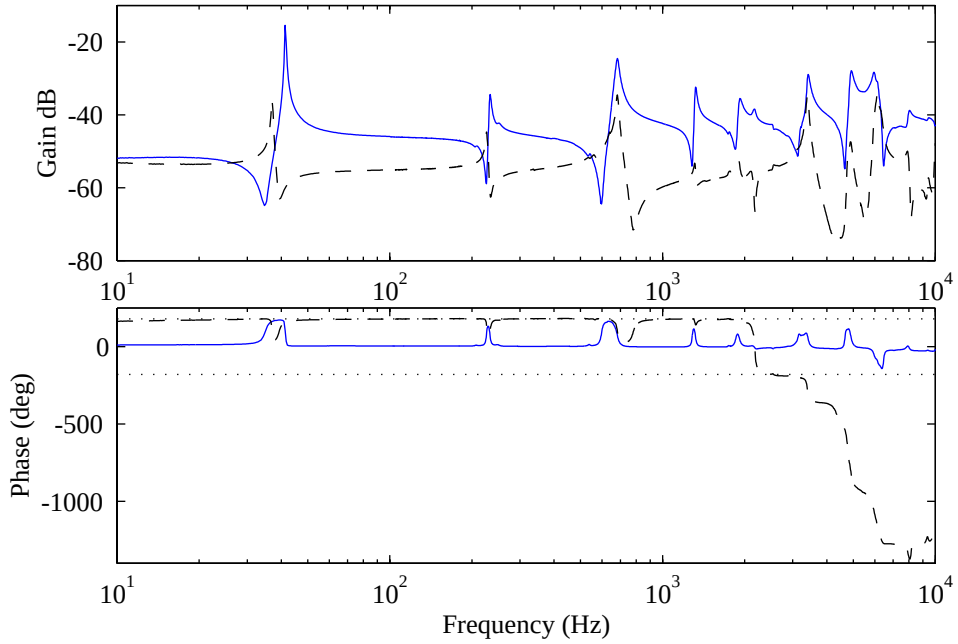

Figure 4.7 Comparison of transfer functions to the shear sensor #2 (solid) and the corresponding dummy sensor (dashed).

ply of the QuickPack acts as the actuator and the bottom ply acts as the strain sensor. With this layout the pole-zero separation in the strain sensor transfer function is wider. A possible physical explanation for this observation is that by placing the sensor between the actuator and the structure more structural information is extracted thus leading to better modal observability and wider pole-zero spacing. In both plies the bottom electrodes were grounded, on the assumption that by grounding the electrode located immediately above the shear sensor the electrical cross talk between the sensors would be minimized. The diagram of the final ASM configuration is shown in Figure 4.8.

Phase 2: Strain and Force Sensor Transfer Functions

With the sensor configuration finalized, the two individual sensor transfer functions were recorded. In order to keep the main mixing coefficient small, the magnitudes of the two transfer functions are roughly equalized by a constant gain χ_y. In the models from Chapter 2 this gain was set to $\chi_y = \bar{\chi}_y = \frac{\beta}{1+\alpha}\frac{c_s}{c_f}$ (2.20). However, as was pointed out in Chapter 3, accurate values for ASM parameters are difficult to obtain due to uncertainties

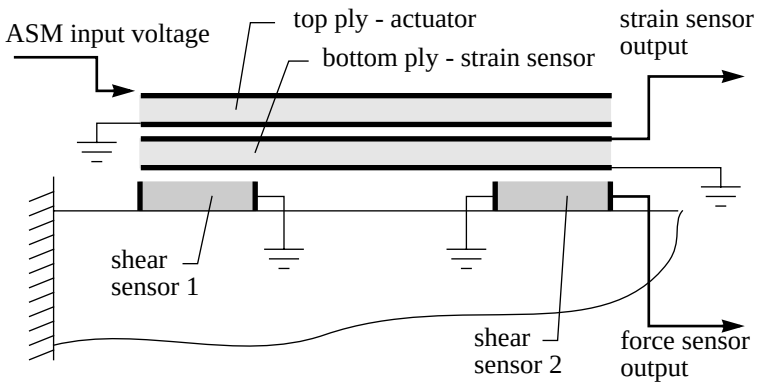

Figure 4.8 Final design of the ASM ply assignments and grounding scheme.

in geometry and material properties. An alternative approach is to manually equalize force and strain sensor transfer functions at an arbitrary frequency. In the current implementation a gain of $\chi_y = 102$ was required to make the magnitude of transfer functions equal at the frequency of 100 Hz.

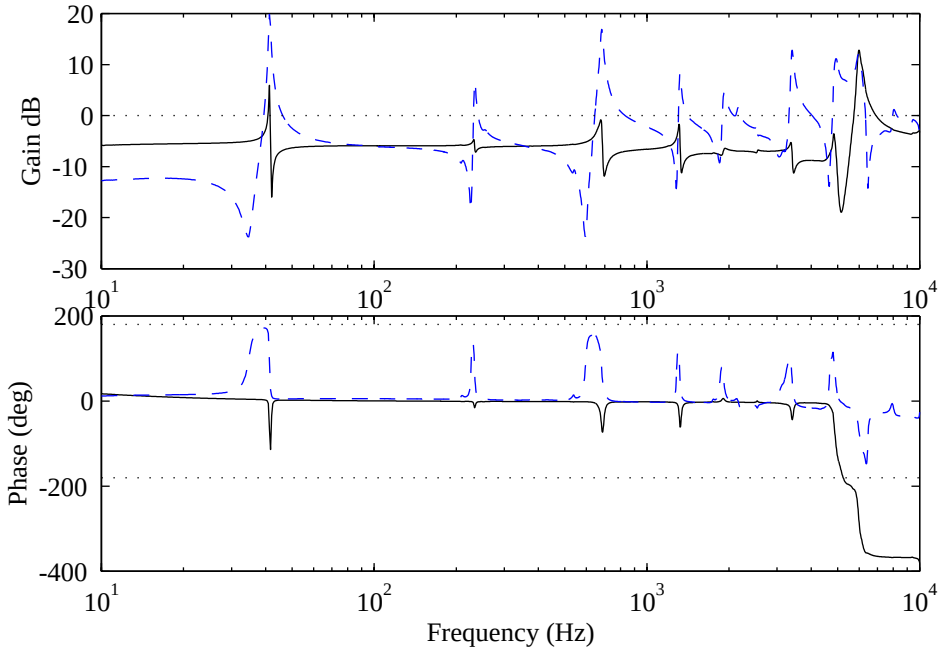

Figure 4.9 Experimental strain (solid) and force (dash) sensor transfer functions adjusted to be equal at 100 Hz.

The Bode plot of the strain sensor transfer function and the *adjusted* force sensor transfer function is shown in Figure 4.9. Note that both transfer functions lose phase at around 5 kHz, indicating loss of collocation. However the drop in the magnitude of the strain sensor transfer function is much lower which leads to a non-minimum phase (NMP) zero in the identified system. Note also a large peak on the magnitude plot at approximately 6 kHz. It corresponds to the first cord-wise bending mode of the beam. Similar results were reported in the past [McCain, 1995; Yung, 1996].

A system identification procedure was performed on the strain and force sensor transfer functions in order to gain insight into the pole-zero structure of the system and to allow to create zero trajectory and zero locus plots. The identified and experimental transfer functions are compared in Figure 4.10 and Figure 4.11. The system was identified as a single-input dual-output linear time-invariant system using Integrated Frequency domain Observability Range Space Extraction and Least Square parameter estimation algorithm (IFORSELS) [Jacques, 1996]. The order of the system was chosen to be 34 states.

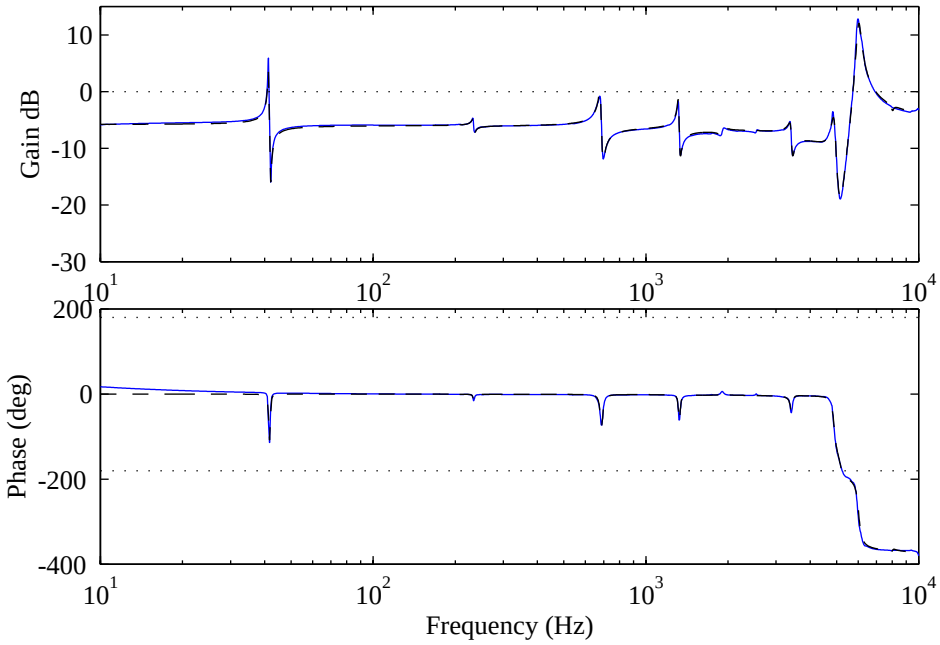

Figure 4.10 Experimental (solid) and identified (dashed) *strain* sensor transfer function.

Note that in the strain sensor output channel, the identified system contains a nearly-symmetric pair of lightly-damped minimum-phase (MP) and non-minimum phase (NMP) zeroes around 5 kHz. The reason for the NMP complex zero in the strain sensor transfer function is unknown. The results were verified by zooming in on the mode in question and performing high-resolution high-gain sine sweep measurements. The 360° drop in phase was consistently observed.

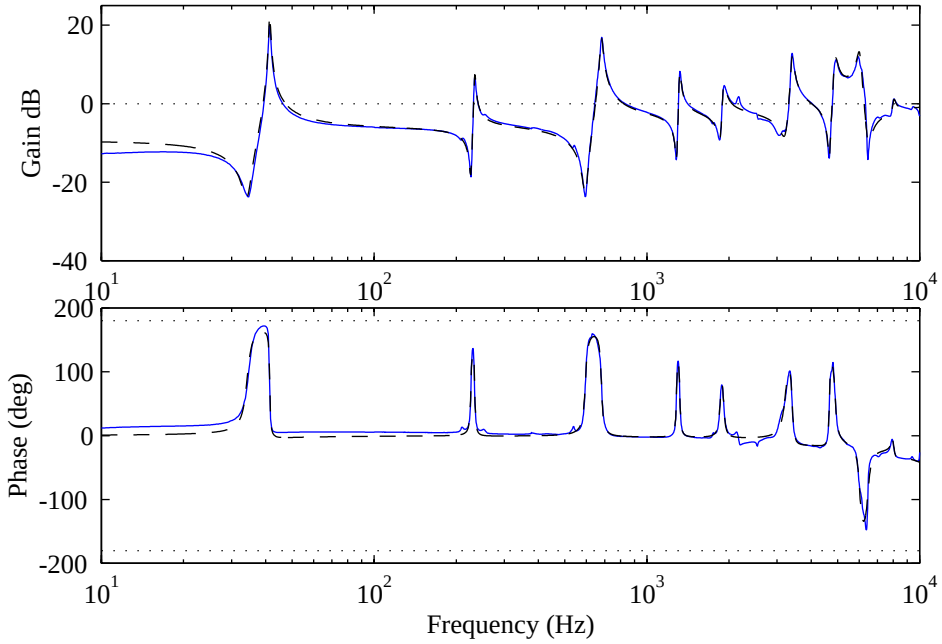

Figure 4.11 Experimental (solid) and identified (dashed) *force* sensor transfer function.

The two outputs of the identified state-space model were mixed in software using a range of mixing coefficients, zeroes of the mixed transfer function were calculated and the resulting zero trajectory plot is shown in Figure 4.12. The original identified model with 34 states had two modes between modes 5 and 6 (see right edge of Figure 4.12) with low observability and controllability. They were nearly unaffected by output mixing and appeared as horizontal lines, similar to mode 4 in the model of the ASM acting as a moment actuator (see Figure 2.23). These two modes were removed from the model to clarify the picture.

Above the sixth mode the zero branches clearly do not follow the pattern set by the simple models from Chapter 2. Another feature of zero trajectory plot not previously encountered is the MP real-valued branch curving away from the γ_S asymptote.

Recall that an earlier attempt to estimate the relative force sensor stiffness failed as was described in Chapter 3. Another opportunity to obtain an estimate comes from examining the zero trajectory plots. Knowing the expected general appearance of the plot the special values of the mixing coefficient can be picked off. The mixing gain γ_F^e lies on the intercept of the lowest zero branch in the negative range of mixing coefficients and γ_S^e is the easiest to identify on the plot of real zeroes as the asymptote for the two real-valued branches. The superscript e stands for *experimental*. The value of γ_C^e is found at the intersection of the zero branches and the pole frequencies but the shallow slope of the zero trajectories makes the crossover point very sensitive to errors in data acquisition and system identification. Out of the three data points the one corresponding to pole-zero cancellation is most suspected of being incorrect.

As was pointed out in Chapter 3, the arrangement of the practical implementation of the ASM differs from the static model considered in Chapter 2 in that the actuator-sensor pack is mounted on *two* compliances while the in static model only one of them had finite stiffness. The modified expressions for the special values of the mixing coefficient were given in (3.7). The three equations for the measured mixing coefficients γ_F^e, γ_S^e, and γ_C^e can be separated into the known parameters on the right and the two unknown parameters $\beta\chi_c$ and χ_c on the left.

$$\begin{aligned} \beta_0\chi_C &= (1+\alpha)\chi_y\gamma_C^e \\ \chi_C &= -\chi_y\gamma_S^e \\ \frac{k_a}{k_{str}}\beta_0\chi_C + \chi_C &= -\chi_y\gamma_F^e \end{aligned} \tag{4.1}$$

Note that in the last equation, the expression for the ASM equivalent stiffness was substituted into (3.7) to avoid iterative solution.

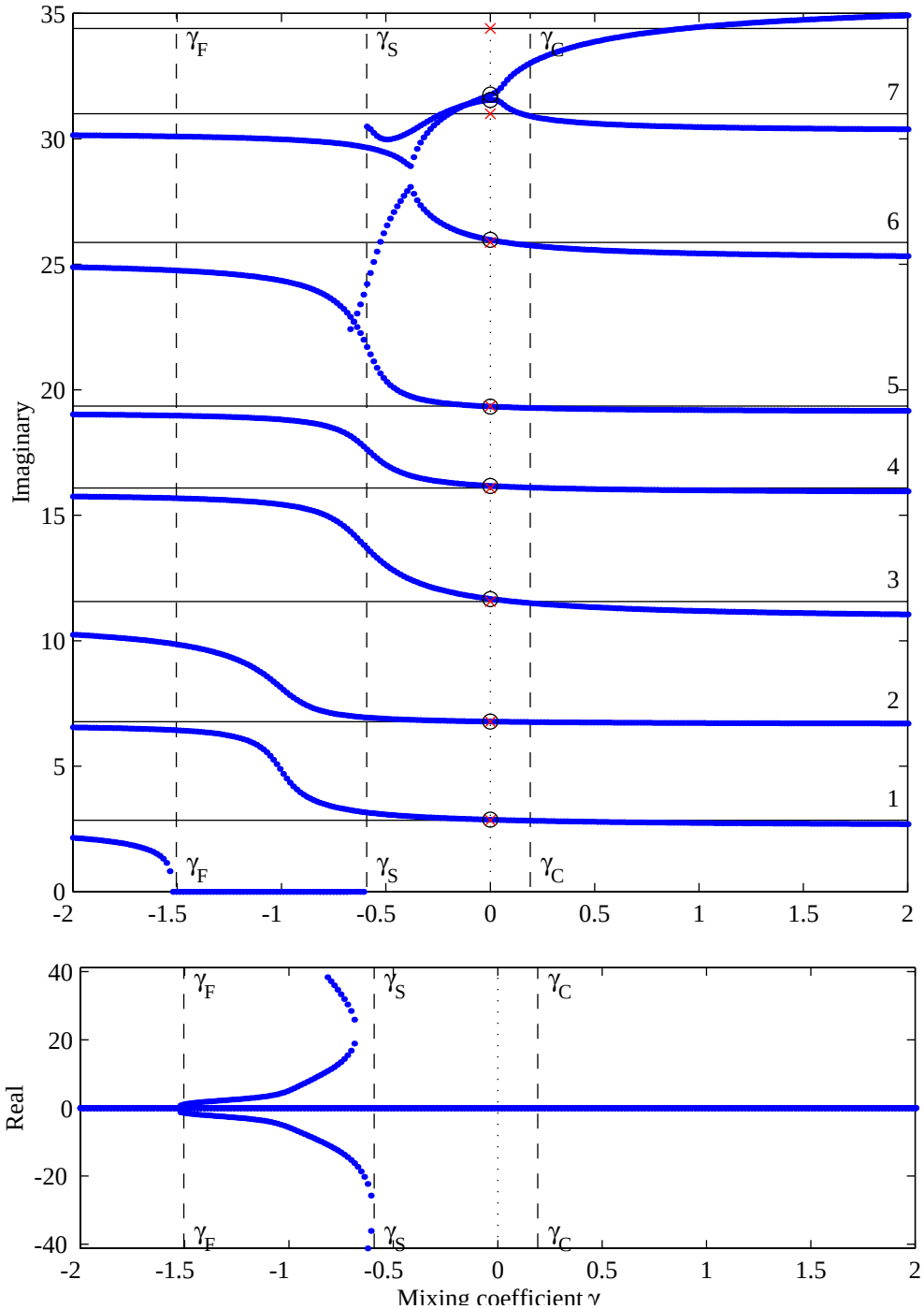

Figure 4.12 Zero trajectories of the model based on the identified strain and force sensor transfer functions.

The solution can be found as a least squares approximation. For the experimental special values $\gamma_C^e = 0.2$, $\gamma_S^e = -0.6$, and $\gamma_F^e = -1.5$ obtained from Figure 4.12 and the known parameters $\alpha = 1.0$, $\chi_C = 102$, the force sensor relative stiffness was estimated to be $\beta \approx 1.33$. The sensor ratio according to this estimate is $\chi_c \approx 87.6$.

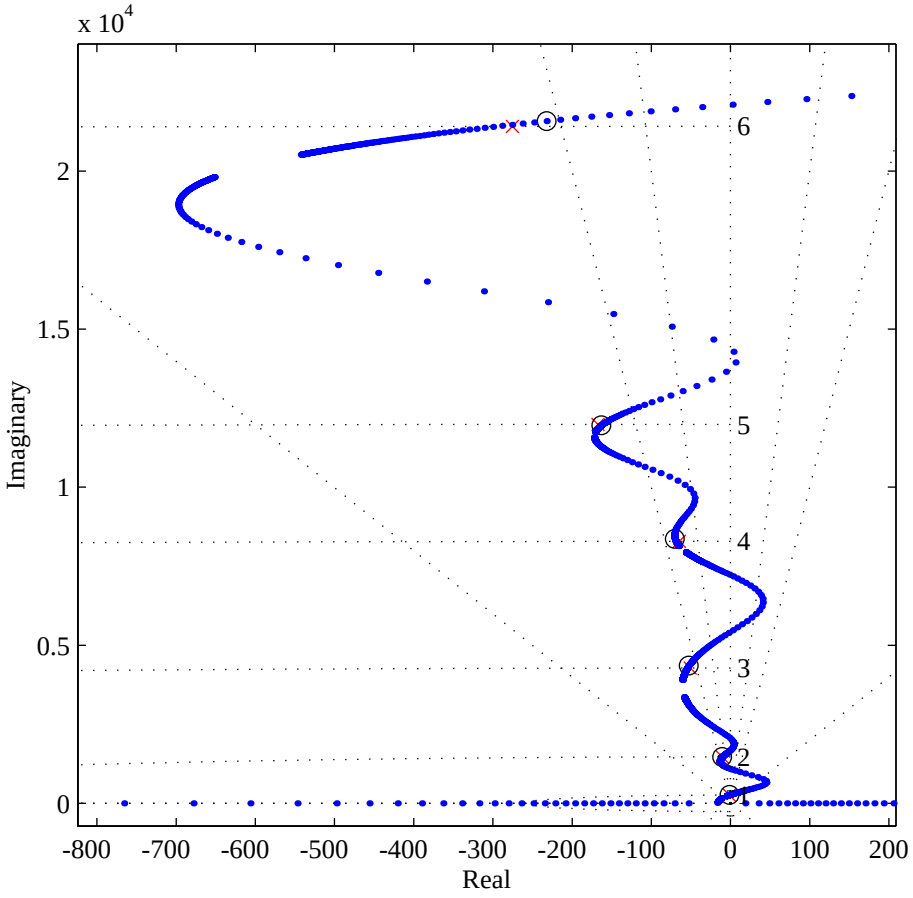

Figure 4.13 Zero locus of the low-frequency modes for the model based on the identified strain and force sensor transfer functions; the modes with low observability/controllability were eliminated.

To estimate the quality of the least squares fit the special values of the mixing coefficient were recalculated using the estimates for β and χ_C. The returned approximated values are $\gamma_C^{LS} = 0.28$, $\gamma_S^{LS} = -0.86$, and $\gamma_F^{LS} = -1.24$. The fit is not particularly good. Specifically, the static model had difficulty fitting a low value of γ_C^e.

For a look from a different perspective, the detail of the zero locus focusing on the first six modes is shown in Figure 4.13. The low-observability modes were eliminated from the model, in order to clarify the picture. The overall shape of the zero locus is not dissimilar to that encountered in the beam models in Chapter 2. The big difference, however, is that the zeroes travel into the right-hand side of the s-plane. Such behavior was not observed in the simple models.

At higher frequencies, the branches of the zero locus are less understandable. The full plot is shown in Figure 4.14. Two branches sweeping through high damping values on the left- and right-hand side of the s-plane are clearly related to the pair of lightly-damped zeroes present in the identified strain sensor transfer function. Another possible factor in the change of behavior for higher modes is the finite order of the identified model itself (11 modes not counting the nearly unobservable ones).

Phase 3: Experimentally Mixed Transfer Functions

Because unexpected complex NMP zeroes were encountered in the mixed transfer functions of the model based on the sensor transfer functions, it was decided to mix the two sensor signals in an analog circuit and record the resulting experimental mixed transfer functions. Twelve mixed transfer functions were measured for a set of mixing coefficient ranging from -2 to +2.

System identification procedure was performed on all transfer functions at once, again using IFORSELS method. The resulting system has one input and twelve outputs, one for each experimental transfer function.The modes with low observability and controllability were removed from the model. Because of the number of transfer functions involved, the fit was not as close as for the original sensor data. Most transfer functions were identified with acceptable quality however, with one notable exception of a transfer function with $\gamma = -0.6$ which was clearly MP in the experiment but became NMP in the identified model.

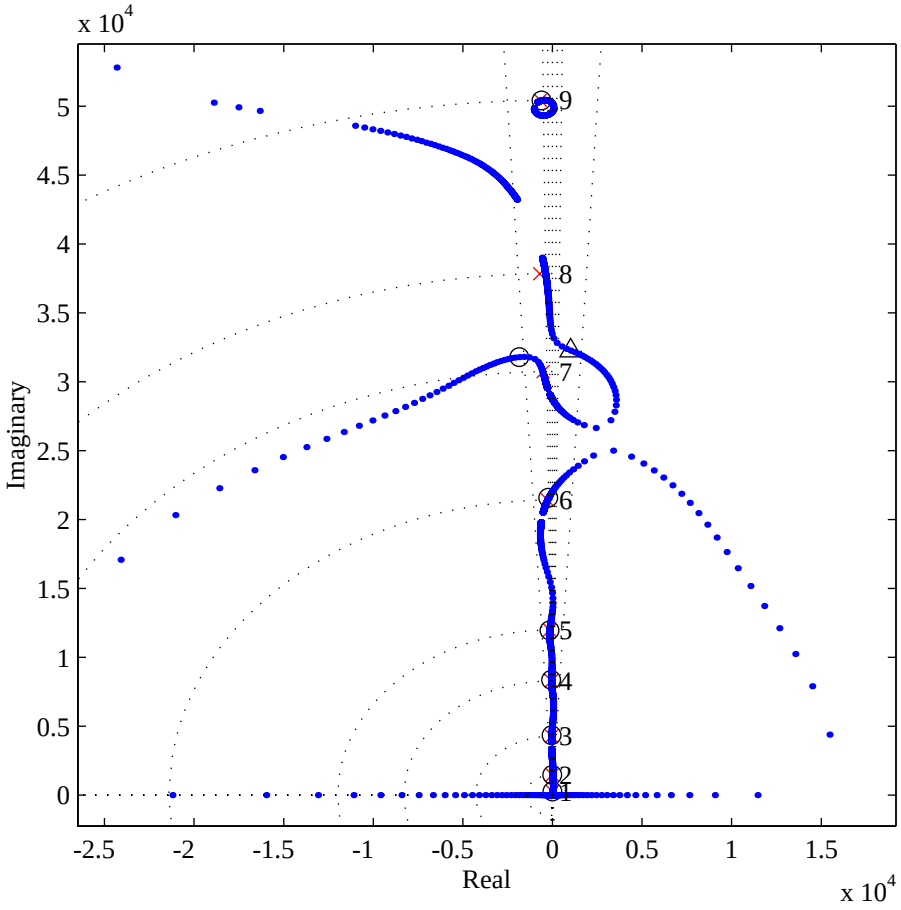

Figure 4.14 Full view of the zero locus based on the identification of the sensor transfer functions; also shown zeroes of the strain sensor transfer function: minimum phase (circles) and non-minimum phase (triangles); the non-minimum phase branch is visible on the right.

Figure 4.15 shows the zero trajectory plot of zeroes from the model based on the two identified sensor transfer function with the zeroes of individual experimentally mixed transfer functions over-plotted as large asterisks. The correlation between zeroes resulting from two models is acceptable.

Similarly, a combination plot showing the zero locus resulting from the two models is shown in Figure 4.16. The match between the two models is not as good when the zero motion is plotted in the s-plane. Three types of discrepancies between the model based on two sensor transfer functions and the system of identified mixed transfer functions can be

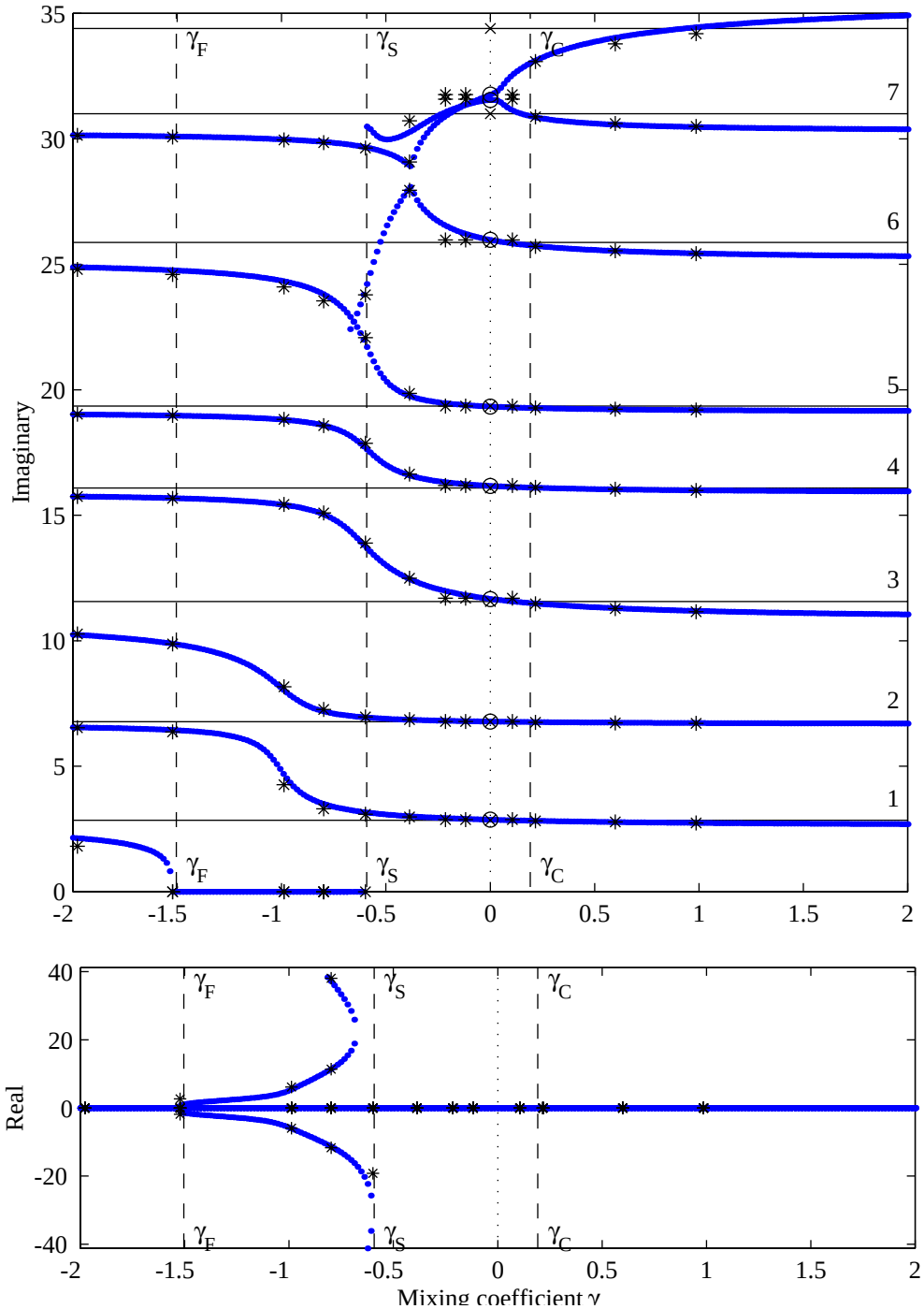

Figure 4.15 Zero trajectory plot based on the identification of two sensor transfer functions (small dots) and identification of individual experimentally mixed transfer functions (asterisks).

noticed: (i) complex NMP zeroes predicted by the first one but did not occur in the second one (see zeroes between modes 1 and 2); (ii) complex NMP zeroes observed in both (see zeroes between modes 3 and 4); (iii) complex NMP zero was not predicted by the first one, it did not occur in experiment, but appeared in the second identified system (a single zero between modes 4 and 5).

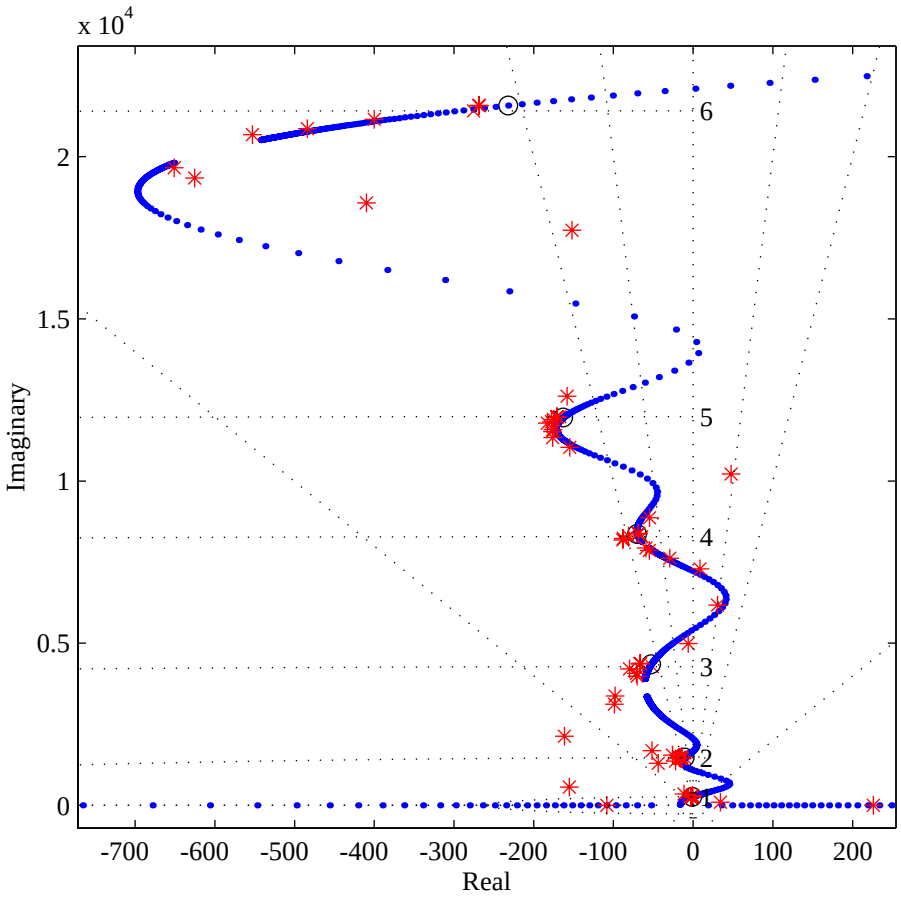

Figure 4.16 Zero locus based on the identification of two sensor transfer functions (small dots) and identification of individual experimentally mixed transfer functions (asterisks), radial lines of constant damping are plotted for values of 0.5%, 1%, and 5%.

By comparing Figure 4.15 and Figure 4.16, it can be concluded that the method of identifying the two sensor transfer functions and mixing them in software was able to capture

the frequency of the zeroes of the mixed transfer function (seen in Figure 4.15) much more successfully then their damping (in Figure 4.16).

4.3 Discussion of Results

The ability to adjust the pole-zero spacing in the structural transfer function was experimentally demonstrated for the case of distributed actuation on a beam.

In the low frequencies the appearance of the experimental zero trajectory plot was similar to the shape expected based on the static ASM model. The stiffness of the force sensor and the ratio of the sensor coefficients was estimated from the experimental zero trajectory plot by fitting the experimental special values of the mixing coefficient to the static model of a four-element actuator-sensor module. Although the values obtained are reasonable, the fit of the model to data was not particularly good. Specifically, a low value for the mixing coefficient corresponding to pole-zero cancellation (γ_C) made the fit difficult.

Real-valued NMP zeroes appeared in the identified models in the negative range of mixing coefficients. The appearance of real-valued zero branches was similar to those observed in simple models. The presence of real-valued NMP zeroes in the model based on experimental data may be interpreted as confirmation of their existence. However, the identified model is still a finite-dimensional representation of a continuous system and these results do not answer the question whether the real zeroes, both MP and NMP, are artifacts of modal truncation or not.

Complex NMP zeroes which were not predicted by beam models were also observed. One branch of NMP zeroes was apparently related to the NMP zero present in the strain sensor transfer function. In addition, the branch which otherwise looked like the one predicted by models crossed into the right hand-side of the s-plane. For three values of the mixing coefficient seen between modes #3 and #4 a 180° phase loss was observed in the experimental transfer function and the identified model placed a NMP zero at that frequency. Taking additional data points by recording additional experimentally-mixed transfer functions

confirmed the original results. The inability to predict complex NMP zeroes is considered to be the biggest deficiency of the models in Chapter 2.

Chapter 5

CONCLUSIONS

Summary

This work focused on a method of shaping the open loop structural transfer function from a distributed sensor to a distributed actuator. The outputs of two sensors of different impedances were combined electronically with the goal of increasing pole-zero spacing for improved performance in low-authority structural control loops. The concept of a three-element actuator-sensor module (ASM) capable of adjusting the equivalent actuator and sensor impedances was presented. The module consists of an actuator, and two sensors for measuring force and strain. The output of the module is constructed by mixing the force and strain signals using a mixing coefficient which can be used to tune the apparent sensor impedance for maximum performance. General shape of zero trajectories as a function of the mixing coefficient was derived. Mass-spring and beam models were used in examples. Both approximate and exact models of beams were employed.

A practical implementation of the module was proposed. The design uses a piezoelectric actuator with a collocated piezoelectric strain sensor and a novel piezoelectric shear load cell. A test article was built, mounted on a cantilever aluminum beam, and tested. Experiments verified the ability to increase pole-zero separation of a structural transfer function by mixing the outputs of displacement and force sensors. Experimentally obtained zero trajectories were compared to the results of simple models.

The overall shape of experimental zero trajectories followed the pattern predicted by considering a static model of the ASM and models of simple mass-spring and beam structures. Specifically, two branches of real-valued minimum phase (MP) and non-minimum phase (NMP) zeroes were encountered for a certain range of negative mixing coefficients. In addition, the experimental results indicated presence of complex NMP zeroes for negative values of the mixing coefficient which were not found in the models of simple structures.

Conclusions

1. Characteristic features of zero trajectories resulting from output mixing were identified by considering a static model of the ASM and models of simple structures. The predicted overall shape and the main features of zero trajectories were confirmed by the experimental mixed transfer functions. However, an attempt to estimate the equivalent static stiffness parameters of the practical ASM design by fitting the measured special values of the mixing coefficient to the ASM static model was not particularly successful. This result suggests that the practical design is significantly different from the static model even at low frequencies.

2. A piezoelectric shear load cell suitable for measuring the force acting through a distributed actuator on a beam structure was built and incorporated into an actuator-sensor module. The method used for applying electrodes to the sides of a thin piezoelectric wafer proved to be simple and produced repeatable results. It appears possible to apply electrodes using the same method to piezoelectric wafers thinner than 0.010 in. The pole-zero structure of transfer functions to the shear sensors was found different from that of the dummy sensors placed at the same location on the beam but not in the load path from the actuator to the structure.

3. The feasibility of controlling pole-zero spacing in a piezoelectric-to-piezoelectric transfer function by means of adjusting the effective sensor imped-

ance of the actuation-sensor module using output mixing was experimentally demonstrated.

4. Based on the work done in the past, NMP behavior of the mixed output was expected for certain negative values of the mixing coefficient [Fleming, 1990; Spangler, 1994]. Physical interpretation of the NMP behavior was given in Chapter 2. Nearly symmetric real-valued MP and NMP zeroes were observed in the mass-spring model and the finite dimensional model of the beam. The infinite-dimensional model of the beam had only imaginary zeroes because the procedure for finding the zeroes of the exact transfer function used in this work could not return real zeroes. Despite the apparent difference in the pole-zero structure between the exact and the approximate solutions, the transfer functions obtained using the two methods were nearly identical in both magnitude and phase. The finite-dimensional representation of the experimental transfer functions also included real-valued zeroes which formed a familiar pattern of nearly-symmetric MP and NMP pairs.

   The conclusion which can be made based on the available information is that the real-valued NMP zeroes represent true NMP behavior caused by measuring the difference between two dynamic signals and are not artifacts of model discretization or truncation. It is believed that an appropriate solution procedure would identify real-valued zeroes in the wave solution as well.

5. In a clear departure from the results of the models of simple structures in Chapter 2, the finite-dimensional representation of the experimentally mixed transfer functions included complex lightly-damped NMP zeroes. One of the NMP zero branches is believed to be caused by the presence of a NMP zero in the strain sensor output. However, an additional mechanism which drives the zero trajectories into the right-hand side of the s-plane appears to be at work and it is not captured in the models of Chapter 2. Complex NMP zeroes remain unexplained and warrant further investigation.

Recommendations for Future Work

1. Further research is needed to understand what parameter not included in the present models causes the zeroes of the experimental mixed transfer function to come close to and even cross the imaginary axis leading to the appearance of complex lightly-damped NMP zeroes.

2. The effects of the presence of real-valued NMP zeroes in the open loop transfer function on the effectiveness of a local controller must be investigated.

3. Performance increases expected due to improved pole-zero spacing should be verified by closing a feedback loop around the mixed transfer function. Any one of the commonly used classical or optimal methods can be used [Yung, 1996].

4. It is expected that some actuator efficiency is sacrificed by lifting the actuator off the beam surface and mounting it two risers of finite stiffness. If the present actuator-sensor module design were to be used in a practical application the effect of design parameters on the efficiency of the load transfer from the actuator to the structure must be investigated.

Potential Improvements to the Specific ASM Design

1. From the actuation efficiency point of view it is better to use a softer strain sensor. The strain sensor can be made thinner than the actuator. It can also be made from a softer piezoelectric material such as polyvinylidene fluoride (PVDF).

2. It is also desirable to use a stiffer force sensor. One possible approach is to use a thinner shear sensor. The area available for electrode application will be reduced and the expected voltage output will be lower, but these changes do not appear to prevent the use of a thinner shear sensor, e.g. 0.005 in thick.

3. The design parameter whose effects on the force sensor output was not properly explored is the dimension of the shear sensor in the direction along the length of the beam. A more detailed finite element model could be constructed to understand the reason for the dependence of the transfer functions on the grounding scheme of the shear sensors mentioned in Chapter 4.

4. To minimize the possibility of damage to the active elements, the gap between the structure and the actuator-sensor package spanning the two risers can be filled with some material to provide support for the fragile piezoelectric wafers.

REFERENCES

[Anderson, 1993] Anderson, Eric H., *Piezoceramic Actuation of One- and Two-Dimensional Structures*, Technical Report #5-93, MIT SERC, 1993.

[Andersson, 1993] Andersson, M. S. and E. F. Crawley, *Spatially Filtering Strain Sensors for Structural Shape Estimation of Intelligent Structures*, Technical Report 3-93, MIT SERC, Feb. 1993.

[Auburn, 1980] Auburn, J. N., "Theory of the Control of Structures by Low-Authority Controllers," *J. of Guidance and Control*, Vol. 3, No. 5, 1980, pp. 444-451..

[Burke, 1987] Burke, S.E., and Hubbard, J.E., "Active Vibration Control of a Simply Supported Beam Using a Spatially Distributed Actuator," *IEEE Control System Magazine*, Aug. 1987, pp.25-30.

[Burke, 1991] Burke, S. E., Hubbard, J. E. J., Meyer, J. E., "Colocation: Design Constraints for Distributed and Discrete Transducers," *Proceedings, 13th Biennial Conference on Mechanical Vibration and Noise*, Miami, Florida, September 22-25, 1991, pp. 75-81. DE Vol. 34.

[Canon, 1984] Canon, R. H., Rosenthal, D. F., "Experiments in control of flexible structures with non-collocated sensors and actuators," *J. of Guidance Control and Dynamics*, vol. 7, no. 5, Sept.-Oct., 1984, pp. 546-553.

[Caughey, 1987] Caughey T.K., and Fanson, J. L., *An Experimental Investigation of Vibration Suppression in Large Space Structures Using Positive Position Feedback*, Dynamics Laboratory Report DYNL-87-1, CalTech, 1987.

[Chen, 1989] Chen, G. S., Lurie, B. J., and Wada, B. K., "Experimental Studies of Adaptive Structure for Precision Performance," *Proceedings of the 30th AIAA/ASME/ASCE/AHS Structures, Structural Dynamics, and Materials Conference*, AIAA, Washington, DC, 1989, pp. 1462-1472. AIAA paper 89-1327.

[Chen, 1990] G.-S. Chen and B.J. Lurie, 1989, *Bridge Feedback for Active Damping Augmentation*. AIAA paper 90-1243.

[Crawley, 1987] Crawley, E. F. and deLuis, J., "Use of Piezoelectric Actuators as Elements of Intelligent Structures," *AIAA Journal*, No. 10, Oct. 1987, pp. 1373-1385. AIAA paper 86-0878.

[Crawley, 1990] Crawley, E. F. and Anderson, E. H., "Detailed Models of Piezoceramic Actuation of Beams," *J. of Intelligent Material Systems and Structures*, Vol. 1,

No. 1, Jan. 1990, pp. 4-25.

[de Labontaine, 1986] de Lafontaine, J., Steiber, M., "Sensor/Actuator selection and placement for control of elastic continua," in Rauch, H. (ed.), *Control of Distributed Parameter Systems 1986: Proceedings of the 4th IFAC Symposium*, Los Angeles, CA, pp. 225-232.

[Dosch, 1992] Dosch, J. J., Inman, D. J., and Garcia, E., "A Self-Sensing Piezoelectric Actuator for Collocated Control," *J. of Intelligent Material Systems and Structures*, Vol. 3, Jan. 1992, pp. 166-185.

[Fanson, 1988] Fanson, J. L., and Garba, J. A., *Experimental Studies of Active Members in Control of Large Space Structures*. AIAA paper 88-2207.

[Fanson, 1989] Fanson, J. L., G.H. Blackwood, and C.-C. Chu, "Active Member Control of Precision Structures," *Proceedings of the 30th Structures, Structural Dynamics, and Materials Conference*, Mobile, AL, 1989, pp.1480-1494. AIAA paper 89-1329.

[Fanson, 1990] Fanson, J. L., and Caughey, T.K., "Positive Position Feedback Control for Large Space Structures," *AIAA Journal*, Vol.28, No.4, 1990, pp.717-724. AIAA paper 87-0902.

[Fleming, 1990] Fleming F. M., "The Effect of Structure, Actuator and Sensor on the Zeros of Controlled Structures", SERC Report #18-90, S.M. Thesis, Massachusetts Institute of Technology, Dec. 1990.

[Fleming, 1991] Fleming, F. M. and Crawley, E. F., "The Zeroes of Controlled Structures: Sensor/Actuator Attributes and Structural Modeling," *Proceedings, 32nd AIAA Structures, Structural Dynamics and Materials Conference*, Baltimore, MD, 1991. AIAA paper 91-0984.

[Goodson, 1970] Goodson, R. E., "Distributed system simulation using infinite product expansions," *Simulation*, Dec. 1970, pp. 255-263.

[Graff, 1975] Graff, Karl F., *Wave Motion in Elastic Solids*, Dover Publications.

[Guicking, 1989] Guicking, D., Melcher, J. and Wimmel, R., "Active Impedance Control in Mechanical Structures," *Acustica*, Vol. 69, 1989, pp. 39-52.

[Hagood, 1988] Hagood, N. W. and Crawley, E. F., "Development and Experimental Verification of Damping Enhancement Methodologies for Space Structures," MIT Space System Laboratory, Report No. 18-88, September, 1988.

[Hagood, 1991] Hagood, N. W. and Anderson, E. H., "Simultaneous Sensing and Actua-

tion Using Piezoelectric Materials," *Proceedings, SPIE Conference on Active and Adaptive Optical Components*, San Diego, July 1991. SPIE paper 1543-40.

[Hall, 1991] Hall, S. R., Crawley, E. F., How, J., and Ward, B., "A Hierarchic Control Architecture for Intelligent Structures," *AIAA J. of Guidance, Control, and Dynamics*, Vol. 14, No. 3, May-June 1991.

[IEEE, 1978] IEEE Std 176-1978, 1978, *IEEE Standard on Piezoelectricity*, The Institute of Electrical and Electronics Engineers.

[Jacques, 1996] Jacques, R. N., K. Liu, and D. W. Miller, "Identification of Highly Accurate Low Order State Space Models in the Frequency Domain," *Proceedings, International Federation of Automatic Control World Congress*, San Francisco, CA, July 1996.

[Lu, 1991] Lu, Utku, K. "Vibration suppression for large scale adaptive truss structures using direct output feedback control," *J. of intelligent material systems and structures*, vol. 4, no.3, 1991, pp.385-397.

[Lurie, 1992] B. J. Lurie, S. W. Sirlin, J. F. O'Brien, J. L. Fanson, "The dial-a-strut controller for structural damping," *Proceedings of ADPA/AIAA/ASME/SPIE Conference on Adaptive Structures*, 1992.

[McCain, 1995] McCain, Amy Jean, *Shaped Actuators and Sensors for Local Control of Intelligent Structures*, Technical Report #3-95, MIT SERC, 1995.

[Meirovitch, 1975] Meirovitch, Leonard, *Elements of Vibration Analysis*, McGraw-Hill, second edition, 1986.

[Preumont, 1990] Preumont, A., Sparavier, M., and Dufour, J. P., "Application of Piezoelectric Actuators to the Active Damping of a Truss Structure," *Proceedings of the 31st AIAA/ASME/ASCE/AHS Structures, Structural Dynamics, and Materials Conference*, AIAA, Washington, DC, 1989, pp.91-103. AIAA paper 90-0950.

[Preumont, 1992] Preumont, Dufour, Malekian, "Active Damping by a Local Force Feedback with Piezoelectric Actuators," *J. of Guidance, Control, and Dynamics*, v.15, no.2, March – April 1992.

[Schaechter, 1981] Schaechter, D., "Optimal Local Control of Flexible Structures," *J. of Guidance and Control*, Vol. 4, No. 1, 1981, pp. 22-26.

[Spangler, 1994] Spangler, Ronald, L., *Broadband Control of Structural Vibration Using Simultaneous Sensing and Actuation with Nonlinear Piezoelectric Elements*, MIT, PhD thesis, 1994, SERC Report 7-94.

[Spector, 1988] Spector, Flashner, *Modeling of noncolocated structural control systems*, 1988.

[Stieber, 1988] Stieber, Michael, E., “Sensors, Actuators, and Hyperstability of Structures,” *AIAA Guidance, Navigation and Control Conference*, 1988. AIAA paper 88-4057.

[Williams, 1989] Williams, Trevor, “Transmission-Zero Bounds for Large Space Structures, with Applications,” *Journal of Guidance, Control, and Dynamics*, Vol. 12, No. 1, Jan.-Feb., 1989, pp. 33-38

[Williams, 1990] Williams, T., and Jer-Nan Juang, "Pole/Zero Cancellations in Flexible Space Structures,” *J. of Guidance, Control, and Dynamics*, Vol. 13, No. 4, July-Aug., 1990, pp. 684-690.

[Yung, 1996] Yung, Jeremy H.,*Compensation Methodologies for Local Control using Strain Actuators and Sensors*, MIT, SM thesis, 1996, AMSL Report 96-2.